2015

Microfluidic Nanoparticles Focusing and Separation

Chao Zhao
Lehigh University

Microfluidic Nanoparticles Focusing and Separation

by

Chao Zhao

Presented to the Graduate and Research Committee

of Lehigh University

in Candidacy for the Degree of

Doctor of Philosophy

in

Materials Science and Engineering

Lehigh University

August 2015

Approved and recommended for acceptance as a dissertation in partial fulfillment of the requirements for the degree of Doctor of Philosophy.

Student: Chao Zhao

Dissertation Title: Microfluidic Nanoparticles Focusing and Separation

_____

Date

_____

Xuanhong Cheng, Dissertation Director, Chair

_____

Accepted Date

Committee Members:

_____

James Gilchrist

_____

Alparslan Oztekin

_____

Jeffrey M. Rickman

Acknowledgements

My deepest appreciation first goes to Professor Xuanhong Cheng, my Ph.D. advisor. It was she who leads me into the field of microfluidics and bioMEMS, and none of my accomplishments could ever be possible without her enormous supports, inspiration and guidance during my five years at Lehigh. She has shown me a high standard as a scientist and a teacher that I can follow in my future career. It was a great honor to work with her.

I also want to thank Professor James Gilchrist, Professor Alparslan Oztekin, and Professor Jeffrey M. Rickman from Lehigh University for serving on my Ph.D. committee, I have learned a lot from the discussions with them.

I would also like to express my thanks to all my friends at Lehigh, Dr. Weihao Weng, Dr. Qian He, Dr. Wanjun Cao, Dr. Qian Wu, Dr. Jinxin Fu, Dr. Ming-Tzo Wei, Yan Wang who have made my life full of joy and thankfulness. I especially thank my group members, Dr. Yi Hu, Dr. Bu Wang, Dr. Krissada Surawathanawises, Dr. Hang Li, Caroline Multari, Keely Heinz, and Liping Pan.

Finally, I want to express my deepest thanks to my parents, my wife, Dan You, and our upcoming baby for their love, support and encouragement. This dissertation is dedicated to them.

Table of Contents

List of tables

List of figures

Abstract

Focusing and separation of bionanoparticles, such as HIV virus, is a critical step in clinical diagnosis. However, it often requires sophisticated infrastructure that is not easily accessible in resource limited environment. Microfluidics is a promising solution to biological sample processing and diagnostics at the point of need because the ability to use very small quantities of samples and reagents, and to carry out separations and detections with high resolution and sensitivity; low cost; short time for analysis; and small footprints for the analytical devices. By studying migration of nanoparticles by gravity or temperature gradient, we designed devices that can focus and separate nanoparticles.

Clinical analysis of acute viral infection in blood requires the separation of viral particles from blood cells, since cytoplasmic enzyme inhibits the subsequent viral detection. To facilitate this procedure in settings without access to a centrifuge, we present a microfluidic device to continuously purify bionanoparticles from cells based on their different intrinsic movements on the microscale. Also, lateral flow introduced by gravity which serves as key for particle separation was quantified.

Enriching nanoparticles, both biological and synthetic in a solution, is commonly practiced for various applications. A general method to focus nanoparticles in a microfluidic channel in a label free and continuous flow fashion is not yet available, due to a dominant Brownian force on the nanoscale. Recent research of thermophoresis indicates that thermophoretic force can overcome Brownian force to direct nanoparticle movement. Coupling thermophoresis with natural convection on the microscale has been shown to induce significant enrichment in a closed capillary. However, the sample volume and throughput are not practical, due to difficulty to control thermophoretic and the naturally convective transport independently, and the concentrated samples are hard

to retrieve. We designed a microfluidic device to couple artificial recirculation with thermophoresis which allows effective nanoparticle focusing and continuous sample retrieval from the outlet. Numerical analysis studies how the microfluidic geometry and flow condition controls the focusing effect. The results demonstrate that the ratio between the thermophoretic and convective fluxes governs the concentration factor, which reaches maximum when the ratio is approximate one. Microfluidic device was also designed and assembled to reveal the physical processes behind the concentration phenomena and show nanoparticles focusing by one order of magnitude.

1 Introduction

Separation and enrichment of biological nanoparticles, such as viruses and disease specific exosomes, is a critical step in clinical diagnosis. However, purifying and concentrating bionanoparticles often require sophisticated infrastructure that is not easily accessible in resource limited environment. For example, centrifugation is the most commonly used method in biological lab, while bulky instruments are necessary. With great advances in the sensing technology, portable, simple and inexpensive sample processing method is becoming a significant bottleneck towards point-of-need detection of microorganisms. Microfluidics is a promising solution to biological sample processing and diagnostics at the point of need because the ability to use very small quantities of samples and reagents, and to carry out separations and detections with high resolution and sensitivity; low cost; short time for analysis; and small footprints for the analytical devices [1]. Recently, researchers have achieved tremendous success in deterministic flow of micron sized colloid particles in microfluidics. One popular and effective method is by coupling lift and inertial forces [2–8], and this technique is widely explored on cells [9–14]. However, if the size of the particle decreases to submicron, the strategy for microparticles focusing and separation is no longer easily applicable [3], because the inertial forces for microparticle sorting is reduced to be less than the Brownian force [2]. Brownian force, which is the random moving of particles suspended in a liquid resulting from their bombardment by atoms and molecules, is always an obstacle for focusing submicron particles. Alternatively, external field is applied to the solution containing the particles and particles of different physical properties are separated based on the force experienced.

1.1 Particle separation by different types of engineered forces

In order to control and manipulate colloidal particles in a suspension, lots of significant work have been accomplished, in which phoresis effects attract the most attention [15]. Phoresis is the migration of colloidal particles under an external gradient, like dielectrophoresis under electric field gradient, magnetophoresis under magnetic field gradient, diffusiophoresis under solute concentration gradient and thermophoresis under temperature gradient. On the other hand, fixed forces, such as gravity, electric field and hydrodynamic forces also show promising results in particle separation [16].

Indeed, the most commonly used method to manipulate colloidal particles is dielectrophoresis (DEP). DEP is a phenomenon in which a force is exerted on a dielectric particle while it is subjected to a non-uniform electric field. The simplest theoretical model is that of a homogeneous sphere surrounded by a conducting dielectric medium. For a homogeneous sphere of radius *r* and complex permittivity ε_p^* in a medium with complex permittivity ε_m^*, the time averaged DEP force is:

$$\langle F_{DEP} \rangle = 2\pi r^3 \varepsilon_m Re\left\{\frac{\varepsilon_p^* - \varepsilon_m^*}{\varepsilon_p^* + 2\varepsilon_m^*}\right\} \nabla \left|\vec{E}_{rms}\right|^2$$

Here $\vec{E}_{rms}$ is the root mean square of the electric field [17]. Yet, to handle nanoparticles in a microchannel experimentally, electrochemical corrosion of an electrode causes deterioration of the electrode and reduced functionality. Further, if the electrode is immersed in an aqueous solution and a voltage is applied, then water decomposes to oxygen and hydrogen bubbles on the surface of an electrode. Usually a coating protection layer is needed on the electrode. Also, DEP is only efficient for insulating suspensions, and conductive suspensions require applying high-frequency electric fields to avoid electrode polarization, and measurements often suffer from noticeable Joule

heating. Comparing DEP force on 10 μm microparticles and on 100 nm nanoparticles, the force decreases by six orders of magnitude. DEP is a dominating force for microparticles, but not for nanoparticles. Recent application of DEP is mostly on microparticles, like cells [18].

Optical trapping is another technique, which utilizes highly focused laser beam to 'grab' the particles. The narrowest point of the focused beam contains a very strong electric field gradient. It turns out that the particles are attracted along the gradient to the region of the strongest electric field, which is the center of the beam. Photons that are absorbed or scattered by the particle in its path exert momentum to the particle. The total force on a particle due to refraction of light is [19]

$$\vec{F}_{OT} = (n/c) \iint (\vec{S}_{in} - \vec{S}_{out}) dA$$

where *n* is the index of the medium, *c* is the velocity of light, $\vec{S}$ is the momentum flux of the light, and *A* is the surface area on the particle. The force is proportional to the surface area of the particle. Comparing optical trapping force on 10 μm microparticles and on 100 nm nanoparticles, the force shrinks by four orders of magnitude. Also, optical trapping is limited to a very small volume as the laser is highly focused and in order to handle large volume, very sophisticated optical setup is needed [20]. It is also mostly applied on microparticles.

For magnetic nanoparticles, the magnetophoretic force is in the same order as the Brownian force [21]. As biological particles lack strong magnetic properties, application of magnetophoresis on cells and viruses requires the binding of the particles with a commercial paramagnetic beads first. The force on the particles is decided by the attached paramagnetic beads.

$$\vec{F}_{MP} = (M \cdot \nabla)\vec{B}$$

with *M* the saturation magnetization of magnetic beads, and *B* the magnetic induction. Currently the binding is depending on collision of the nanoparticles and the magnetic beads, and the binding efficiency is compromised at low target concentrations [22]. Also the introduced magnetic beads bring contaminant to the sample.

Diffusiophoresis explores the migration of particles under solute concentration gradient [23]. When there is a solute concentrating gradient, different diffusion coefficients of anions and cations result in a local electric field, exerting a force on the nanoparticles, originating from the interaction between the localized electric field and double layer on the surface of the nanoparticles. The diffusiophoretic velocity is proportional to the solute concentration gradient

$$v_{DP} = D_{DP} \cdot \nabla log C_s$$

with D_{DP} being the diffusiophoretic mobility, and C_s is the solute concentration. D_{DP} is not size dependent and is only related to the Debye length. This technique is successfully applied on synthetic microparticles and nanoparticles, but bio-vesicles are sensitive to osmotic pressure, and generating solute concentration gradients damages their integrity.

Thermophoresis is also called thermodiffusion, thermomigration, and in fluids the Soret effect, or the Ludwig-Soret effect. An example that can be observed by the naked eyes is the smoke around a hot rod. The smoke goes away from the rod, as diffusion is related to temperature, resulting in a net flux away from the rod. It is quantified as the thermal diffusion coefficient D_T in

$$v_{TP} = -D_{\mathrm{T}} \nabla T$$

and $S_T = \frac{D_T}{D}$ is the Soret coefficient, where v is the thermophoretic velocity, D is the diffusion coefficient of the particle and ∇T is the temperature gradient. In 1930s, thermophoresis was widely studied as a way to separate and concentrate isotope [24,25]. However, in fluid phase, thermophoresis is a much more complicated case, as the interaction near the particle surface is not very well understood. Nevertheless, for thermophoresis, it is immune from electrochemical corrosion, water decomposition and Joule heating. It could be applied to a volume large enough to process medical samples, without introducing contaminant and keeping the osmosis pressure uniform everywhere. Moreover, while all the other phoresis rely on simple particle properties like dielectric constant or surface charge, thermophoresis is taking advantage of interaction at the particle/solvent interface. For example, there are proteins with same surface charge showing thermophoresis effect with opposite migration direction [26]. Furthermore, and most importantly, recent study shows that the Soret coefficient seems to be size independent [27], which can drive significant and directional migration of nanoparticles for their focusing in a suspension.

Inertial forces of fluid on microparticles are proven to be able to separate and focus microparticles, despite the common wisdom that inertia does not contribute to microfluidic phenomena, as the Reynolds number is very small. However, if the channel dimension is in the same order as the microparticles, the particle Reynolds number is critical:

$$Re_p = Re_c \frac{a^2}{D_h^2} = \frac{U_m a^2}{\nu D_h}$$

here Re_p and Re_c are the channel Reynolds number and the particle Reynolds number, respectively, and a is the particle diameter, D_h is the hydraulic diameter of the channel,

U_m is the maximum channel velocity and ν is the kinematic viscosity of the fluid [2]. Inertial forces dominate particle behavior when the particle Reynolds number is of order 1. By coupling the inertial force with secondary flow, microparticles can be focused and separated. However, in order to apply this mechanism on nanoparticles, the microfluidic channel dimension should be less than one micrometer, which is not easy to fabricate and prone to clogging.

The different engineered forces and their utility for nanoparticle manipulation are summarized in Tab. 1 below. The rapid growth of microfluidics techniques opens up a number of possible applications of gravitational migration and thermophoresis, both on practical and basic reasons. In this thesis, we will study the gravitational migration and thermophoresis of nanoparticles in microfluidics.

Table 1 Comparison of forces employed for particle separation.

Several methods	External field	Pros and cons for Bionanoparticles
Dielectrophoresis	Electric field gradient	+ Well controlled gradient - Electrochemical corrosion, water decomposition, Joule heating
Optical trapping	Highly focused laser beam	+ Precious control on single biological microparticle - Very small volume
Magnetophoresis	Magnetic field gradient	+ Control on magnetic beads - Require labeling and introduce contaminant
Diffusiophoresis	solute concentration gradient	+ Require no external electromagnetic gradient - Osmosis pressure on biological species
Thermophoresis	Temperature gradient	+ Temperature gradient is universal in nature, where biological creatures live in - Not a easily controlled gradient
Inertial and hydrodynamic force	Hydrodynamic force	+ Simple channel, high throughput - Channel dimension too small for nanoparticles
Centrifugal force	Centrifugation force	+ Concentrate nearly everything - Time consuming, equipment requirement

1.2 Gravity induced particles separation and swirling

1.2.1 Gravity induced separation of virus from blood cells

Clinical diagnosis of acute viral infection in blood requires purifying viral particles from blood cells, considering the inhibitory effect of the cytoplasmic content to the subsequent nucleic acid amplification reactions. In clinical laboratories, this task is routinely handled by centrifugation, while diagnosis at the point of care demands simple assays without access to bulky instruments. Although manual [28] or CD format [29–31] centrifuges have been recently reported, it is still non-trivial to integrate them into micro total analysis systems.

Alternatively, microfluidic plasma or viral extractors based on non-centrifugal mechanisms have been actively explored in research laboratories. Passive filtration devices, including microfabricated planar filter [32–36] or embedded membranes [37], purify plasma components from blood cell through size exclusion. However, they have a limited throughput and are prone to clogging or red blood cell (RBC) lysis. Biomimedic devices with bifurcation structures [38,39] or expanding channels [40,41] exploit the plasma skimming effect to separate cells from plasma, but only a small fraction of plasma can be extracted since the cell free plasma layer is usually very thin. Other hydrodynamic devices such as deterministic arrays [42], inertial focusing channels [2,43], and microgroove structures [44,45] have been created to sort cells, but very few of them have been optimized to purify nanoparticles in blood. In addition, external electromagnetic fields have been implemented in microchips to induce bulk electrohydrodynamic flow [46], move RBC in a magnetic gradient [47], or physically immobilize blood cells through dielectrophoresis [48], but the extensive accessories to generate high fields and/or the requirement to pre-treat blood samples limit their applications. Magnetic activated particle sorting [49,50] after tagging the target species with magnetic beads purify and concentrate viral particles

effectively, while it still faces the challenge of extensive manual handling and low throughput for point of care uses.

Here, we present a simple, two-layer microfluidic device to continuously purify viruses from blood cells with a high yield of the target virus. This device takes advantage of the different intrinsic movements of micron- and submicron-sized bioparticles on the microscale. While blood cells sediment in a physiological solution with a predictable terminal velocity, submicron-sized viral particles move around by diffusion. Since the two movements have different dependence on time, when a biological sample is layered on top of a buffer solution, the two species can preferentially separate in the vertical direction. Continuous sample processing is achievable in a microfluidic environment when both the biological sample and the supporting buffer are convected in a laminar flow that does not interfere with the intrinsic particle transport. We first performed numerical analysis to predicate the separation effect for different sized particles and then validated the model using suspensions of synthetic particles and diluted blood containing HIV viruses. The continuous operation mode and the parallelization capability offered by microfluidics make this design compatible with high throughput applications. Another advantage of the device is the high yield of the target nanoparticles, always greater than 50% determined by the nature of diffusion. These properties make this device appealing to purify circulating viral particles existing in a low concentration or in a small sample volume. With the automation potential of lab-on-a-chip type of devices, this viral separation design can function as an upstream sample preparation module to continuously provide cell depleted bionanoparticles at the point of care for downstream analysis.

1.2.2 Gravity induced swirl of nanoparticles

Lab-on-a-Chip type of devices utilizing parallel streams of two or more fluids have been developed for a wide range of applications. In the past few years, multi-stream flow containing nanoparticles has attracted interest for nanoparticle separation, concentration [16,23,51,52], assembly [53,54], enhancement of heat transfer and fluid flow [16] as well as thermal insulation [55]. In these applications, adjacent streams from separate inlets are usually assumed to remain parallel, while mass transport across streams happens exclusively through diffusion. The transport phenomena in such systems have been carefully studied employing both computational and experimental approaches [56–59].

However, parallel streams introduced from the inlets don't always have matched density. The resulting density stratification is expected to drive reorientation of the streams. Interfacial reorientation induced by gravity has been observed in microfluidic flows [60–63]. For example, S. K. Yoon *et al.* found empirically that the interface between two miscible and density stratified fluids reoriented when diffusion was negligible. The tilting angle depends on several dimensionless parameters including the dimensionless distance in the flow direction, y/D_h, and the ratio of gravitational force to viscous force, Re/Fr^2. In particular, Re/Fr^2 was found to dominate the flow characteristics. Later, Y. Yamaguchi *et al.* performed fluid dynamics simulation and demonstrated that the reorientation took place in a creeping shear flow of miscible fluids even considering diffusion. In addition to the two parameters mentioned above, microchannel geometry, wall property, interfacial tension between two fluids and inter-stream mass diffusion were also discovered to influence the interfacial reorientation. Beyond simple interfacial tilting, laminar flow of density stratified fluids together with Dean vortices have been shown to generate different types of curved interface [64]. The Dean force in side-by-side two fluids system engenders a distorted but symmetric interface [65]. This is enhanced if the two fluids have a density mismatch and the distorted interface becomes nonsymmetrical given

appropriate angle between gravity and initial fluid interface. While these studies have provided significant insights into density stratified multi-stream flow, they were carried out using relatively high flow rates and low Re/Fr^2, and the resulting reorientation were generally below 0.5π.

In this study, we explored the interface reorientation associated with creeping flow of two miscible, density stratified fluids at much greater Re/Fr^2 than reported previously. The two fluids are introduced side by side into simple straight microchannels and nanoparticles are dispersed in the stream of the lighter fluid. The density stratification is found to generate a gravity-driven flow transition, which induces a swirling motion of the nanofluid. The dependence of the nanofluid swirl on density stratification, hydrodynamic drag and channel geometry are systematically studied using confocal microscopy imaging and computational fluid dynamics modeling.

1.3 Thermal diffusion of suspended colloid particles

1.3.1 Mechanism for thermal diffusion

There is an increasing interest in colloid particle motion under a temperature gradient in a fluid phase in recent years, because it is expected to provide insight into the thermodynamics of the interface between the particle and solvent. The only parameter to characterize the thermophoresis is the thermal diffusion coefficient, and several theoretical descriptions of the thermal diffusion coefficient have been proposed for the mechanism of thermophoresis: interfacial tension gradient [66], nonuniform electrolyte and electrostatic distribution [67], thermal-acoustic perturbations [68], radiation pressures [69], and nonuniform London-van der Waals interactions [70]. The electrostatic explanation is most successful, and proven by experiments. However, there are several different models based on electrostatic mechanism proposed by Anderson [71], Bringuier *et al.* [72], Duhr *et*

al. [73], and Morozov [67], with different predictions between the thermal diffusion coefficient and particle properties.

The theory by Anderson [71] reformulated thermoosmosis of an electrolyte in a porous medium to describe the thermophoresis of particles in liquids. In this theory, when the particles are large relative to the thickness of the interfacial layer, Anderson predicted the thermodiffusion coefficient to be

$$D_T^{Anderson} = -\frac{2}{\eta T}\left[\frac{2\Lambda_{\mathrm{l}}}{2\Lambda_{\mathrm{l}} + \Lambda_{\mathrm{p}}}\right]\int_0^{\infty} yh(y)dy$$

where *h(y)* is the enthalpy density at a distance y from the particle surface, and Λ_{l} and Λ_{p} are the thermal conductivities of the liquid and particle, respectively, and η is the viscosity of fluid.

In the model proposed by Bringuier *et al.* [72], the Soret coefficient is defined

$$S_T^{Bringuier} = \frac{1}{T} + \frac{1}{k_B T}\frac{\partial W_{min}^{dl}}{\partial T} = \frac{1}{T} + \frac{W_{min}^{dl}}{k_B T^2} \times \left[\frac{T}{\epsilon}\frac{\partial \epsilon}{\partial T} + \frac{2T}{\zeta}\frac{\partial \zeta}{\partial T} - \frac{\kappa R_h\left(1 + \frac{T}{\epsilon}\frac{\partial \epsilon}{\partial T}\right)}{2(1 + \kappa R_h)}\right]$$

The first term is the kinetic contribution due to the Brownian motion of the particle, and $W_{min}^{dl} \equiv 2\pi\epsilon R_h(1 + \kappa R_h)\zeta^2$ is the electrical work required to form the double layer. Here ϵ is the dielectric constant of the fluid, ζ is the zeta potential of the particle, κ is the Debye length, and R_h is the particle's hydrodynamic radius.

In the description by Morozov [67], particle velocities are derived from the basis that temperature gradients induce nonuniform electric stresses in the double layer; that is, thermodiffusion is due to unbalanced electrostatic potentials and electrolyte distributions on opposite sides of the particle. The analytic solution for the Soret coefficient is

$$S_T^{Morozov} = \frac{R_h}{2L_B T}\left[\frac{3\Lambda_1}{2\Lambda_1 + \Lambda_p}\right] \times \left[\zeta_D^2 - \left(24 + 8\frac{T}{\epsilon}\frac{\partial \epsilon}{\partial T}\right)\ln cosh\frac{\zeta_D}{4}\right]$$

here $\zeta_D = e\zeta/k_B T$ is the dimensionless zeta potential, and L_B is the Bjerrum length. The above three theories, however, are either not verified by or don't match with experimental results.

Recently, Duhr et al. [73] attributed thermophoresis to two contributions: the entropy of ionic shielding and the temperature-sensitive entropy of water hydration. The contribution from the entropy of the ionic shielding is calculated by Gibbs-free energy $G_{ionic} = Q_{eff}^2 \lambda_{DH}/[2A\varepsilon\varepsilon_0]$, with the effective charge Q_{eff} and the particle surface *A*. Here, $\lambda_{DH} = \sqrt{\varepsilon(T)\varepsilon_0 kT/2e^2 c_s}$ is the Debye length, and ε is the dielectric constant of the fluid. The contribution from the hydration entropy of water was directly inferred from the particle-area-specific hydration entropy $s_{hyd} = S_{hyd}/A$. Finally, the contribution from the Brownian motion is $G = kT$. These three factors, in which the Brownian term can be neglected, add up to

$$S_T^{Duhr} = \frac{A}{kT}\left(-s_{hyd} + \frac{\beta\sigma_{eff}^2}{4\varepsilon\varepsilon_0 T} \times \lambda_{DH}\right)$$

Experiments were guided by this equation through changing the Debye length from the solute concentration, the temperature, and the colloidal size, and matched well with this theory. In our work, Duhr *et al.*'s theory is selected to predict particle's thermal diffusion coefficient.

1.3.2 Experimental systems for the measurement of thermal diffusion coefficients

Different experimental techniques were developed for measuring the thermal diffusion coefficient, including classic Soret cell with beam deflection technique, thermo gravitational column, two-chamber thermodiffusion cell, thermal diffusion forced Rayleigh

scattering, thermal lens method, microfluidics fluorescence method, and thermal field-flow fractionation [74]. The most intensively investigated methods are beam deflection technique and microfluidic fluorescence method.

The beam deflection (BD) method exploits the deflection of a laser beam due to the concentration, and therefore refractive index gradient induced by the impose temperature field [75]. A laser beam is mildly focused through the plate gap, and the position of the transmitted beam is monitored by a position-sensitive detector with a resolution of a few μm, placed far from the cell. The beam suffers first a very rapid downward deflection due to the temperature dependence of the refractive index of the solution $(\Delta\vartheta)_{th}$, followed by a much slower change due to the progressive build-up of the thermophoresis induced concentration gradient $(\Delta\vartheta)_s$. The Soret coefficient is determined as

$$S_T = -\frac{1}{c}\frac{\frac{\partial n}{\partial T}}{\frac{\partial n}{\partial c}}\frac{(\Delta\vartheta)_s}{(\Delta\vartheta)_{th}}$$

where $\frac{\partial n}{\partial T}$ and $\frac{\partial n}{\partial c}$ are respectively the temperature and concentration dependence of the refractive index. BD is a simple, reliable, and accurate method. However, it has a major drawback, since the plate spacing cannot be made much smaller than about 1 mm, time for reach equilibrium is quite long, even for particles with size in a few nm.

The microfluidic fluorescence method is an all-optical imaging for thermophoresis [76]. After introducing a temperature gradient in the microfluidic channel, the concentration evolution was observed and determined by its fluorescent intensity. After the system reaches its steady state, the Soret coefficient could be calculated by

$$S_T = \frac{-ln\frac{c}{c_0}}{T-T_0}$$

where c and c_0 are fluorescent intensity values.

Intensive investigation has been accomplished by using these two methods, and people have been studying thermal diffusion coefficient on different materials, like colloidal latex particles, surfactant aggregates, salt, proteins and biological macromolecules, and polymers, etc [26]. Putnam *et al.* studied thermophoresis of polystyrene (PS) nanoparticles and proteins of T4 lysozyme in DI water [27]. Duhr *et al.* mainly focused on different sized PS nanoparticles and DNA in 1mM Tris buffer [76]. Jiang *et al.* considered 100 nm PS beads in 10 mM Tris buffer and polymer solution [77]. Vigolo *et al.* investigated different sized nanoparticles in 100 mM NaCl brine and Triton X-100 buffer [78]. Braibanti *et al.* studied different sized PS nanoparticles in 1 mM Tris-HCl buffer [79]. These results all show that temperature, particle properties including size, material, and buffer solution are critical for thermophoresis. However, to the author's best knowledge, no work has been done on biological particles like viruses.

Although, the particle differs in material, size, surface structure, zeta potential, and shape, the thermal diffusion coefficient varies within a limited range $1 < D_T < 10\ m^2 s^{-1} K^{-1}$. For example, in Tab. 2, some selected values of the 'rescaled' thermal diffusion coefficient $\widetilde{D}_T = D_T T$ for aqueous systems are shown, ranging from micellar solutions to polymers and spherical latex particles. Numbers in Tab. 2 for PS spheres with radius at 53 nm and 253 nm differ because of different solution composition and measurement technique involved. Strikingly, while diffusion coefficient varies by more than three orders of magnitude, thermal diffusion coefficient changes by no more than a factor of twenty. Also, for 100 nm nanoparticles, $\widetilde{D}_T \gg \mathrm{D}$, so that thermal diffusion is dominant over Brownian motion. This is exactly the benefit of applying thermophoresis on nanoparticles focusing.

Table 2 Values of $\widetilde{D}_T$ and D for some selected colloidal systems [26].

System	$\widetilde{D}_T$ (10^{-6} cm^2 s^{-1})	D (10^{-6} cm^2 s^{-1})
SDS micell (R = 2.5 nm)	12.8 [80]	1.0
Triton X100 (R = 3.5 nm)	7.45 [79]	0.58
NaPSS (M_w = 74 kDa)	7.15 [81]	0.53
PS spheres (R = 53 nm)	4.7 [79] / 1.8 [73]	0.03
PS spheres (R = 253 nm)	4.3 [79] / 7.2 [73]	0.007
PS spheres (R = 1 µm)	30 [73]	0.002

Although the thermal diffusion coefficient is relatively insensitive to the particle size, dynamic study of the transient state shows that the concentration kinetics is size dependent. In addition, hydrodynamic forces and inertial forces are strongly influenced by the particle size. Thus, by coupling thermophoresis effect with hydrodynamic force may also help to separate different particles.

1.3.3 Boosting the concentration factor by coupling thermophoresis with swirling flow in a thermodiffusion column

Granting the theoretical background of thermophoresis in fluid is still in debate, its application on nanoparticles focusing shows tremendous application and remarkable results. Competition between thermophoresis and diffusiophoresis shows interesting experimental results [77,82,83]. Also, DNA and salt in a thermodiffusion column provide a new mechanism for prebiotic molecules to accumulate from a highly diluted ocean [84–91]. Artificial Janus particles are studied to better understand thermophoresis [92]. Thermophoresis in microfluidics starts to attract more attention [78].

Constant diffusion and thermal diffusion coefficients both lead to an exponential depletion law [93],

$$\frac{c}{c_0} = exp[-S_T(T - T_0)]$$

here c is the concentration of the particles, T is the temperature. Although it introduces a concentrating effect on one side of the temperature gradient, the concentration factor is limited, as the temperature gradient could not be infinitely high in a microchannel. In order to boost the concentration factor in a reasonable temperature gradient, microscale thermophoresis coupled with swirling in a thermodiffusion column was demonstrated to show an extremely high concentration factor with biologically friendly setting (Fig. 1). A thermodiffusion column is a closed column, where two side walls have a different temperature. Because of the thermal expansion of water under different temperature in the column, the water is lighter on the warm side, and heavier on the cold side. This introduces a natural convection (Fig. 1c). At the same time, particles in the column experience a thermophoresis in the temperature gradient. The coupling between thermophoresis and swirling boost the concentration factor several orders of magnitude higher than pure thermophoresis, because particles concentrated by thermophoresis to the wall keep migrating to one corner due to swirling flow. However, these two effects are coupled and it is difficult to study each effect independently.

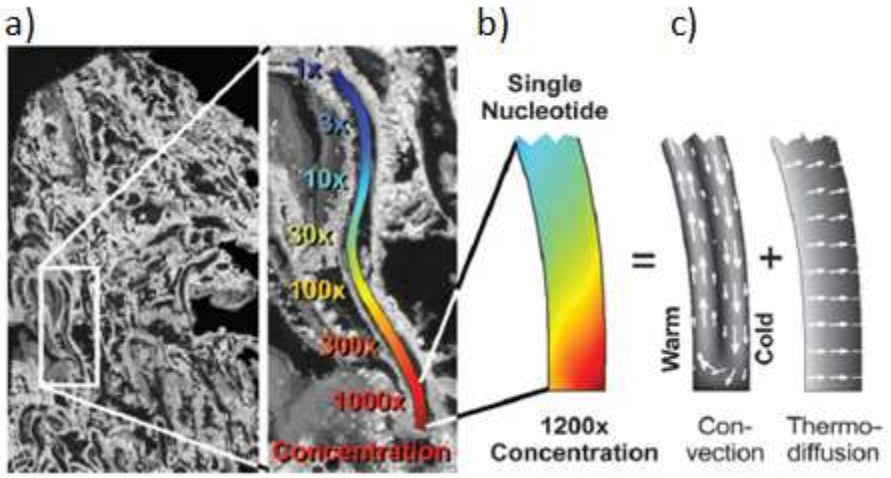

Figure 1 Heat-driven molecular accumulation in hydrothermal pores [86]. a) Section through aragonite from the submarine hydrothermal vent field at Lost City. b) Simulation of a part of the pore system. If subjected to a horizontal thermal gradient of 30 K, a 1200 fold accumulation of single nucleotides is expected. c) The mechanism of accumulation is driven by heat in a twofold way. Thermal convection shuttles the molecules vertically up and down and thermophoresis pushes them horizontally to the right.

Analytical results for thermodiffusion column was first solved by Debye [24] and Onsager *et al.* [25]. Analytical solution was calculated in 2D by solving

$$\frac{\partial n}{\partial t} = D\left(\frac{\partial^2 n}{\partial x^2} + \frac{\partial^2 n}{\partial y^2}\right) + D_T \frac{dT}{dx}\frac{\partial n}{\partial x} - v\frac{\partial n}{\partial y}$$

$$\frac{d^3 v}{dx^3} = -\frac{\alpha g \rho}{\eta}\frac{\tau}{a}$$

here, *n* is the particle concentration, *v* is the fluid velocity, α is the thermal expansion coefficient of the fluid, ρ is the density of the fluid, η is the viscosity of the fluid, τ is the position, and a is the position is the width of the column. Intensive mathematical handling is needed, and under first order approximation, the maximum natural convection velocity is [87]

$$v = \frac{\Delta T \alpha g \rho}{6\eta} a^2 \frac{3}{64}$$

and the steady state accumulation of a thermodiffusion column can be described by

$$\frac{c_{trap}}{c_0} = exp\left(\frac{q/120}{1+q^2/10080} S_T \Delta T r\right)$$

with *q* defined as

$$q = \frac{\Delta T \alpha g \rho a^3}{6\eta D}$$

here $\frac{c_{trap}}{c_0}$ denotes the ratio of the concentration at the accumulation position to the boundaries, and *r* is the aspect ratio of the column.

However, the analytical solution is based on the assumption that the temperature is linear proportional to the position in the column, which may not be the case when the convection disturbs the temperature distribution. Also, a transient solution is also interesting to study the dynamics of concentration evolution. Last but not least, if the column is an open pore as in hydrothermal pores (Fig. 1), the solution could not be applied as it was for a closed system without feeding.

In order to better understand this effect on small molecules, like DNA molecules [86] and polymers [94], continuous models are applied in COMSOL Multiphysics (COMSOL Inc., Burlington, MA) to this problem. Three models are applied:

The model of heat transfer in fluids solves for the temperature gradient,

$$\rho C_p \frac{\partial T}{\partial t} + \rho C_p v \cdot \nabla T = \nabla \cdot (k \nabla T)$$

the creeping flow model describes the swirling velocity profile,

$$\rho \frac{\partial v}{\partial t} + \rho v \cdot \nabla v = -\nabla p + \mu \nabla^2 v + \alpha g \rho (T - T_0)$$

and the species transport model couples fluid flow with thermophoresis to show the species concentration,

$$\frac{\partial c}{\partial t} = \nabla \cdot (D_T c \nabla T + D \nabla c) - \nabla \cdot (vc)$$

Here ρ is the fluid density, μ is the viscosity, C_p is the heat capacity of the fluid, k is the thermal conductivity of the fluid, T is the temperature, t is the time, v is the fluid velocity, p is the pressure, α is the thermal expansion coefficient of the fluid, g is the gravitational acceleration, c is the concentration of the species. The build-in models of COMSOL for species transport need to be modified to include the thermophoresis flux term $D_T c \nabla T$. Initially, the concentration of the species is uniform, and the evolution of the concentration could be predicted under a moderate temperature gradient. In this way, coupling between fluid convection and temperature distribution is enabled, and transient solution is acquired even with the thermodiffusion pore open with molecules feeding from the top. This simulation predicted extreme accumulation of nucleotides in hydrothermal pore system, and enabled a mechanism to provide highly concentrated single nucleotides [86].

The concentration effect in thermodiffusion columns was reported in the literature. Steady state concentrating phenomena of fluorescent dye 8-hydroxypyrene-1,3,6-trisulfonic acid salt (HPTS) (Fig. 2a), deoxycytidine triphosphate (dCTP), 20-mer of adenine Oligo (dA), and oleate in a thermodiffusion column was measured [88]. Also, transient evolution of small molecules like DNA [87] and RNA [94] were shown to match results from the continuous models (Fig. 2b,c).

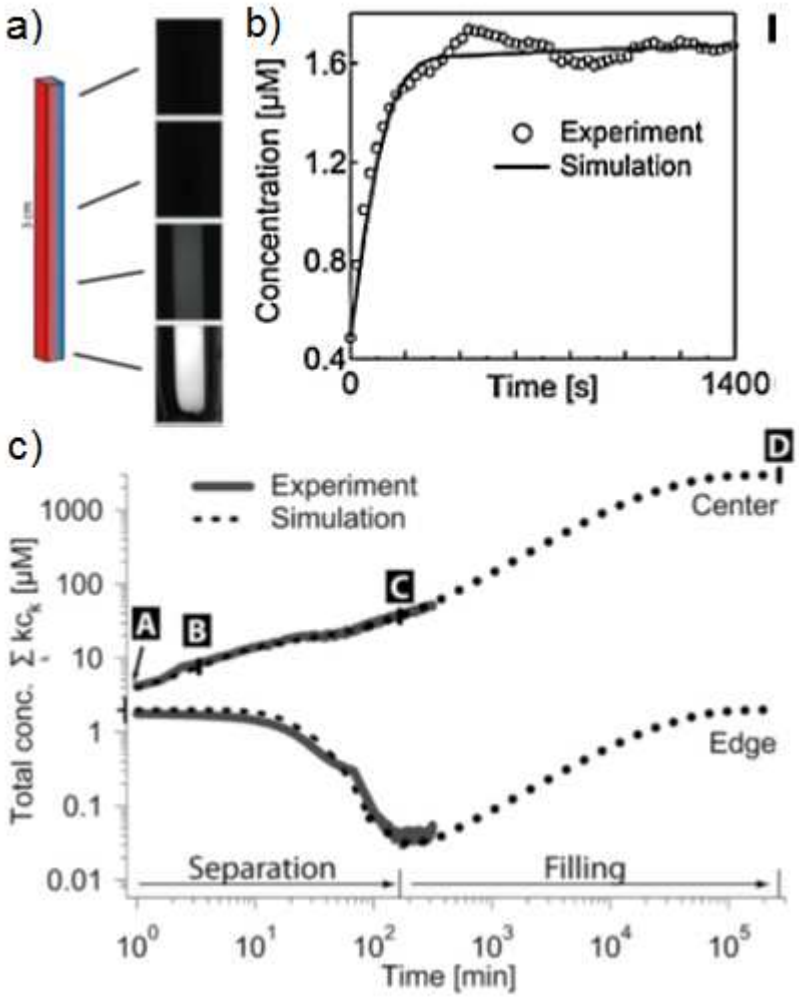

Figure 2 a) Locally concentrated HPTS in a thermodiffusion column [88]. b) The kinetics of accumulation is well described theoretically for DNA [87]. c) Simulated and measured RNA monomer concentration in the center and at the edge of the thermodiffusion column [94].

Fig. 2a shows steady state fluorescence images of a linear capillary about 3 cm long after 24 h at ΔT = 30 K in a thermodiffusion column, revealing a strong concentration gradient of HPTS from top to bottom in the capillary [88]. Here, observing transient evolution of the dye intensity was not possible as the capillary length is far beyond the working distance of the microscope objective, and the temperature controlling unit is not integral in an optical system. Fig. 2b and Fig. 2c compare transient concentration of DNA or RNA in a laser instead of gravity driven thermodiffusion column, and the continuous model match well with experiments. However, in their simulation, in order to apply the

models for thermodiffusion column, transferring from laser induced convection to water expansion induced convection is needed.

The success of experimental measurements of concentration in a thermodiffusion column above is not trivial, as a temperature gradient needs to be applied on a quite small dimension, typically around 100 μm. Different strategies have been proposed to introduce a local temperature gradient in a small dimension [95,96], including focused IR laser [73], heating and cooling block [88], water, silver-epoxy resistive heater [78], etc. Applying temperature gradient in microfluidics has been implemented for polymerase chain reaction (PCR). However, as the channel is small, forming conformal contact between the temperature control unit and the channel is challenging.

Another experimental consideration is in measuring the temperature distribution in situ. This is important as the temperature on the heater and cooler is not necessarily the same as that of the fluid inside the system. People have used a thermochromic solution [97], encapsulated beads of thermochromic liquid crystals [98], nuclear magnetic resonance thermometry [99], Raman spectroscopy [100], and a temperature-dependent fluorescent dye [101], in which the fluorescent dye (Rhodamine B [101] or 2', 7'-bis(carboxyethyl)-5(6)-carboxyfluorescein [73]) is most popular, fully optical, and could be easily integrated into a microfluidic channel.

1.4 Thesis layout

In the above section, we presented the potential of external field in nanoparticles focusing and separation. For biological vesicles, fundamental understanding of nanoparticle migration mechanism is critical. As discussed above, gravity and thermophoresis may present ways to achieve the nanoparticles focusing and separation.

Here, we studied these two forces for focusing and separation applications for viral sample processing.

2 Gravity induced particles separation and swirling

2.1 Gravity induced separation of virus from blood cells

2.1.1 Introduction

Clinical analysis of acute viral infection in blood requires the separation of viral particles from blood cells, since the cytoplasmic enzyme inhibits the subsequent viral detection. To facilitate this procedure in settings without access to a centrifuge, we present a microfluidic device to continuously purify bionanoparticles from cells based on their different intrinsic movements on the microscale. In this device, a biological sample is layered on top of a physiological buffer, and both fluids are transported horizontally at the same flow rate in a straight channel under laminar flow. While the micron sized particles such as cells sediment to the bottom layer with a predictable terminal velocity, the nanoparticles move vertically by diffusion. As their vertical travel distances have a different dependence on time, the micro- and nanoparticles can preferentially reside in the bottom and top layers respectively after certain residence time, yielding purified viruses. We first performed numerical analysis to predicate the particle separation and then tested the theory using suspensions of synthetic particles and biological samples. The experimental results using dilute synthetic particles closely matched the numerical analysis of a two layer flow system containing different sized particles. Similar purification was achieved using diluted blood spiked with human immunodeficiency virus. However, viral purification in whole blood is compromised due to extensive bioparticle collisions. With the parallelization and automation potential offered by

microfluidics, this device has the potential to function as an upstream sample preparation module to continuously provide cell depleted bio-nanoparticles for downstream analysis.

2.1.2 Results and conclusion

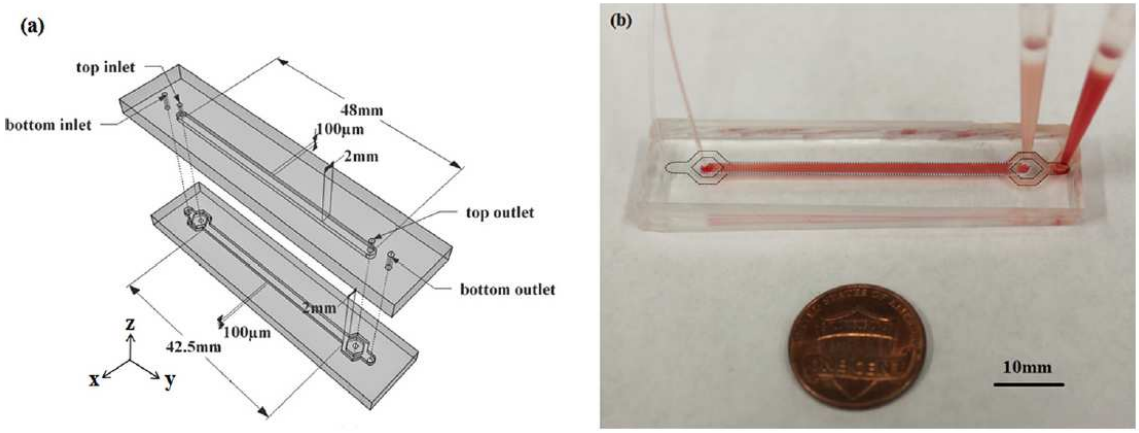

Figure 3 Schematic illustration of the device structure with labeled dimensions (a) and a photograph showing the device in action (b). The device contains two layers of microchannels: the biological sample is injected into the top layer and a carrier buffer is injected into the bottom to allow the separation of the cells versus viral particles by their intrinsic movements. In the photograph, the dark dash line outlines the bottom layer channel and the light dash line outlines the top layer channel.

PDMS microfluidic devices were fabricated (Fig. 3) using the standard soft lithography technique. First, SU-8 photoresist was patterned on a silicon wafer by photolithography to form a negative mold. Next, a 10:1 mixture of poly(dimethylsiloxane) (PDMS) prepolymer and curing agent was poured onto the mold and baked at 70 ºC until cured. After cutting and removing the PDMS channels from the SU-8 mold, a top channel was carefully aligned with a bottom channel and the two were bonded permanently through oxygen plasma at a forward power of 50 W and pressure 100 mT above the base pressure for 30 s. The channels were then blocked with 1% BSA in PBS to reduce nonspecific binding on the channel walls before further experiments.

The overlapping channel of the two layers has a dimension of 2 mm × 42.5 mm × 100 μm (width × length × height) (Fig. 3). The inlet of the bottom channel branches so that the islands in between support the top layer sample flow before it is layered on the bottom cushion buffer. The same branch at the bottom layer outlet allows separate collection of the outflow from two different vertical layers. The flow resistance at the branch region is low compared to that of the main channel, so similar amount of fluid exits from the two layers, as observed in our experiments. COMSOL simulations revealed similar distribution of particle concentration in channels of various dimensions but comparable convection velocity, while the throughput is proportional to the channel width. The width to height ratio was selected here to provide a reasonable throughput while avoiding significant PDMS sagging.

The HIV particles were produced by transfecting HEK293T/17 cells with four plasmids as described before [102]. Briefly, HEK 293T cells on a 6 cm dish were transfected with 7.2 μg pGag-eGFP, 48 μg pJR-FL, 12 μg pcRev, and 24 μg pR8ΔEnv using the calcium phosphate protocol. Transfected cells were kept in a CO_2 incubator for 48 h, and the supernatant medium was collected, briefly centrifuged to remove cell debris, and passed through a 0.45 mm filter. The viral suspension was then aliquoted and stored at -80 ºC. The infectivity of the HIV viruses was also determined using the β-Gal assay, as described before, to confirm the transfection success [102].

To demonstrate the principle of particle separation based on their intrinsic movements in the vertical direction, single particle suspensions containing either 5 μm polystyrene microbeads or 100 nm polystyrene nanobeads were introduced into the top inlet at different flow rates (3, 6, 10, 15, 20 μl/min) using a syringe pump (Chemyx Inc. Fusion 400, Stafford, TX). The particles were diluted in PBS/0.3% SDS to a final particle concentration of 0.2% (v/v). This concentration of SDS was found to maintain a

dispersed state of the nanoparticles through light scattering analyses (data not shown). Particle free PBS/0.3% SDS was injected into the bottom inlet at the same flow rate. The outflow was collected from the top and bottom outlets individually. The particle concentration was determined by optical absorbance at 470 nm for the microbeads and 545 nm for the nanobeads, respectively, using a UV-Vis spectrometer. These two wavelengths matched the excitation wavelengths of the fluorophores embedded in the particles and the absorbance was found to correlate linearly with the particle concentration in the suspension (data not shown). Since the flow resistances in the two layers are comparable, similar outflow volumes were expected from the two outlets. When the outflow volumes from the two outlets differed by over 20%, the samples were discarded since obstruction inside the device could lead to chaotic flow and significant sample mixing that compromised the separation.

To mimic a blood sample from a subject of viral infection, lab stocks of HIV viruses were spiked into whole blood or 10 times diluted blood by PBS. We also diluted the HIV stock in bare PBS containing 1% BSA. The final viral concentration was ~10^5 HIV virions/mL in all cases. The biological sample was injected into the top inlet of the device at a flow rate of 3 or 6 μl/min, which correlated to sufficient residence time to deplete red blood cells from the top layer. The supporting layer injected from the bottom inlet was PBS for experiments involving blood or PBS/1%BSA for experiments with bare HIV. After collecting the outflow from the top and bottom outlets individually, cells were counted manually under an optical microscope using a hemocytometer and HIV viral concentration was determined using a commercial p24 ELISA kit. The p24 protein comprises the viral capsid and its concentration directly relates to the viral concentration [103].

COMSOL Multiphysics software (COMSOL Inc., Burlington, MA) was utilized to simulate the concentration change of a source containing a diffusive solute in contact with a solute-free drain. A 'Transport of Diluted Species' model was used. The model was set up where both layers were 100 μm thick and 2 mm wide. The top and bottom faces (z=0 and z=200 μm) of composite structure were considered no-slip boundaries. The density and viscosity of both layers were set to be 1 g/cm^3 and 0.001 Pa s. The diffusion coefficients of the solute were calculated using the Stokes-Einstein relation for nano-species of different sizes. To observe the concentration evolution with time, both layers were set to move in the y direction at an average velocity of 0.45 mm/s. Fluid flow was assumed to be steady state, and incompressible, and inertia was neglected. The flow was laminar and fluid velocity in the y direction was not expected to interfere with the intrinsic diffusion of a diluted solute in the z direction. A triangulated mesh of roughly 3.6×10^6 elements was used to ensure solver accuracy.

All experiments were repeated in at least 3 different devices. The averages were shown in the figures, and each error bar represented the standard deviation of the mean.

Table 3 Calculated Peclet numbers for typical biological particles of different sizes under intrinsic movements of sedimentation and diffusion. The terminal velocity and diffusion coefficient were calculated. The parameters used for the calculations are as follows: characteristic length=100 μm (thickness of the biological sample layer tested in the experiments below), solution density=1 g/cm^3, bioparticle density=1.05 g/cm^3 (lower limit for cells and viruses), solution viscosity=0.001 Pa·s, and temperature=296 K.

Species	Cells	Cells	Platelets	Viruses and exosomes			Proteins
Diameter of beads	10 μm	5 μm	1 μm	100 nm	50 nm	20 nm	5 nm
Terminal velocity (nm/s)	2722.2	680.6	27.2	0.3	7.5×10^{-2}	1.2×10^{-2}	7.5×10^{-4}
Diffusion coefficient (m^2/s)	4.39×10^{-14}	8.78×10^{-14}	4.39×10^{-13}	4.39×10^{-12}	8.78×10^{-12}	2.20×10^{-11}	8.78×10^{-11}
Peclet number	1033.4	129.1	1.0	1.1×10^{-3}	1.4×10^{-4}	9.1×10^{-6}	1.4×10^{-7}

Bioparticles in a static suspension undergo two intrinsic movements, sedimentation from gravity and diffusive random walk. When the gravitational force, buoyant force, and drag force are balanced in the z direction, sedimentation of a spherical object moving with a low Reynolds number is characterized by the terminal velocity

$$V_t = \frac{gd^2}{18\mu}(\rho_m - \rho)$$

where g is acceleration of gravity, d is diameter of the sphere, μ is fluid viscosity, ρ_m is density of the sphere, and ρ is density of the fluid. The settling distance of a sphere in the stead state is $V_t t$. The diffusion coefficient of a spherical particle through a liquid of low Reynolds number is characterized by the Stokes-Einstein relation

$$D_{AB} = \frac{k_B T}{6\pi\mu r}$$

where k_B is Boltzmann's constant, T is temperature, μ is fluid viscosity, and r is particle radius. Using the random walk theory, the diffusion length of a sphere is estimated as $2\sqrt{D_{AB}t}$.

To determine which intrinsic transport process dominates for a suspended particle of a particular size, Peclet number, Pe, is calculated

$$Pe = \frac{UL}{D_{AB}}$$

where U is terminal velocity, L is a characteristic length, and D_{AB} is the particle diffusion coefficient. Using a characteristic dimension of 100 μm (thickness of the biological sample layer tested in the experiments below), solution density of 1 g/cm^3, particle density of 1.05 g/cm^3 (lower limit for biological particles), and solution viscosity of 0.001

Pa·s, Pe for different sized bioparticles under intrinsic movements of sedimentation and diffusion were calculated and shown in Tab. 3.

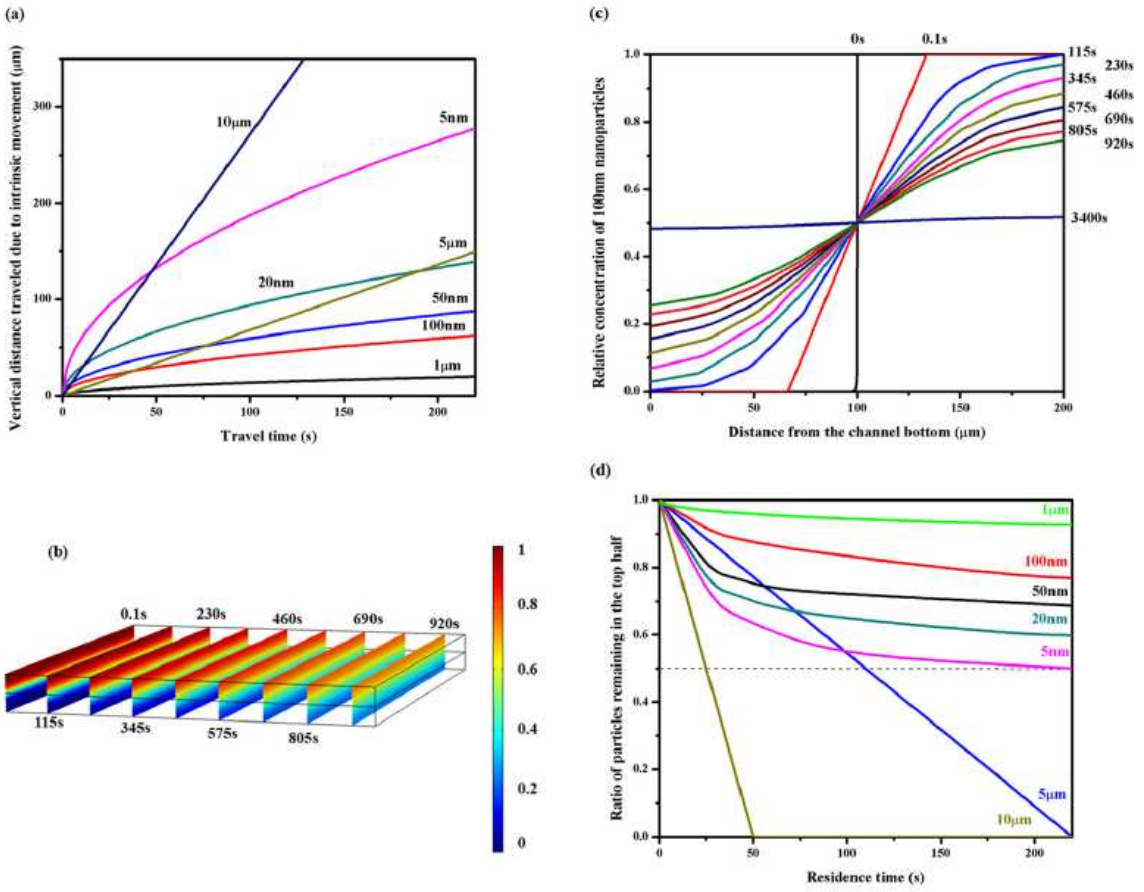

Figure 4 Numerical analysis of the concentration change for different sized particles in a two layer structure. (a) Vertical distance traveled by bioparticles of various sizes in water due to intrinsic movements. The travel distances were calculated using the sedimentation or diffusion equations presented in the text. (b) COMSOL simulation showing the concentration evolution for a two layer structure where a suspension containing a diffusive solute was layered on a carrier fluid. The solute diffusion coefficient was set to be 4.39×10^{-12} m^2/s, corresponding to that of the 100 nm particles in water. The density and viscosity of the medium was set to be 1 g/cm^3 and 0.001 Pa·s. The convection velocity in the y direction was set to be 46 μm/s so the concentration profiles after different contact time could be plotted. The color indicates the relative concentration and the slices correspond to various time points post initiation of diffusion. The diffusion times were labeled next to the slices. (c) The concentration profile along the z direction dissected from (b) with the diffusion time labeled on the right. It takes over 3400 s for 100 nm particles to reach the concentration equilibrium in the simulated geometry. (d) COMSOL simulation showing expected particle concentration remaining in the top layer at different time points. A ratio of 0.5 (dashed line) indicates no preferential particle residence. The numerical analysis suggests that bioparticles with diameters of 5–10 μm sediment to the bottom layer in ~200 s while over 50% of the nanoparticles remain in the top layer. The relative nanoparticle concentration remaining in the top layer depends on its size or diffusion coefficient.

The distinct Peclet numbers for cells and bionanoparticles indicate that their intrinsic movements are dominated by different transport processes. Specifically, the Peclet

number is much greater than 1 for blood cells a few micrometers in diameter, i.e., their movements are dominated by sedimentation in a medium with density and viscosity comparable to water. For typical blood cells 6–9 μm in diameter and having a density of 1.05–1.1 g/cm^3 suspended in PBS, the terminal velocity is found to be in the range of 0.98–4.41 μm/s. While it takes ~10^{-4} second for blood cells to reach the terminal velocity, this duration is very short compared to the sample residence time in our experiments and is neglected in the following analyses. Thus, when a diluted suspension of cells is layered on top of a buffer cushion, the cell concentration will decrease linearly with time in the original sample (Fig. 4d).

On the other hand, nanoparticles on the order of 100 nanometers in diameter or smaller have a Peclet number much smaller than 1, suggesting their intrinsic movements in a physiological solution is mostly diffusive. We calculated the diffusion coefficients of a few nanoparticles with biologically relevant sizes (Tab. 3) using the Stokes-Einstein relation. Next, we set up a COMSOL model in which a source suspension containing a diffusive solute was layered on top of a drain free of solute, both fluid layers being 100 μm thick. The concentration evolution in the two layer structure was then simulated as a function of time. Fig. 4b demonstrates the cross sectional concentration maps in the composite structure at various time points post the initiation of contact using the diffusion coefficient calculated for 100 nm particles in water. Fig. 4c shows the vertical concentration change for 100 nm spheres extracted from the middle plane along the flow direction in Fig. 4b. It is clearly observed that equilibrium is not reached before 3400 s for 100 nm spheres to diffuse through a 100 μm thick drain. The nanoparticles preferentially locate in the source region before they homogenize in both layers. The concentration curves were then used to calculate the ratio of nanoparticles remaining in the source layer. Similar operation was performed using diffusion coefficients corresponding to different sized

nanoparticles, and Fig. 4d summarizes their concentration drop from the source layer with time. For comparison, the concentration changes for cell sized particles in the top half are included in the same figure.

Comparing their concentration behavior in the two layer geometry, it was observed that the concentration of cell sized particles drops faster in the top layer than nanoparticles, as long as the residence time is beyond the cross point (Fig. 4d). For 100 nm particles, the cross point is about 1 s. For a residence time of ~200 s, >90% of 5 μm spheres settle to the bottom layer, while the concentration of 100 nm particles in the top 100 μm layer only dropped by 20%. Thus, bionanoparticles around 100 nm in diameter can be purified from cells with a significant yield using the simulated geometry based on intrinsic particle transport. It should be pointed out that the above analysis is over-simplified since particle interactions were neglected; thus, it is only applicable to dilute suspensions. Nonetheless, it provides useful insight into intrinsic particle movement on the microscale. We next implemented a microfluidic chip to test the theoretical analysis using synthetic and biological particles.

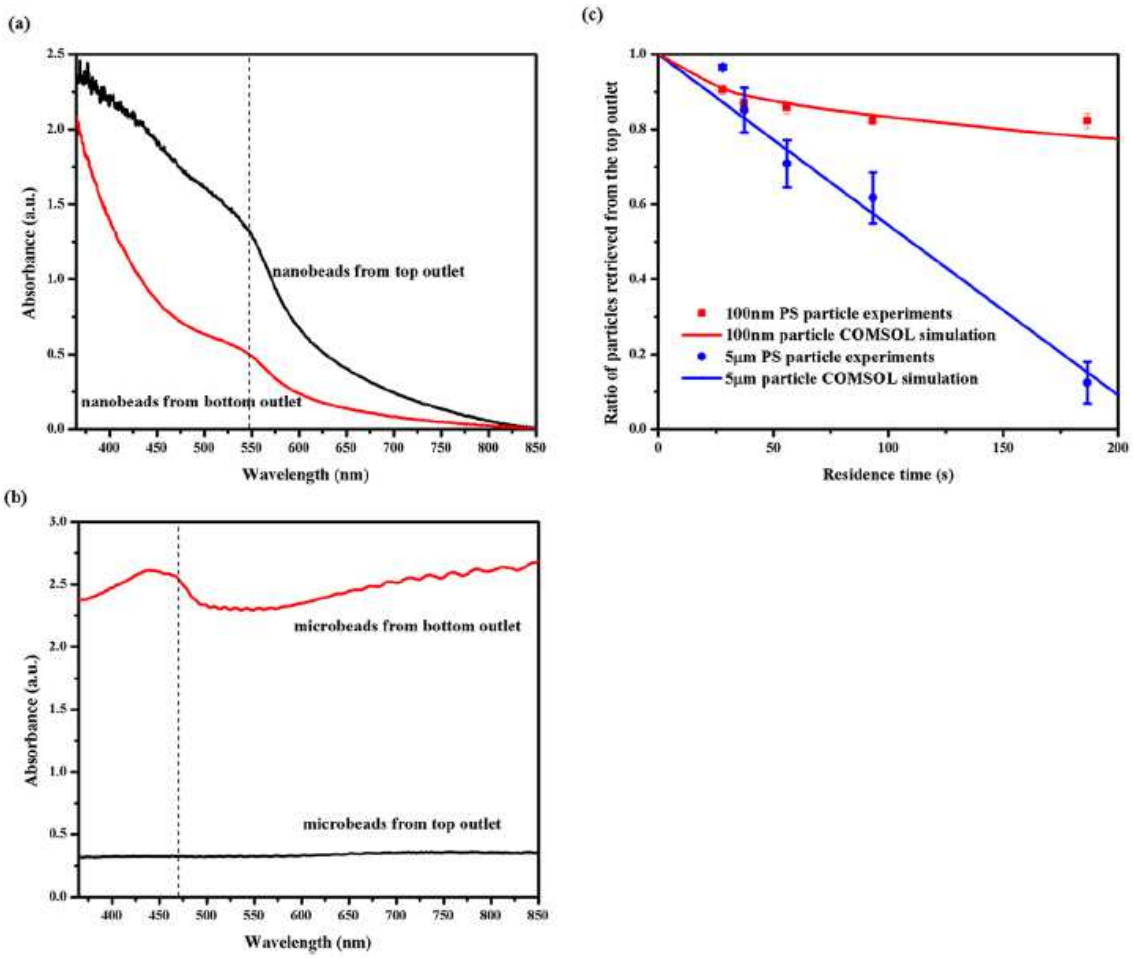

Figure 5 Representative UV-Vis absorption spectra of (a) nanoparticle and (b) microparticle suspensions retrieved from the microchip at a flow rate of 3 μl/min. The 100 nm polystyrene nanoparticles were labeled with Firefli™ Fluorescent Red (Ex 542/Em 612 nm) and 5 μm polystyrene microparticles were labeled by Firefli™ Fluorescent Green (Ex 468/Em 508 nm). Suspensions containing a single type of synthetic particles were injected into the top inlet of at 3 μl/min. The outflow from the top and bottom outlets were analyzed by UV-Vis spectroscopy and repetitive spectra are presented. The absorbance at 545 nm for nanoparticles and 470 nm for microparticles were used to quantify their concentrations since they correlated linearly with the particle concentration. Similar spectra were acquired for other flow conditions. (c) Experimental data (solid dots and solid squares) showing the ratio of particles retrieved from the top outlet at different residence time points. PBS/SDS solutions containing either 5 μm or 100 nm polystyrene particles were injected into the top inlet and particle free PBS/SDS solution was injected into the bottom inlet. The two layers had identical flow rates of 20, 15, 10, 6, and 3 μl/min, and the particle residence time in the devices were calculated for the plot. Each data point was repeated in at least 3 devices, and error bars represent standard deviations from these repeats. The experimental measurements closely matched results from COMSOL simulation (blue and red lines).

To test the numerical analysis described above, we constructed a microfluidic chip in which a biological sample was layered on top of a support fluid to purify viral particles from cells based on their intrinsic movements in the vertical direction. The purpose of the support fluid was to carry away cells but kept most of the viral particles in the top layer

sample. Both layers were 100 μm thick, similar to the simulated structure. The two layer sample was also horizontally transported in a laminar flow to allow continuous sample processing. The Reynolds number was <0.045 for all the flow rates tested in our work; thus, the convection was not expected to significantly influence the intrinsic vertical movement of the particles in a dilute suspension. We first used suspensions containing polystyrene spheres either 5 μm or 100 nm in diameter diluted in PBS/0.3% SDS at a particle concentration of 0.2% (v/v). The particle sizes were selected to mimic blood cells and HIV viral particles, respectively. The density of the polystyrene beads, 1.05 g/cm^3, is on the low end of the cell density range (1.05–1.1 g/cm^3), so they represent the population with a slow sedimentation rate. The suspension was injected into the top inlet, while an identical buffer containing no sphere was used as a carrier solution in the bottom layer. The flow rates for both layers were the same at 20, 15, 10, 6, or 3 μl/min, and the corresponding sample residence times in the device were 28, 37, 56, 93, or 187 s. The outflows from the top and bottom halves were collected, and the particle concentration was determined by suspension absorbance at 470 nm for the microspheres and 545 nm for the nanospheres (Fig. 5a and 5b). The ratio of particles remaining in the top layer at various residence time points was plotted in Fig. 5c. It was observed that the concentration of 5 μm microspheres decreased nearly linearly in the original sample (circles in Fig. 5c), while the concentration of 100 nm nanospheres decreased gradually, following a diffusive behavior (squares in Fig. 5c). In both cases, the change of particle concentration in the top layer closely matched the prediction from COMSOL simulation (lines in Fig. 5c). At a residence time of 187 s, the concentration of microspheres dropped to <10% in the top outflow, but >80% of the nanospheres was retrieved from the same outlet. When microbeads and nanobeads were mixed together at a total particle concentration of 0.2% and introduced from the top outlet, comparable separation result was observed visually, while it was difficult to quantify the two species

independently due to their overlapping UV-Vis absorption spectra. Another limitation of the analyses using synthetic particles was the adhesion of polystyrene spheres to the PDMS floor at a flow rate lower than 3 μl/min, despite the use of SDS. Thus, no residence longer than 187 s, which corresponds to the flow rate of 3 μl/min, was tested, although longer residence time was expected to further improve the nanosphere purity with only a slight drop in the yield.

Following the success in synthetic particle separation, we then spiked HIV viruses into healthy donor's blood to mimic a blood sample from an HIV infected subject. Red blood cells (RBCs), the most abundant cell species in blood, have a density of 1.09–1.1 g/cm^3 and a terminal velocity of 2.45 μm/s in PBS buffer. The sedimentation rate of RBCs in plasma is slowed down to 1.63 μm/s due to higher viscosity (1.2 Pa·s) and density (1.025 g/cm^3) of plasma [104]. Even so, it should only take RBCs ~60 s to settle 100 μm. Thus, the two flow rates of 6 and 3 μl/min, corresponding to residence times of 93 and 187 s, were selected to separate blood cells from HIV viral particles.

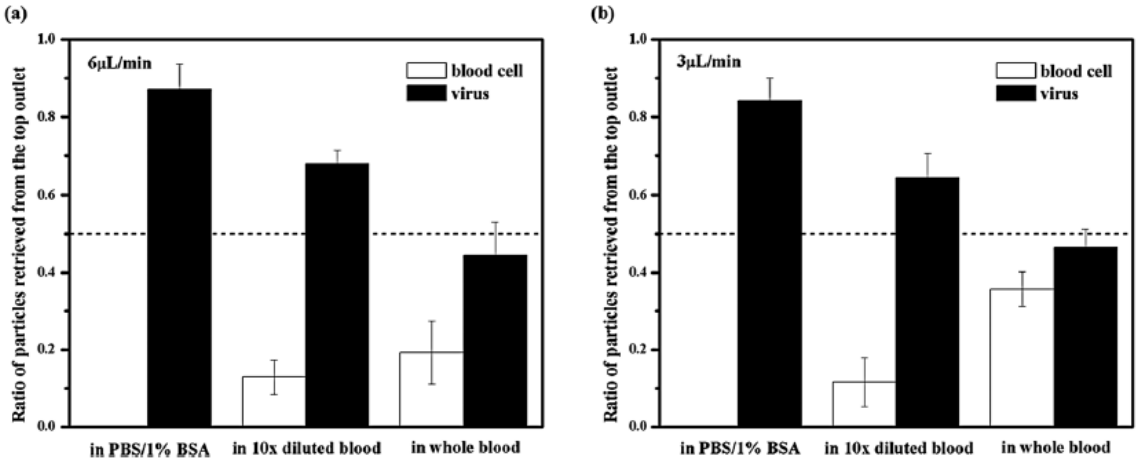

Figure 6 Relative ratios of blood cells and HIV viral particles retrieved from the top outlet. The biological samples were injected into the top inlet and PBS (for experiments containing blood) or PBS/1% BSA (for blood free experiments) was injected into the bottom. Both layers had identical flow rates of either 6 μl/min (a) or 3 μl/min (b). (a) At a flow rate of 6 μl/min, 87.3±6.3% of HIV viral particles were retrieved from the top outlet in the absence of blood cells. When HIV particles were spiked in blood diluted ten times by PBS, 68.2±3.3% of viruses and 12.8±4.4% of blood cells were retrieved from the top outlet. In whole blood, 44.4±8.7% of viruses and 19.2±8.2% of blood cells were retrieved from the top outlet. (b) When the flow rate was 3 μl/min for both layers, 84.2±5.8% of HIV viral particles were retrieved from the top outlet in the absence of blood cells. When HIV particles were spiked in blood diluted ten times by PBS, 64.5±6.0% of viruses and 11.6±6.3% of blood cells were retrieved from the top outlet. In whole blood, 46.5±4.7% of viruses and 35.7±4.5% of blood cells were retrieved from the top outlet.

First, we spiked HIV particles in blood diluted ten times in PBS and injected it into the top inlet of the device. The carrier buffer in the bottom layer was PBS. As shown in Fig. 6, when both layers were flowed at 6 μl/min (residence time 93 s), nearly 90% of the blood cells moved out of the top layer, while nearly 70% of HIV particles remained in this layer. At a slower flow rate of 3 μl/min or a residence time of 187 s, both the blood cell and viral concentration in the top layer dropped slightly. As a control, we also diluted the HIV stock using PBS/1% BSA and injected it into the top inlet of the device. In this case, the carrier buffer was PBS/1% BSA. In the absence of blood cells, 87.3±6.3% and 84.2±5.8% of viral particles remained in the top layer under a flow rate of 6 μl/min and 3 μl/min, respectively. The compromised viral yield in 10× diluted blood is likely a result of collisions with cells, which accelerates nanoparticle mixing in the vertical direction. In addition, collisions between cells also hamper their unidirectional settling [105]. As a result,

cell contamination was found in the top layer despite sufficient residence time for red blood cells to completely settle out of this layer in theory. Switching the biosample to the bottom layer while flowing the buffer from the top inlet may improve the purity of virus retrieved from the top outlet, but the maximum yield is expected to drop to 50% accordingly.

Accelerated nanoparticle mixing and disturbed cell sedimentation was further exaggerated in whole blood. When the top layer contained HIV spiked in whole blood, about 50% viral particles and 19% blood cells were retrieved from the top outlet for a residence time of 93 s. At a longer residence time of 187 s, the blood cell contamination from the top outflow increased to 30%. The even worse separation at slower flow rate was caused by unsteady convection. At 3 μl/min, blood cell movement was often observed pulsatile in the device. This was likely a result of a significant increase of blood viscosity at low shear rates [106], which led to high flow resistance in the cell-rich region and unpredictable flow patterns. Besides particle collisions, another factor that may contribute to the poor separation in whole blood is the unmatched density between plasma and the bottom carrier fluid, which could cause the blood layer to collapse. Increasing both the bottom layer density and the residence time may alleviate this problem. Unfortunately, it was hard to test this hypothesis with the current design given the unsteady flow at the low flow rate. Future designs that allow longer residence time but still maintain a high shear rate will be evaluated with different carrier fluid compositions for whole blood processing.

The device presented here purifies bionanopaticles from blood cells in a diluted suspension where particle collisions are insignificant. Using HIV particles for demonstration here, we envision that the principle can be applied to the purification of other submicron species in blood. It should be noted that the nanoparticle yields

decrease with their diameters in a device of a fixed dimension (Fig. 4d). For example, in the current microdevice of a 100 μm thick channel in each layer, the theory predicts retrieval of >80% of 100 nm particles from the top outlet after 187 s, but homogenized presence of 5 nm particles throughout the thickness. Nonetheless, since the diffusion and sedimentation distances always cross regardless of the nanoparticle size (Fig. 4a), it will be possible to separate them using the described principle. At least 50% of the nanoparticle target could be retrieved from the nature of diffusion and the yield can be improved by optimizing the device dimension for a specific target size.

In conclusion, we take advantage of the intrinsic differences in their movements to purify viral particles from a blood sample in a microfluidic chip. The two layer flow design allows continuous sample processing and extraction of a high proportion of the target particles. The mechanism can be easily applied to effectively purify other submicron species from blood cells. The capability of continuous separation and >50% yield without significant instrument requirement makes the design suitable for processing small volume and low concentration targets at resource limited settings.

2.1.3 Acknowledgements

We are grateful for the helpful discussions with Professor James Gilchrist. The HIV viral stock was kindly prepared by Yi Hu. Funding for the research was provided by National Institute of Health under Grant No. NIAID-1R21AI081638.

2.2 Gravity induced swirl of nanoparticles

2.2.1 Introduction

Parallel flows of two fluids in microfluidic devices are used for miniaturized chemistry, physics, biology and bioengineering studies, and the streams are often considered to remain parallel. However, as the two fluids don't always have the same density, interface

reorientation induced by the density stratification is unavoidable. In this paper, flow characteristics of an aqueous polystyrene nanofluid and a sucrose densified aqueous solution flowing parallel in microchannels are examined. Nanoparticles 100 nm in diameter are used in the study. The motion of the nanoparticles was simulated using the Lagrangian description and directly observed by a confocal microscope. Matched results were obtained from computational and empirical analysis. Although solution density homogenizes rapidly resulting from a fast diffusion of sucrose in water, the nanofluid was observed to rotate for an extended period. Angular displacement of the nanofluid depends on the ratio of gravitational force to viscous force, Re/Fr^2, where Re is the Reynolds number and Fr is the Froude number. In the developing region at the steady state, the angular displacement is related to y/D_h, the ratio between distance from the inlet and the hydraulic diameter of the microfluidic channel. The development of nanofluid flow feature also depends on h/w, the ratio of microfluidic channel's height to width. The quantitative description of the angular displacement of nanofluid will aid rational designs of microfluidic devices utilizing multi-stream, multiphase flows.

2.2.2 Results and conclusion

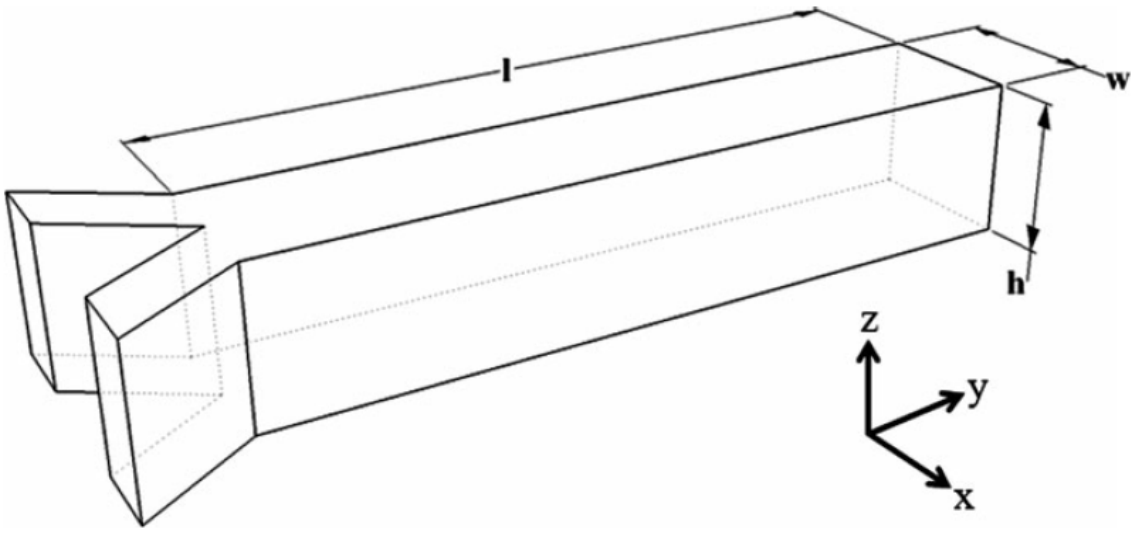

Figure 7 A schematic of microfluidic devices used in this study. All devices contain a Y-junction merging into a main channel. Two main channel geometries, 40 mm × 2 mm × 200 μm, and 40 mm × 200 μm × 160 μm (l × w × h) were used in our work with the cross-sectional aspect ratios of 0.1 and 0.8, respectively

Microfluidic devices were fabricated (Fig. 7) using the standard soft lithography technique. First, SU-8 photoresist was patterned on a silicon wafer by photolithography to form a negative mold. Next, a 10:1 mixture of poly(dimethylsiloxane) (PDMS) prepolymer and curing agent was poured onto the mold and baked at 70 °C until cured. After cutting and removing the PDMS channels from the SU-8 mold, the channels were bonded permanently to glass slides through oxygen plasma at a forward power of 50W and pressure 100mT above the base pressure for 30 seconds. The channels were then blocked with 1% BSA in PBS to reduce nonspecific binding on the channel walls before further experiments.

Devices used in this study contain a Y-junction merging into a main channel, as shown in Fig. 7. Two main channel geometries were tested with dimensions of 40 mm × 2 mm × 200 μm, and 40 mm × 200 μm × 160 μm (length × width × height), respectively. The corresponding cross-sectional aspect ratios (*h/w*) are thus 0.1 and 0.8. Polystyrene nanoparticles were diluted in PBS/0.3% SDS to a final particle concentration of 0.2% (v/v). This concentration of SDS does not affect the Newtonian property of the fluid [107],

but helps to maintain a dispersed state of the nanoparticles as confirmed by light scattering measurements (data not shown). The solution of 25% sucrose was made by dissolving sucrose in PBS/0.3% SDS.

To study nanoparticle transport in the devices, the nanofluid containing polystyrene beads was injected from one inlet, and the aqueous sucrose solution was injected from the other by a syringe pump (Chemyx Inc. Fusion 400, Stafford, TX). BD Luer-Lok™ 1mL syringes (Franklin Lakes, NJ) were used for sample injection when flow rates were higher than 0.1 μL min^{-1}. Lower flow rates were introduced by VICI C-160 10μL syringes (Houston, TX). Confocal images were taken on a fluorescent confocal microscope (Olympus IX81, Center Valley, PA). The images from the same *y* coordinates were automatically processed by FLUOVIEW Viewer (Center Valley, PA) to form the cross-sectional images.

Table 4 Properties of fluid and nanoparticles in simulation

Properties	Value
Density of water	**1,000 kg m^{-3}**
Viscosity of water	**1.0 cP**
Density of 25% sucrose	**1,100 kg m^{-3}**
Viscosity of 25% sucrose	**2.5 cP**
Density of nanoparticles	**1,100 kg m^{-3}**
Diameter of nanoparticles	**100 nm**
Drag coefficient	**0.47**
Mass diffusion coefficient of sucrose	**$2.14\text{-}5.22\times10^{-10}$ m^2s^{-1}**

ANSYS Fluent (ANSYS Inc., Canonsburg, PA) was employed to simulate steady state 3-D laminar flows of two miscible fluids in the developing and fully developed regions. The main channel geometries used in the experiments without branching inlets were created as a computational domain by ANSYS DesignModeler. The particle tracking theory with Eulerian-Lagrangian approach was employed. The main fluid (continuum phase) was treated using Eulerian description and the dispersed particles (discrete phase) were

tracked using the Lagrangian description. Two-way coupling was employed in our modeling, where the continuum phase could affect the behavior of discrete phase (nanoparticles), and vice versa. Hence, in this process a proper designed solver calculated the continuous and discrete phase equations in an alternate manner until a converged coupled solution was achieved. Particles in Fluent are treated as volumeless points, but size effect is incorporated in the equations of Brownian, drag, lift and buoyant forces. Given the low particle concentration (0.2 %) and much larger channel geometry compared to the particle size, particle-particle and particle-wall interactions are negligible. Thus, it is reasonable to ignore the particle volume for particle tracking. Gravitational acceleration was set as 9.8 kg m^{-3}. Since the buffer solution used in the experiments has comparable density and viscosity as water, side-by-side uniform flow of 25% sucrose (ρ = 1,100 kg m^{-3}, μ = 2.5 cP) and water (ρ = 1,000 kg m^{-3}, μ = 1.0 cP) was introduced as the inputs in the simulation with equal flow rates. Mass-weighted-mixing law was applied to account for the viscosity evolution, and volume-weighted-mixing law was applied to form the density evolution. Velocity of constant magnitude normal to *x-z* plane was applied at the inlets. Nanoparticles 100 nm in diameter were introduced together with water at a mass flow rate of 10^{-11} kg s^{-1}. The volume fraction of the nanoparticles is 0.2%. The density and viscosity of the nanofluid is 0.1 kg/m^3 and 5×10^{-3} cP [108] higher than those of base fluid, respectively. As these differences are negligible, density and viscosity of the base fluid (water) are applied to the nanofluid (Tab. 4). No-slip stationary wall with reflecting boundary condition type for nanoparticles was chosen. Zero pressure was set at the outlet.

Steady creeping flow of the two streams was modeled by the two-way coupling laminar flow module. The equations governing the conservation of mass and momentum of the liquid phase are [109,110]

$$\nabla \cdot (\rho \vec{u}) = 0$$

$$\nabla \cdot (\rho \vec{u}\vec{u}) = -\nabla p + \nabla \cdot (\bar{\bar{\tau}}) + \rho \vec{g} + \sum \left(F_D \left(\overrightarrow{u_p} - \vec{u} \right) \right) \dot{m}_p \Delta t$$

$$Re_p = \frac{\rho d_p \left| u_p - u \right|}{\mu} \quad and \quad F_D = \frac{18\mu}{\rho_P d_p^2} \frac{C_D Re_p}{24}$$

where ρ is the fluid density, μ is the molecular viscosity of the fluid, $\vec{u}$ is the fluid phase velocity, p is the static pressure, $\bar{\bar{\tau}}$ is the stress tensor, $\rho \vec{g}$ is the gravitational body force, $\overrightarrow{u_p}$ is the particle velocity, ρ_P is the density of the particle, d_p is the particle diameter, C_D is the drag coefficient, $\dot{m}_p$ is the mass flow rate of the particles, Δt is the time step, $F_D \left(\vec{u} - \overrightarrow{u_p} \right)$ is the drag force per unit particle mass and Re_p is the relative Reynolds number. The last term in the second equation is the momentum source term that represents the influence of the particles on the flow field of fluids.

Diffusion of sucrose into water was modeled by the species transport module:

$$\nabla \cdot (\rho \vec{u} Y_i) = -\nabla \cdot \left(-\rho D_{i,m} \nabla Y_i \right)$$

where Y_i is the local mass fraction of each species, and $D_{i,m}$ is the mass diffusion coefficient for species i in the mixture.

Discrete phase module was used to track the movement of particles:

$$\frac{d\overrightarrow{u_p}}{dt} = F_D \left(\vec{u} - \overrightarrow{u_p} \right) + \frac{\vec{g} \left(\rho_p - \rho \right)}{\rho_p} + \overrightarrow{F_b} + \overrightarrow{F_l}$$

$$F_{b_i} = \zeta_i \sqrt{\frac{\pi S_0}{\Delta t}} \quad and \quad S_0 = \frac{216 \mu k_B T}{\pi^2 \rho^2 d_p^5 \left(\frac{\rho_P}{\rho} \right)^2 C_c}$$

$$\overrightarrow{F_l} = \frac{2K(\mu/\rho)^{1/2} \rho d_{ij}}{\rho_p d_p (d_{lk} d_{kl})^{1/4}} \left(\vec{u} - \overrightarrow{u_p} \right)$$

where $\overrightarrow{F_b}$ is the Brownian force per unit particle mass [111], $\overrightarrow{F_l}$ is the Saffman's lift force per unit particle mass due to shear [112], K=2.594, ζ_i are zero-mean, unit-variance-independent Gaussian random numbers, T is the absolute temperature of the fluid, k_B is the Boltzmann constant, C_c is the Stokes-Cunningham slip correction, and d_{ij} is the deformation tensor. For comparison, nanoparticles were replaced by molecules (MW = 479 Da) and microparticles (d_p = 10 μm) to study size dependence of the particle motion. Similar to the above procedures, laminar, species transport and discrete phase models were applied to simulate the motion of microparticles, while laminar and species transport models were used for molecular studies. Iterative calculations to solve Navier-Stokes equations were carried out by the SIMPLE scheme for pressure-velocity coupling. Contours of Discrete Phase Model concentration were saved at different cross sections.

Following previous studies [60–63], we hypothesize that the spatial characteristics of the nanofluid are influenced by Re/Fr^2 ($=D_h^2 g\Delta\rho/\mu v$), the ratio of the gravitational force to the viscous force, y/D_h, dimensionless entrance distance and h/w, the aspect ratio of microfluidic channel. Here D_h is the hydraulic diameter of the channel, $g\Delta\rho$ is the buoyancy constant, μ is the viscosity of the mixture, v is the average velocity of fluid flow along the main channel, y is the entrance length along the channel, h is the channel height, and w is the channel width. Since the two streams were introduced at the same flow rate, the ratio of average velocity between the two streams is unity and its effect on the nanoparticle dynamics and the flow structure was not investigated here.

Table 5 Predicted nanoparticle distribution with different mesh sizes

Number of elements	Mesh size (μm)	Predicted nanoparticle distribution
37,800	**32**	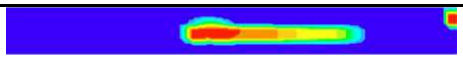
327,600	**16**	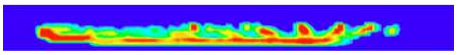
2,500,000	**8**	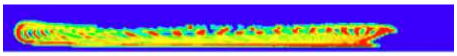
20,000,000	**4**	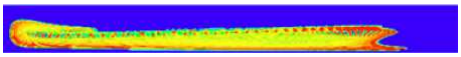

In order to check the spectral convergence, nanoparticle distribution was simulated using different mesh sizes of 32 μm, 16 μm, 8 μm and 4 μm in a microchannel with h/w= 0.1, y/D_h = 0.5 and Re/Fr^2 = 1109. The particle size distribution was found to be comparable for mesh size of 8 μm and 4 μm (Tab. 5). Thus, 8 μm mesh size is sufficient to achieve the spectral convergence, and the numerical results presented below were generated using the mesh size of 8 μm.

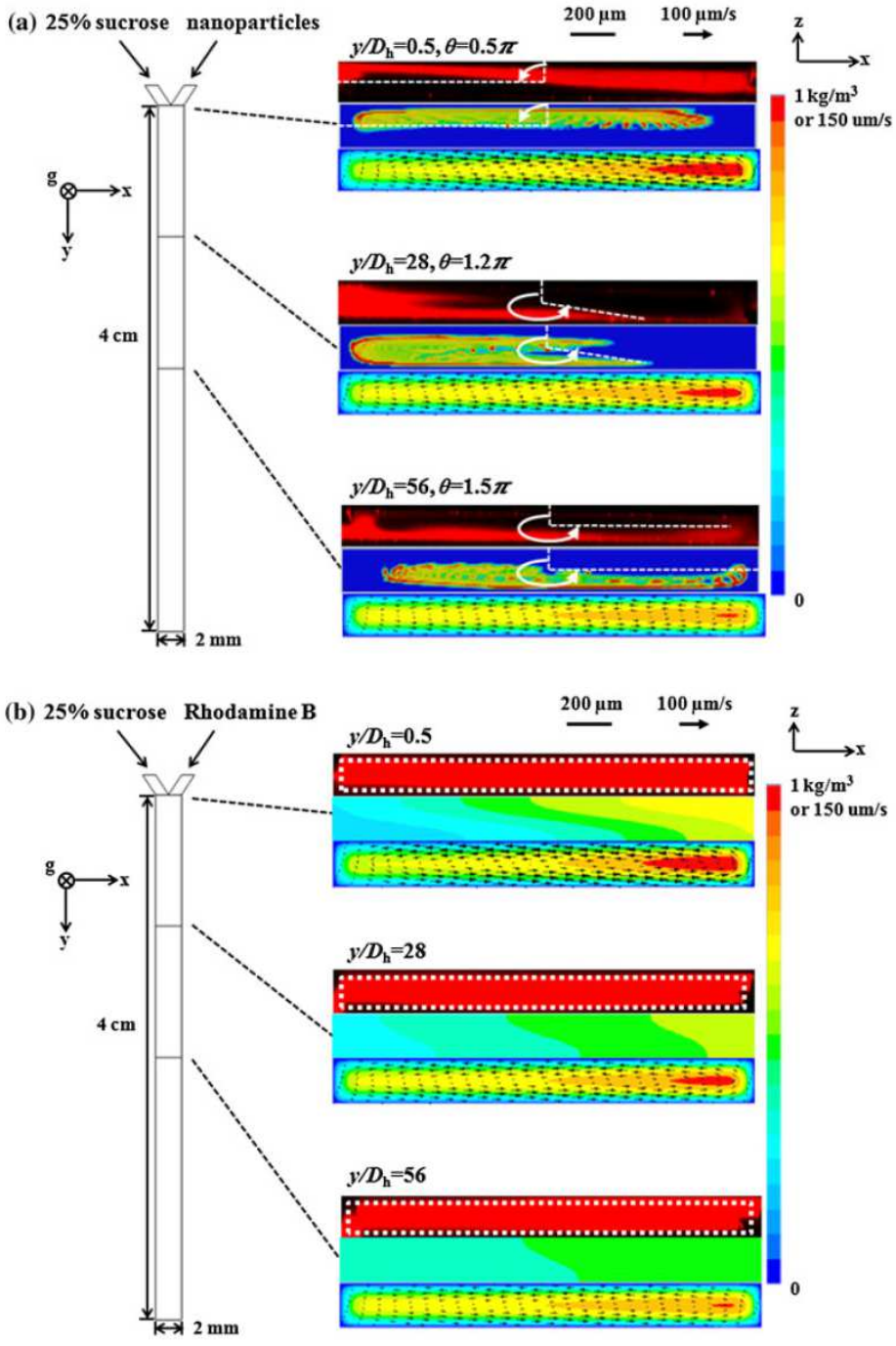

Figure 8 (a) (Left) A schematic showing the top view of the microchannel. (Right) Confocal images (top image of each group) and predicted contours (middle image of each group) of nanoparticle distribution at three locations corresponding to y/D_h=0.5, 28, 56. In-plane velocity vectors with velocity contours in the *y* direction are shown as the bottom images of each group. The swirling motion of the nanoparticles follows the in-plane fluid motion. The range of the color scale bar is from 0 to 1 kg m^{-3} for the nanoparticle distribution maps (middle of each group), and 0 to 180µm s^{-1} for the out of plane velocity. (b) Confocal images (top image of each group), predicted contours (middle image of each group) and secondary flow vector with *y* direction velocity contours (bottom image of each group) of a small fluorescent molecule, Rhodamine B, along the flow direction. Rhodamine quickly equilibrates in the cross-sectional image. In both (a) and (b), h/w=0.1 and Re/Fr^2=1109

First, nanoparticle migration was examined in a channel with a cross-sectional dimension of 200 μm (*h*) by 2 mm (*w*), which corresponds to an aspect ratio (*h/w*) of 0.1. A 25% sucrose solution and the nanofluid were injected into the two arms of inlets by a syringe pump, and flow rates of the two fluids were kept the same and constant. After the flow reached a steady state, confocal fluorescent images were taken in the *x-z* plane at different *y* positions. In comparison, numerical simulations were run for the same geometry and flow condition. Fig. 8a shows the measured and predicted nanoparticle distribution at three *x-z* planes normal to the flow direction, y=0.5 D_h, 28 D_h, and 56 D_h, respectively. The volume flow rate was 0.96 μL min^{-1} and Re/Fr^2 was 1109. A viscosity value of 1.46 cP was used to calculate Re/Fr^2. This value corresponds to the viscosity of 12.5% sucrose. It was picked considering fast diffusion and homogenization of small molecules with our experimental parameters, as observed in Fig. 8b. Thus nanoparticle motion mostly happens within 12.5% sucrose except for a short distance near the device inlets. The top image of each panel from confocal microscopy denotes the concentration distribution of nanoparticles; the middle image is the predicted nanoparticle concentration contour from simulation. The two match well in all *x-z* planes. The bottom graph of each panel shows the in-plane velocity vectors overlapped on the out-of-plane velocity contours.

As observed in Fig. 8a, the interface between the nanofluid and sucrose solution quickly reorients from the vertical direction. The fluorescent nanoparticles reside on the top half of the channel at y/D_h ~1, which corresponds to fully developed reorientation in previous reports when Re/Fr^2 is on the order of 1 [61]. With Re/Fr^2 on the order of 1000 here, the nanoparticles continue to rotate in the *x-z* plane along the sides of the cross-section till the device outlet. For comparison, Rhodamine B was used in the place of nanoparticles in the lower density stream and its distribution was found to equilibrate at y/D_h ~1 by confocal microscopy (Fig. 8b). As the molecular weight of Rhodamine (MW=479 Da) is

comparable to that of sucrose (MW=342 Da), this suggests that the density mismatch disappears within a short distance from the fluid converging point, due to fast diffusion of sucrose.

To understand the long lasting motion of the nanofluid, the fluid velocity field was studied and presented as the bottom image of each panel in Fig. 8a. The in-plane velocity vectors display a counterclockwise swirling pattern induced by the initial density stratification. As fluids travel along the channel, magnitude of the in-plane velocity gradually decreases, but remains undeveloped even near the device outlet. At the same time, the out-of-plane velocity develops from an asymmetrical profile to the Poiseuille flow. The same rotational direction of the fluid and nanoparticles suggests that the nanoparticles follow the fluid motion.

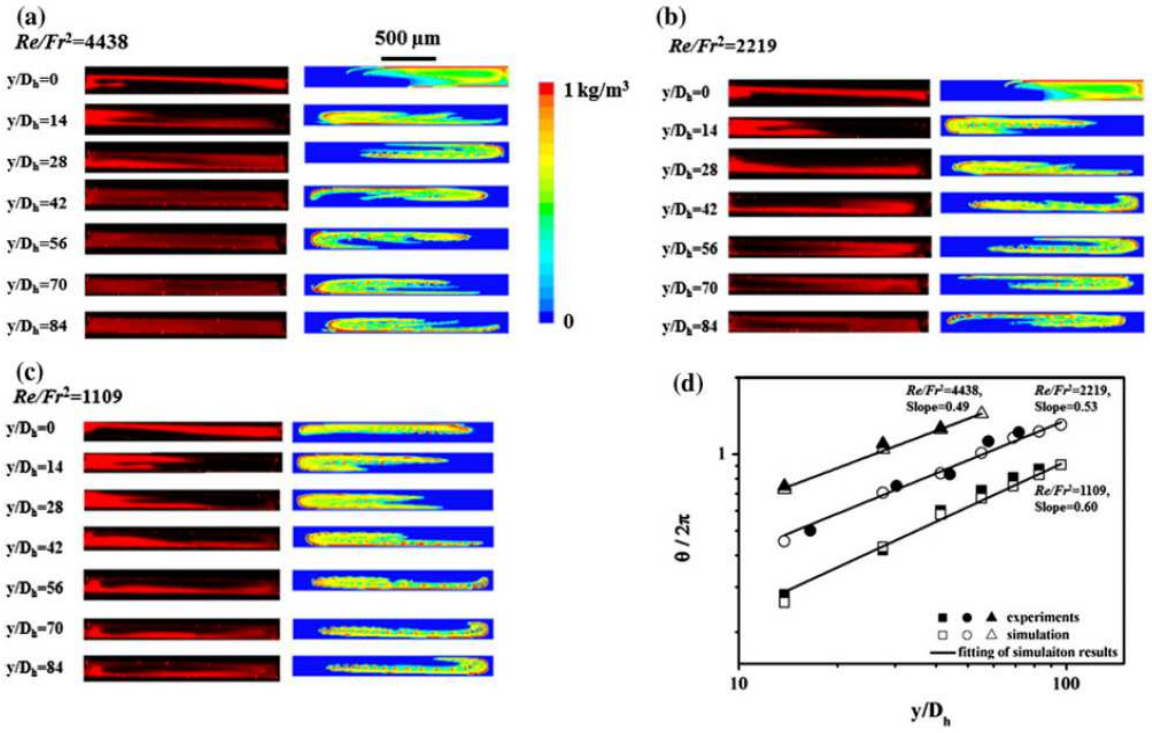

Figure 9 (a-c) Confocal images (left) and predicted contours (right) of particle distributions in developing regions for Re/Fr^2=4438 (a), 2219 (b), and 1109 (c). Good match between the two are observed. (d) The angular displacement (θ) as a function of dimensionless distance from the inlet y/D_h for Re/Fr^2=1109 (squares), 2219 (circles), and 4438 (triangles). The empty symbols are from simulation and solid symbols from experiments. Allometric fitting of the simulation data points is also shown as solid lines

As the input flow rate changes, reorientation pattern of the nanofluid changes accordingly. Fig. 9a-c shows the swirling pattern of nanofluid at three different flow rates, corresponding to Re/Fr^2 = 4438, 2219, and 1109. The angular displacement (θ) of the nanofluid in the developing region was quantified using the leading edge of the fluorescent region [113] as shown in Fig. 8a. The relationship between θ and the dimensionless translational distance (y/D_h) is presented in Fig. 9d in the log-log scale using all images with clear rotational fronts. The empty symbols are from simulation and solid symbols from experiments. It is observed that as Re/Fr^2 increases or input flow rate decreases, the nanofluid experiences greater angular displacement at the same y/D_h. With all three Re/Fr^2 values tested in this work, the nanofluid swirl does not reach the fully developed state even at the device outlet. Furthermore, linear relationships between θ and y/D_h in the log-log scale are observed for all three Re/Fr^2 in the developing region. An allometric fitting of the simulation results (lines in Fig. 9d) indicates that the powers at Re/Fr^2 of 4438, 2219, and 1109 are 0.49, 0.53 and 0.60, respectively. The less-than-unity power indicates deceleration of the nanofluid rotation, which matches the in-plane velocity profile (Fig. 8a). This also supports that nanoparticle motion is driven by gravity induced fluid flow.

The initial nanofluid reorientation is driven by the density stratification until the densifier (sucrose) homogenizes. From Fig. 9, it is observed that greater Re/Fr^2 promotes more reorientation. Greater Re/Fr^2 implies higher gravitational force relative to viscous force, and thus more in-plane fluid momentum to drive the nanofluid swirling. Compared to the work by Yoon *et al.*, in which the lighter fluid rotates up to $\pi/2$ in the fully developed state, we observed much greater reorientation angles. This difference results from pronounced diffusion of the densifier in our work: a uniform density is reached before the angular displacement reaches $\pi/2$, thus momentum acquired from initial density

stratification continues to drive the motion of the nanofluid. On the other hand, diffusion is negligible in Yoon's work. It is difficult for the lower density fluid to overcome the gravitational force and re-orientate beyond $\pi/2$.

After the sucrose concentration reaches equilibrium in the channel, the nanoparticles experience several in-plane forces, including the drag force, gravitational force, buoyancy force, and Brownian force, among which the drag force dominates. This in-plane drag force decelerates nanofluid rotation, thus the power between θ and y/D_h is less than one. Yoon *et al.* reported a constant power of 0.51 between θ and y/D_h in the developing region when diffusion is negligible with Re/Fr^2 in the range of 0.1 to 10. Here, we observed comparable powers of 0.49 and 0.53 corresponding Re/Fr^2 of 4438 and 2219 respectively, while diffusion of the densifier is significant. The comparable power suggests that the dominant forces decelerating the reorientation may be consistent in our and Yoon's work, despite the great separation of Re/Fr^2. Although densifier diffusion is significant in our study, net diffusion happens for a transient period compared to the residence time of fluids in the channel in the cases of high Re/Fr^2. Thus the drag force is mostly from an invariable source, similar to that in Yoon's work in the absence of diffusion. On the other hand, when Re/Fr^2 is 1109, the time portion with net diffusion is larger, and the drag force is from a variable source during this period. In this case, the slope between θ and y/D_h deviates slightly from the value in Yoon's work.

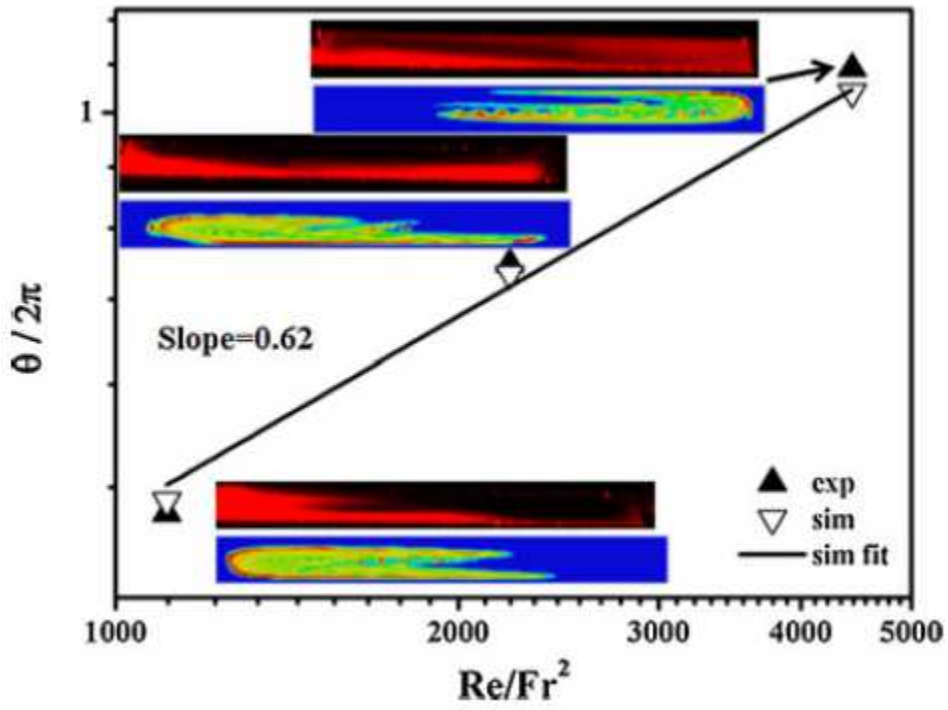

Figure 10 A log-log plot of the angular displacement (θ) as a function of Re/Fr^2 at h/w=0.1, y/D_h=28. The empty symbols denote the predicted results and solid symbols denote experimental measurements. Allometric fitting of the simulation data points is also shown as the solid line

We further compared the angular displacement at the same cross-sectional location of y/D_h = 28 but with different Re/Fr^2 of 1109, 2219, 4438. The results are plotted in Fig. 10 with the solid and empty triangles denoting experimental and simulation results, respectively. A linear dependence of θ on Re/Fr^2 in the log-log scale is observed. An allometric fitting of the simulation results shows a power of 0.62. As Re/Fr^2 is inversely proportional to average velocity in the y direction and θ is measured at the same y coordinate here, the x axis of Fig. 10 scales linearly with the pattern development time. The power of θ vs. Re/Fr^2 being less than 1 suggests that the average rotational velocity decrease at greater Re/Fr^2. Interestingly, this power value matches the value of 0.61 from Yoon *et al.* using two miscible fluids of negligible diffusion and much lower Re/Fr^2. This suggests again that physics behind the interfacial reorientation is comparable in both cases, despite the inclusion of solute diffusion and nanoparticle in our work. As the fluid residence time is long in our channels, the transient solute diffusion does not have a

significant effect on nanofluid rotation except to enable the reorientation beyond $\pi/2$. At the same time, the inertia of nanoparticles is small hence the nanoparticles follow the secondary fluid flow.

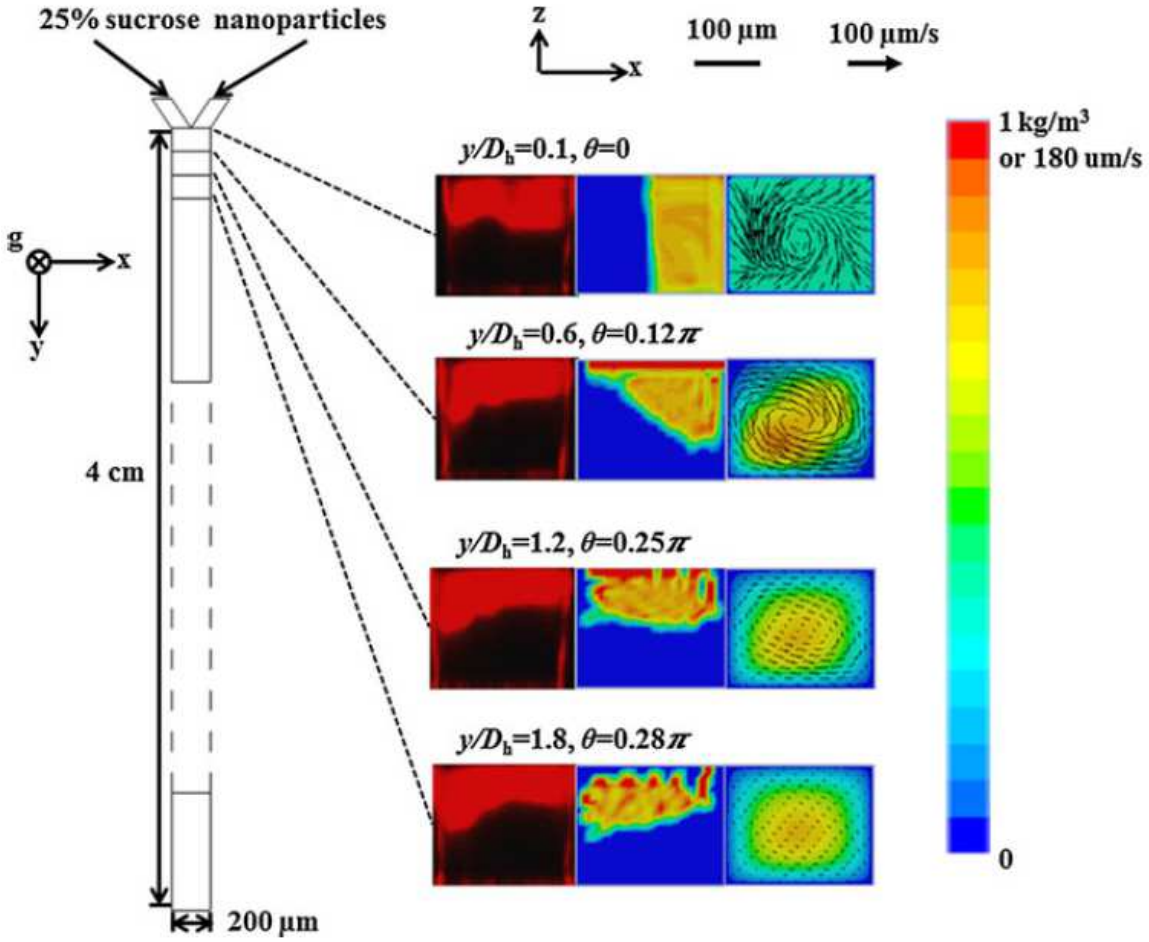

Figure 11 (Left) A schematic showing the top view of the microfluidic device. (Right) The images on the left are from the confocal microscopy; the middle ones are from numerical simulation with the color corresponding to particle concentration from 0 to 1 kg m^{-3} and the images on the right is the in-plane velocity vectors overlapped with the out-of-plane velocity contours for y/D_h=0.1, 0.6, 1.2 and 1.8. Here h/w=0.8 and Re/Fr^2=530

Since the device geometry has been suggested to play an important role in the interfacial reorientation, nanofluid motion in a device with an aspect ratio of 0.8 was investigated next. Similar to the above tests, the nanofluid and the denser sucrose solution were injected side-by-side into the device. At a flow rate of 0.04 µL min^{-1} for each stream and Re/Fr^2 of 530, the confocal images (images on the left of each panel)

and predicted contours of nanoparticle distribution (images in the middle of each panel) are shown in Fig. 11. In comparison, the overlapped in-plane velocity vectors and out-of-plane velocity contours (images on the right of each panel) are also presented. As observed in Fig. 11, nanofluid motion reaches a fully developed state near the inlet, which coincides with the dampening of the in-plane velocity. The discrepancy between experimental and numerical results arises from a back flow as discussed below.

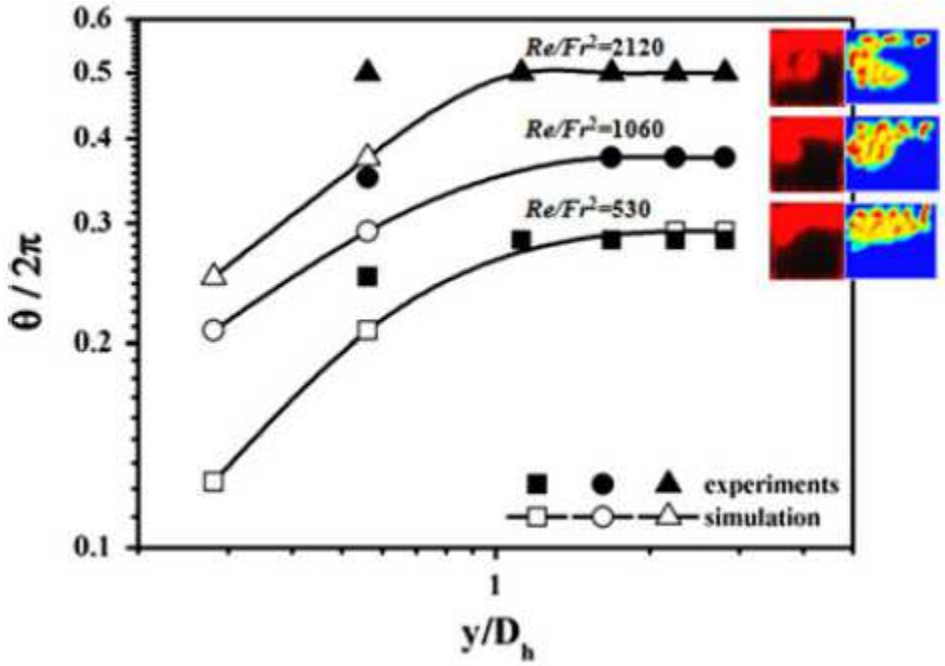

Figure 12 Log-log plots of the angular displacement (θ) as a function of y/D_h for different Re/Fr^2 with fully developed confocal images and predicted contours of nanoparticle distribution for different Re/Fr^2 in the insets. The squares represents results from Re/Fr^2=530, circles from Re/Fr^2=1060, and triangles from Re/Fr^2=2120. The empty symbols are from simulations, and the solid symbols are from experiments. In the fully developed region, experimental results match with simulation results. The angular displacement quickly reaches a fully-developed state. The solid lines trace the simulation results and are used to guide the eye

Fig.12 shows the quantitative relationship between the angular displacement and y/D_h for different values of Re/Fr^2 in the devices with h/w = 0.8. The empty symbols are from simulation and solid symbols are from experiments. The solid lines trace the simulation results and are used to guide the eye. We did not fit θ versus y/D_h in the developing region here due to fast development of the re-orientation. The deviation of experimental data from numerical predictions in the developing region is caused by a backflow near

inlets at extremely low flow rates: it was observed that sucrose penetrated into the nanofluid inlet branch at flow rates lower than 0.1 μL min^{-1}, likely due to slight difference of flow resistance in the two branches. Thus, the reorientation pattern develops faster in the confocal images. Nonetheless, the fully developed angular displacements from experiments and modeling are well matched, and it increases with the decrease of the input flow rate or the increase of Re/Fr^2. This is consistent with the observations in the device of h/w = 0.1 and supports the theory of greater momentum transfer at higher gravitational force relative to the viscous force.

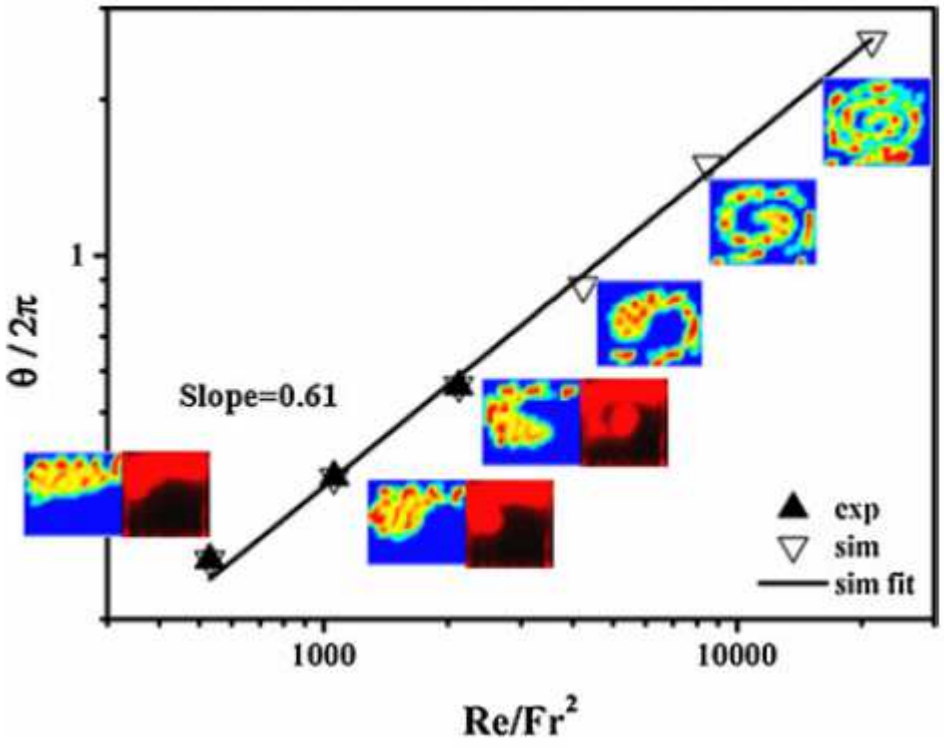

Figure 13 A log-log plot of the angular displacement (θ) as a function of Re/Fr^2 for fixed y/D_h=2.4. The empty symbols are from simulation and solid dots are from experiments. Allometric fitting of the simulation data points is shown as the solid line

When the images are acquired at the same position in the fully developed region but with varying flow rates, the angular displacement scales with $(Re/Fr^2)^{0.61}$ (see Fig. 13). Surprisingly, the power is the same as in the device with an aspect ratio of 0.1, and is

also consistent with previous results in the literature, despite those studies characterized interfacial re-orientation in the developing region.

A drastic difference is observed in the developing length between devices with aspect ratios of 0.1 and 0.8. For device with an aspect ratio of 0.8, secondary flow diminishes near inlets for y/D_h~1, while for device with an aspect ratio of 0.1, secondary flow continues for a long distance even to the outlet of the channel (y/D_h~100). The difference of development length is much greater than that of the Reynolds number, which is 2 times higher in the device with h/w=0.1. This phenomenon can be explained by the initial momentum generated by density stratification. In the two geometries, the channel height is nearly the same but the width is 8 times different. In the low aspect ratio device, movement of more fluid and thus greater momentum result in a much longer development length.

In addition to the dominant swirling motion as observed in the device of h/w=0.1, simulation results from the h/w=0.8 devices also reveal an inwards motion to the center of the x-z plane, forming an Archimedean spiral (inset of Fig. 13). This is likely a result of shear-induced motion [114]. Shear stress distribution in a device with aspect ratio close to 1 tends to push nanoparticles inwards to the center of the cross section. Combination of shear-induced and swirl motion results in an Archimedean spiral.

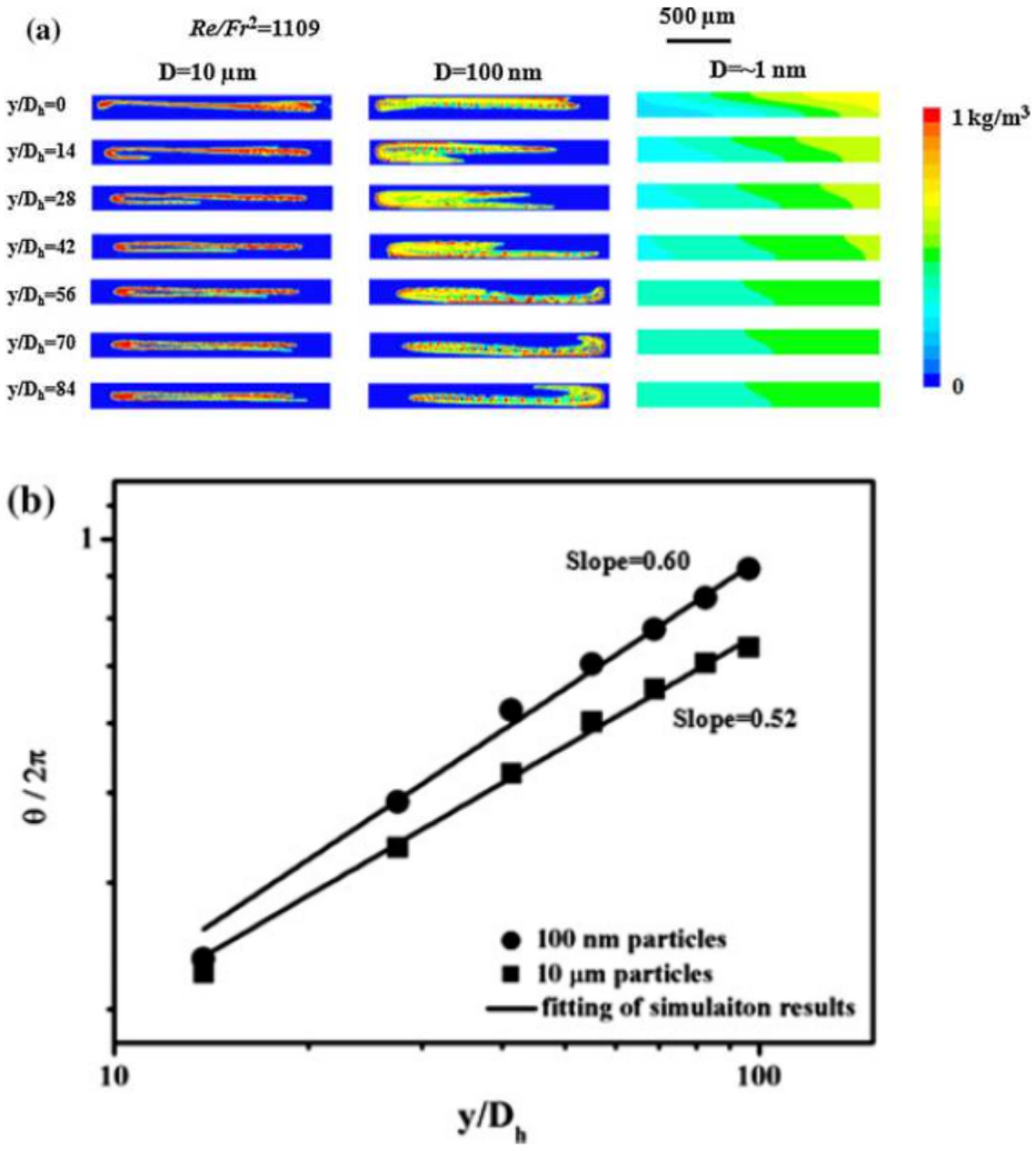

Figure 14 (a) Predicted contours of distributions for 10 μm, 100 nm particles and ~1 nm molecules in otherwise identical stratified flow. In all cases, Re/Fr^2=1109. Slower swirling velocity is observed for microparticles. The microparticles also exhibit an inward motion, which is not observed in the nanofluid swirling with the same channel geometry. (b) The predicted angular displacement (θ) as a function of dimensionless distance from the inlet y/D_h for particles with different diameter at Re/Fr^2=1109. The round symbols are from 100 nm particles and square symbols from 10 μm particles. Allometric fitting of the simulation data points is also shown as solid lines

Besides channel geometry, the observed swirling effect is also sensitive to the particle size. As observed in Fig. 14a, 100 nm nanoparticles mainly swirl, 10 μm microparticles have an inward motion in addition to swirling, and ~1 nm molecules demonstrate fast

diffusion. The different patterns can be explained by size dependent forces. The main forces that the suspended species experience under density stratification are drag, Brownian, and lift force. Using the flow conditions and device geometry tested here, Reynolds numbers for all suspended species are much less than 1, which suggests that the inertial force is negligible relative to the drag force. Thus, all species follow the base fluid swirling through drag force. The effect of drag force can also be observed in the identical secondary flow of the base fluid in the presence of different species (Fig. 8a, b and unshown data). At the same time, diffusion length of micro- and nanoparticle are less than 10 μm within the residence time of 450 seconds and this diffusion length is less than 3% of the device hydrodynamic diameter. Thus, no obvious diffusion is observed for these particles. On the other hand, for molecules of single nanometer dimension, the diffusion length is comparable to the microchannel hydrodynamic diameter within 6 seconds. This contributes to the observed homogenization of molecules near the device inlet. The main force that accounts for the difference between micro- and nanoparticles is the lift force. The lift force remains small for nanoparticles, but becomes significant for microparticles [111]. The lift force drives the microparticles away from the wall to the channel center where velocity of the base fluid swirling is low. Thus, microparticles have slower swirling velocity (Fig. 14b). For even bigger particles like millimeter-scale particles, we conjecture that the lift force may push all the particles even more towards the device center and the swirling velocity would be even slower.

Although it was not experimentally tested, it is worth noting that the diffusion coefficient of the densifier plays an important role to control the nanofluid motion. Too high a diffusion coefficient leads to an immediate homogenization, and the nanofluid does not have enough time to obtain the swirling momentum. On the other hand, too low a diffusion coefficient will lead to reorientation stopping at $\theta = \pi/2$, as further rotation

requires overcoming the gravity. Thus densifier diffusivity needs to be carefully selected to produce desirable nanofluid swirl.

In conclusion, nanofluid swirl patterns induced by density stratification are observed in a steady laminar flow of two miscible fluids in microchannels. The nanofluid migration patterns are investigated in both entrance and fully developed regions in two geometries for various fluid velocities. Stream rotation forms when the device aspect ratio is 0.1, and Archimedean spiral shaped patterns are observed when the device aspect ratio is ~1. The angular displacement varies with dimensionless position from the inlet in the entrance region and the ratio between gravitational and viscous force, Re/Fr^2. Through both experiments and simulation, the swirling motion of nanofluid is shown to follow secondary flow of the base fluid. The interaction of gravitational force, buoyancy force, drag force, Brownian force and diffusion can be utilized to explain the observed swirling patterns. As the particle size varies from nanometer to micrometer the swirling motion and migration pattern of particles alters. The patterns observed and predicted in the present work may have application in nanoparticle focusing, sorting and mixing in microenvironments.

2.2.3 Acknowledgements

We are grateful for the helpful discussions about confocal microscopy with Prof. H. Daniel Ou-Yang, Yi Hu, and Ming-Tzo Wei, about FLUENT with Yan Xu. We also thank Krissada Surawathanawises for Scanning Electron Microscope imaging. Funding for the research is provided by National Institute of Health under Grant No NIAID-1R21AI081638.

3 Thermophoresis induced particles focusing and separation

3.1 Measuring the Soret coefficient of synthetic and biological nanoparticles

3.1.1 Introduction

Compared to other forces that drive particle motion in a fluid, such as dielectrophoresis [18], optical tweezers [19], magnetophoresis [21,22], diffusiophoresis [23], centrifugal force and inertial force [2], the driving force for thermophoresis is less obvious. For example, proteins with the same surface charge could demonstrate opposite migration direction in a temperature gradient [26]. It has been postulated that various interfacial properties as well as the particle size could influence the Soret coefficient, but the exact mechanism is still under investigation. Nonetheless, the sensitivity of thermophoresis to the interfacial forces offers exclusive insights about thermodynamics on the molecular level. Thermophoresis is also capable of overcoming Brownian force and drive the motion of unlabeled, solvated nanoparticles and molecules on the macroscopic scale. It has found applications in various fields such as isotope concentration and gas phase separation [24,25], and has attracted a lot of research interest for the understanding of origin of life [86,88,94], protein interactions [91] and colloid interfacial energies [93]. These characteristics have led to various applications of thermophoresis in the biomedical field. Thermophoresis of many biological species in electrolyte solutions have been characterized, including DNA [73], protein [91], lipids [88], liposome [115], detergent [27,116], and virus [117,118]. Multiple reviews on the theories and implementation of thermophoresis can be found in the literature [74,119,120,121]. Two parameters are commonly used to characterize thermophoresis: the thermal diffusion coefficient, D_T, which is the ratio of the thermophoretic velocity to the temperature gradient and the Soret coefficient, S_T, which is the ratio of the thermal diffusion coefficient to the

normal diffusion coefficient.

There have been several proposed theories to predict the Soret coefficient [66–73]. Because these theories are based on thermodynamic analysis of ion distribution and hydration layer structure in a temperature gradient, it is still difficult to derive the theoretical S_T due to the lack of thermodynamic parameters. Instead, S_T is mostly obtained experimentally. When the motion of the target species can be directly tracked by an optical microscope, the thermophoretic velocity and S_T is usually measured from the particle velocity. On the other hand, the measurement of S_T relies on the concentration profile. At the steady state, a balance between thermodiffusion and ordinary diffusion leads to a predictable concentration gradient in response to a temperature gradient. Assuming the diffusion and thermodiffusion coefficients are both constants and the temperature gradient is linear, the steady state concentration for two dimensional thermophoresis can be approximated by the exponential depletion law:

$$\frac{c}{c_0} = exp[-S_T(T - T_0)] \quad (1)$$

where the normalized concentration c/c_0 depends on the temperature difference $T - T_0$. Here c_0 is the bulk concentration of the reservoir and T_0 is the ambient temperature. To extract S_T from a three dimensional concentration profile or from solute distribution in the transient state, a continuous phase model has been constructed that couples flux from convection, diffusion and thermodiffusion [24,25,73]. These data-fitting methods require the target species to be in a continuum phase to measure the concentration distribution.

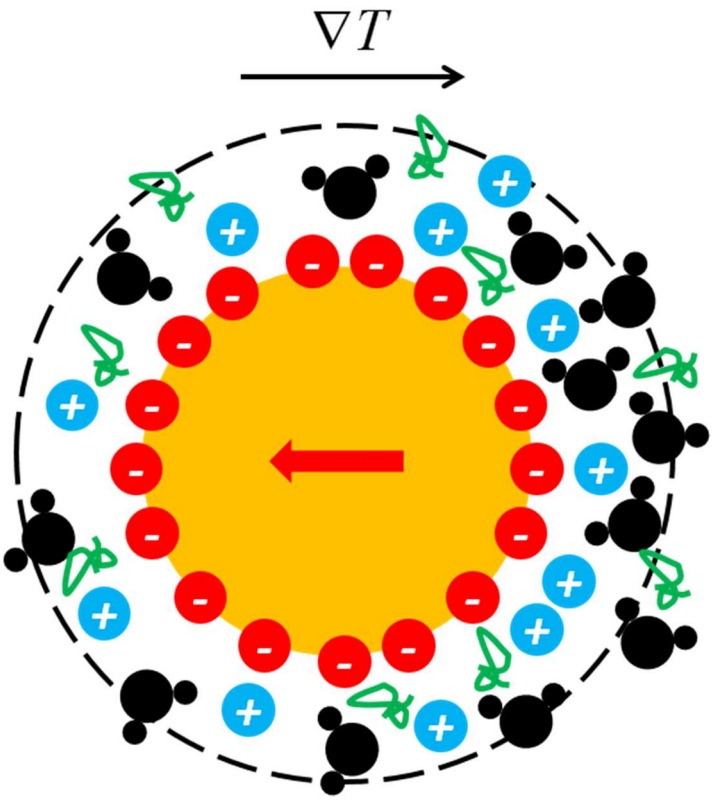

Figure 15 Schematic of a nanoparticle interacting with solute

Synthetic particles, micelle and limited number of biological molecules, like DNA and protein have been studied. However, information about biological vesicles are scarce and critical. As thermophoresis is a surface effect (Fig. 15), interaction at the surface of biological vesicles is determined to be different from that of polystyrene beads. Also, as thermophoresis is depending on the physiological buffer and plasma proteins, a systematic study of thermophoresis under different buffer conditions is needed. Here, we measured the Soret coefficient of synthetic nanoparticles in different buffers, and that of the HIV virus for the first time.

Another application of measuring the Soret coefficient in biomedicine is to quantify biomolecule binding in complex fluids. Understanding the kinetics and mechanisms of biomolecule interactions is important for different fields of life science, from molecular physiology and pathology to diagnostics and pharmacology [120,121]. As the Soret coefficient

is highly sensitive to binding-induced changes such as particle size, charge, and hydration layer, it has recently been used for quantitative analysis of biomolecule interactions in the solution phase. The groundbreaking demonstration, termed microscale thermophoresis, was reported in 2010, where interactions of proteins and small molecules in blood serum and cell lysate were measured [91]. The setup uses an infrared laser focused in a thin microfluidic chamber to create a circular temperature gradient. Natural convection is negligible in the thin gap and the temperature gradient drives biomolecules away from the laser focal point [77,92], generating a 2-D depletion zone (Fig. 25a-b) visible with fluorescent molecules. Compared to conventional methods such as electrophoretic mobility shift assays (EMSA) [122,123], enzyme linked immunosorbent assays (ELISA) [124], isothermal titration calorimetry (ITC) [125–127], dynamics light scattering (DLS) [128,129], fluorescence polarization (FP) [130,131], and surface plasmon resonance (SPR) [132–135], using Soret coefficient to infer molecular interaction requires little sample preparation or purification. The sample volume is extremely low down to 10 nL [136] and concentration down to sub-nM is measurable in the solution [120]. The optical setup is relatively simple and can be adapted from a simple fluorescence microscope.

Since the Soret coefficient of the receptor-ligand complex is higher than those of the unbound molecules, the complex responds stronger to the temperature gradient than free molecules, leading to greater concentration depletion (Fig. 25c). The steady-state depletion at the laser focal point in a titration series is used to generate the binding isotherm (Fig. 25d). By fitting the isotherm to Hill's equation, the dissociation constant K_d is derived for receptor-ligand pairs. In the first report by Wienken *et al.*, the interactions of three receptor-ligand pairs, human interferon gamma and its antibody, calmodulin and calcium as well as kinase PKA and its small-molecule inhibitor quercetin were studied and the$K_d$values were in good agreement with those measured by other approaches in the literature [91]. Since then, microscale thermophoresis has been applied to compare the

affinity of receptors with ligands, including the binding of tubulin to two intraflagellar transport proteins [137], interaction of H5N1 influenza virus with human and avian receptors [138], activity inhibition of the G-protein-regulated Rho guanine nucleotide exchange factor [139] and histone deacetylases Sirtuin by their inhibitors [140] and the modulation of positive transcription elongation factor by two repressors [141]. Many of these interactions were characterized for the first time since the sample concentration and volume could not afford analysis by conventional approaches.

The measurement of K_d can be further used to study the dependence of molecular binding on the solution composition. For example, through thermophoretic measurements, the dissociation constant between an aptamer and thrombin was found to increase by 8 folds when the solution changes from a Tris buffer to a sodium citrate buffer [142]. In addition, thermophoresis can be utilized to study complex binding modes, such as competitive binding of two ligands to the same binding site [143,144].

Besides receptor-ligand binding, microscale thermophoresis has also been utilized to detect polymer phase transition and protein conformational change in aqueous solutions [145]. For example, M. Wolff *et al.* used this method to measure the lower critical solution temperature (LCST) of oligo(ethylene glycol). The LCST behavior involves the coil-to-globule transition of individual polymer chain and interchain aggregation that increases the solution turbidity. However, it is challenging to measure the turbidity change in a small sample volume at low concentrations in the nanomolar range. Instead, M. Wolff *et al.* determined S_T of polymer molecules at different ambient temperatures (Fig. 25e). As the hydration layer around the polymers changes dramatically at the transition temperature, the crossover point on the S_T vs temperature curve with a slope changing from negative to positive was interpreted as the phase transition temperature. Similarly, native and denatured proteins have different S_T, which have been used to study the folding of the core protein of human hepatitis B virus in guanidinium chloride and urea [146].

Despite the utility of thermophoresis for biomolecule enrichment and bio-interaction measurements, the mechanism of thermophoresis in an aqueous phase is still under active research. Molecular dynamics analysis is needed to predict the origin of thermophoresis and carefully designed experiments with only one varying parameter at a time are needed to verify the theoretical prediction. The mechanistic understanding can provide insights on how biomolecules and bioparticles interact with the solvent molecules and each other as well as thermodynamics at the interface. Coupled with detailed structure map of biomolecules, one may use S_T to infer binding sites of ligand on the receptor and chemical bonds involved in the interaction. Beyond the demonstrated measurements of reaction isotherm at the equilibrium state, microscale thermophoresis may be used to study the reaction kinetics as long as the thermophoretic response rate is faster than the reaction rate. From the technical point of view, microscale thermophoresis requires the analyte to be treated as a continuum, while a dilute nanoparticle suspension, such as a viral sample, may not meet the requirement. Experimental breakthroughs are yet needed to characterize the thermophoretic behavior of such suspensions with discrete species. The extraordinary enrichment power of the thermodiffusion column can promote novel biosensor development, while strategies to scale up the thermodiffusion column and maintain the concentration power may be necessary to make thermophoretic enrichment practical for biological sample processing.

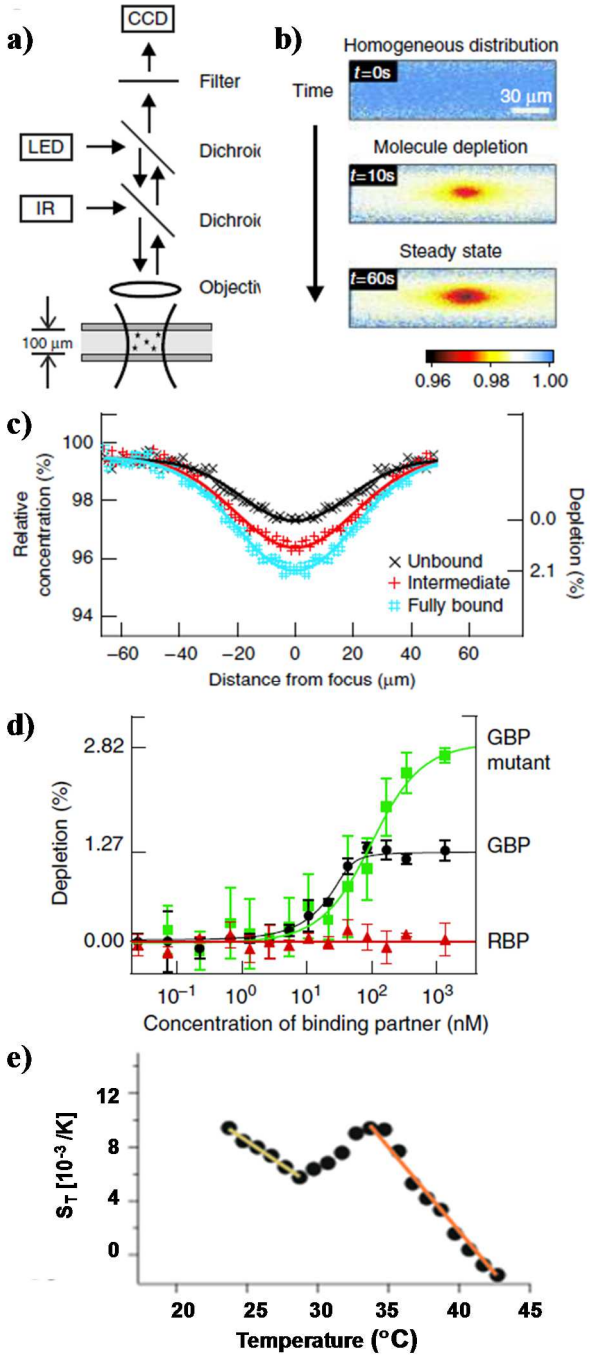

Figure 16 Microscale thermophoresis for quantifying biomolecular interactions (Figures from [91] and [145]). a) Thermophoresis response was measured with an IR laser locally heating a sample in a shallow microchamber. The re-distribution of a fluorescent species in response to the temperature gradient is imaged by a microscope. b) Initially, the fluorescence is uniformly distributed. After switching on the IR laser, depletion of molecules is observed. c) The steady state depletion profile of human interferon-γ was measured in the presence of its antibody at different concentrations. The depletion reflects the fraction of bound complex. d) To determine the reaction constant of an interaction pair, one binding partner was titrated while the other is kept constant. Here the interaction of the intrinsic fluorescent protein GFP with various binder proteins was measured [91]. e) For a themoresponsive polymer, the Soret coefficient was measured over a range of ambient temperature and the transition temperature is interpreted as the transition point on the curve [145].

3.1.2 Results and conclusion

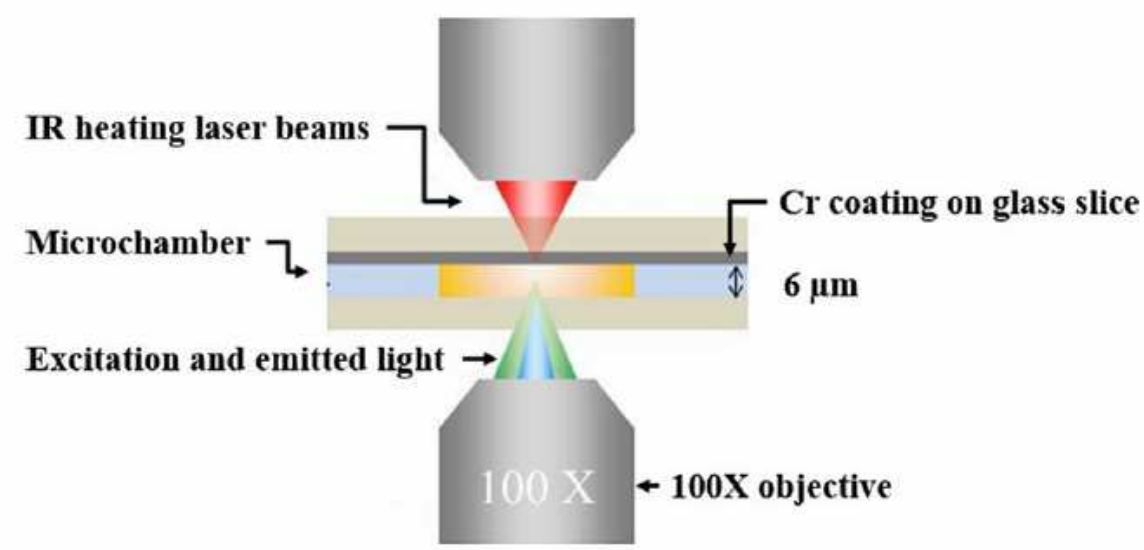

Figure 17 A schematic of the optical setup combined with a microfluidic chamber used in this study. The laser was focused on the ceiling with a thin chromium layer to absorb the IR energy. Distribution of 100 nm fluorescent Polystyrene beads was observed by a confocal fluorescence microscope.

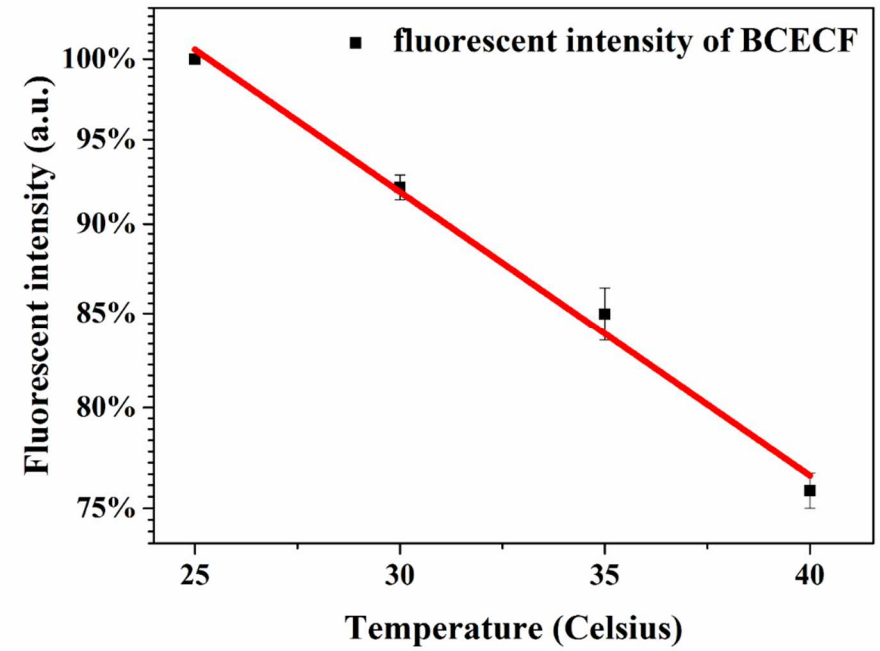

Figure 18 Dependence of fluorescent intensity of BCECF as a function of temperature. The microscope stage was heated uniformly and the temperature in the detection chamber was measured using a thermocouple. The intensity decreases in response to increasing temperature with a slope of -1.6% K^{-1}.

The optical set up used in this work was modified based on the literature [77]. Briefly, polystyrene nanoparticles were diluted in DI water and 3 μL of the nanoparticle suspension was pipetted on a glass slide. A chromium coated coverslip was placed on the suspension to form a 6 μm thick thin film. The edge of the coverslip was sealed by mineral oil to prevent evaporation [76]. To create a temperature gradient, an infrared laser (1 mW) was focused on the chromium layer (Fig. 17). The IR laser was a Gaussian beam with a radius around 1 μm. The temperature gradient in the liquid was calibrated independently using a temperature sensitive dye BCECF at a concentration of 1 mM [147]. The fluorescence intensity of BCECF decreases linearly with temperature (Fig. 18). The particle distribution was imaged using confocal microscopy on the center plane between the two solid substrates.

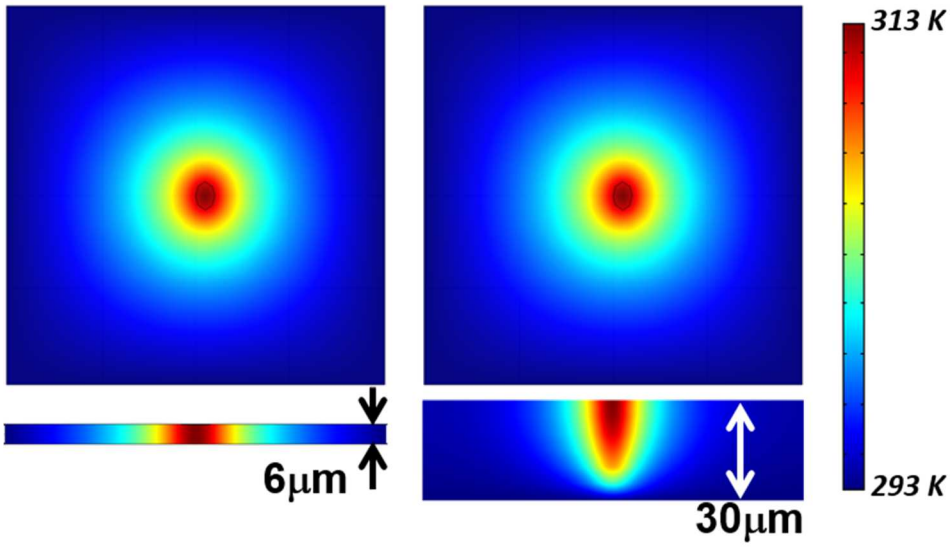

Figure 19 Temperature profile under different chamber heights.

Numerical analysis was performed by the continuous phase models. The power density of the IR laser was modeled as a three dimensional Gaussian distribution and the laser was considered as an energy source:

$$Q = Q_0(1 - R_c)A_c\left(\frac{1}{\pi r_x r_y}\right)\exp\left(-\frac{(x - x_0)^2}{2r_x^2} - \frac{(y - y_0)^2}{2r_y^2}\right)\exp\left(-A_c abs(z)\right)$$

where Q is the power density in the fluid, Q_0 is the total laser power, A_c is absorption coefficient, R_c is reflection coefficient, r_x and r_y are the standard deviation of laser pulse in the x and the y directions, respectively. x_0 and y_0 are the center coordinates of the laser beam, and x, y and z are the spatial coordinates. $abs(z)$ is the absolute value of z. Since the liquid film is thin, the laser heating established a two dimensional temperature gradient in the liquid between the focal point and the ambient. Fig. 19 shows the 2D and 3D Temperature profiles when chamber height is 6 μm or 30 μm. The experiment and simulation match well with each other (Fig. 20).

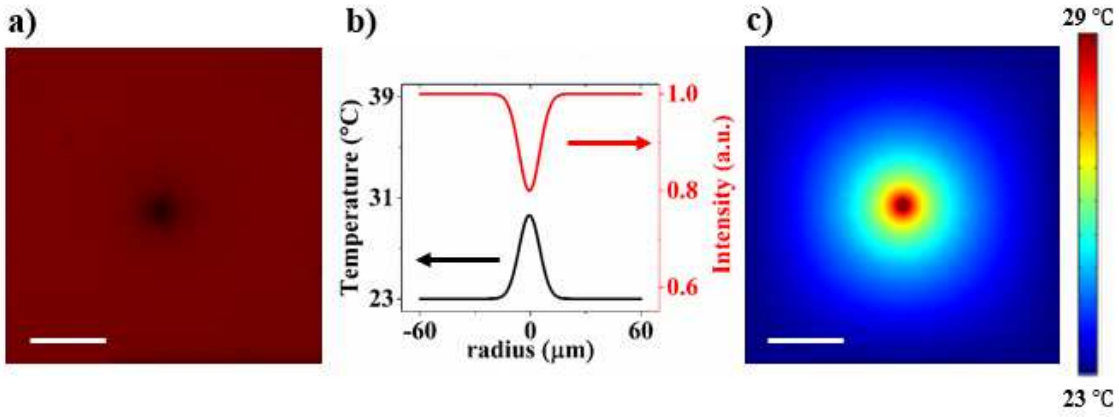

Figure 20 Measurement of the temperature profile in the detection chamber from laser heating. a) Fluorescent intensity measurement by BCECF. b) Radially averaged fluorescence intensity is converted to the temperature profile, which indicates a linear temperature gradient of 0.5 K μm^{-1} spanning radially from the focused laser for ~20 μm (c) The simulated temperature gradient matches the experimental observation. This temperature gradient is used in both the continuous and discrete phase models.

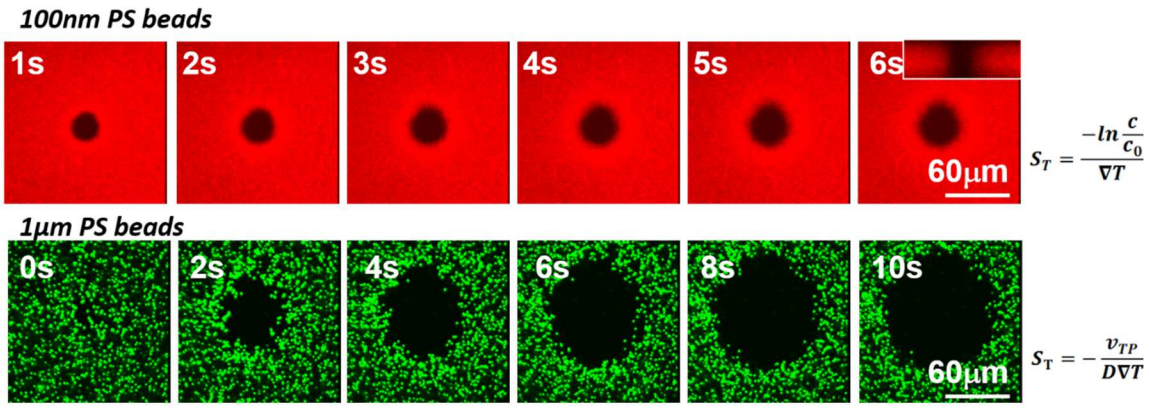

Figure 21 Dynamics of migration of 100 nm PS beads and 1 μm PS beads under a temperature gradient.

For measurement of the Soret coefficient, a 2D temperature gradient is needed, so a chamber with height at 6 μm is adopted. After successfully establish a radial temperature gradient, 100 nm PS beads and 1 μm PS beads were exposed to it. Because of the depletion of beads in high temperature, Fig. 21 shows the dynamics of thermophoresis, and it takes less than 10 seconds to reach steady state in current setup. For 100 nm PS beads, the temperature profile was fit with the depletion function to derive the Soret coefficient. Contrarily, for 1 μm PS beads, the velocity of individual beads was tracked and used to calculate the Soret coefficient by its definition.

For the continuous phase model, the governing equations to describe natural convection are the Navier-Stokes equation with Boussinesq approximation and the mass conservation equation:

$$\frac{\partial \boldsymbol{u}}{\partial t} + \boldsymbol{u} \cdot \boldsymbol{\nabla} \boldsymbol{u} = -\frac{1}{\rho} \boldsymbol{\nabla} p + \gamma \boldsymbol{\nabla}^2 \boldsymbol{u} + \alpha \boldsymbol{g}(T - T_0)$$

$$\boldsymbol{\nabla} \cdot (\rho \boldsymbol{u}) = 0$$

where ρ is the fluid density, γ is the kinematic viscosity, t is the time, $\boldsymbol{u}$ is the fluid velocity, p is the pressure, α is the thermal expansion coefficient of the fluid, $\boldsymbol{g}$ is the gravitational acceleration, and T is the temperature.

The conservation of energy is in the form:

$$\rho C_p \frac{\partial T}{\partial t} + \rho C_p \boldsymbol{u} \cdot \boldsymbol{\nabla} T = \boldsymbol{\nabla} \cdot (k \boldsymbol{\nabla} T)$$

where C_p is the heat capacity of the fluid, and k is the thermal conductivity of the fluid.

The mass transport equation includes the mass diffusion, advection and the effect of the thermophoresis:

$$\frac{\partial c}{\partial t} = \boldsymbol{\nabla} \cdot (D_T c \boldsymbol{\nabla} T + D \boldsymbol{\nabla} c) - \boldsymbol{\nabla} \cdot (\boldsymbol{u} c)$$

where c is the concentration of the species.

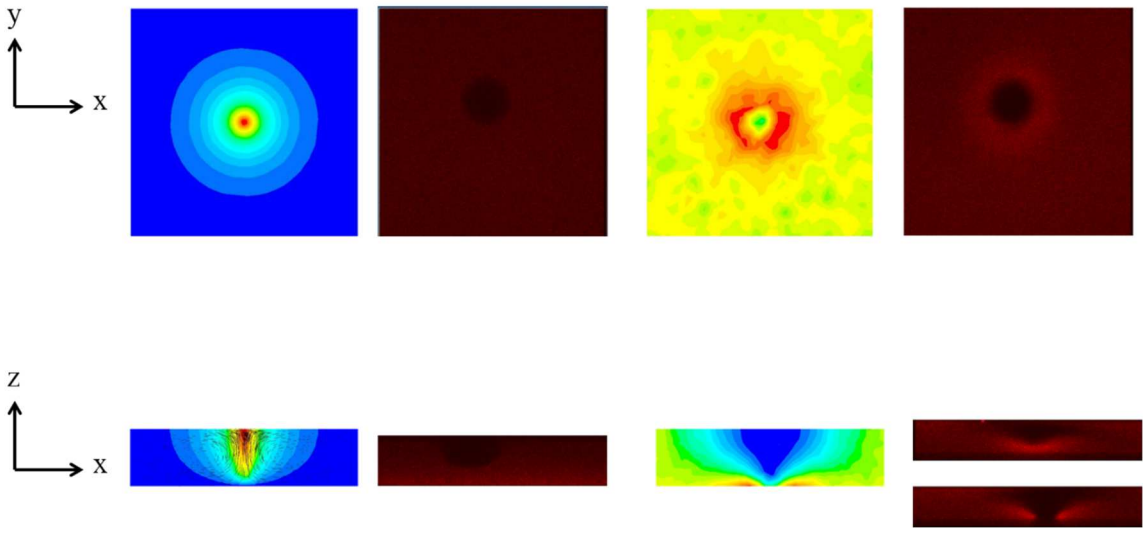

Figure 22 2D and 3D temperature gradient and particle pattern.

For chamber higher than 30 μm, natural convection induced by the radial temperature gradient prevents the chamber from being applied to derive the Soret coefficient.

However, coupling these two together induces interesting trapping phenomenon [84]. In our simulation and experiments, the focusing effect could be repeated (Fig. 22). On the left of Fig. 22, it shows the fluorescent intensity of BCECF, which is proportional to temperature, and it shows the 3D temperature gradient when the chamber height is 30 μm. On the right half of Fig. 22, it shows the nanoparticles fluorescent intensity. The top and cross sectional view of the nanoparticle fluorescence shows the focusing ring structure on the bottom of the chamber, and the cross sectional view shows the nanoparticle redistribution caused by thermophoresis and natural convection.

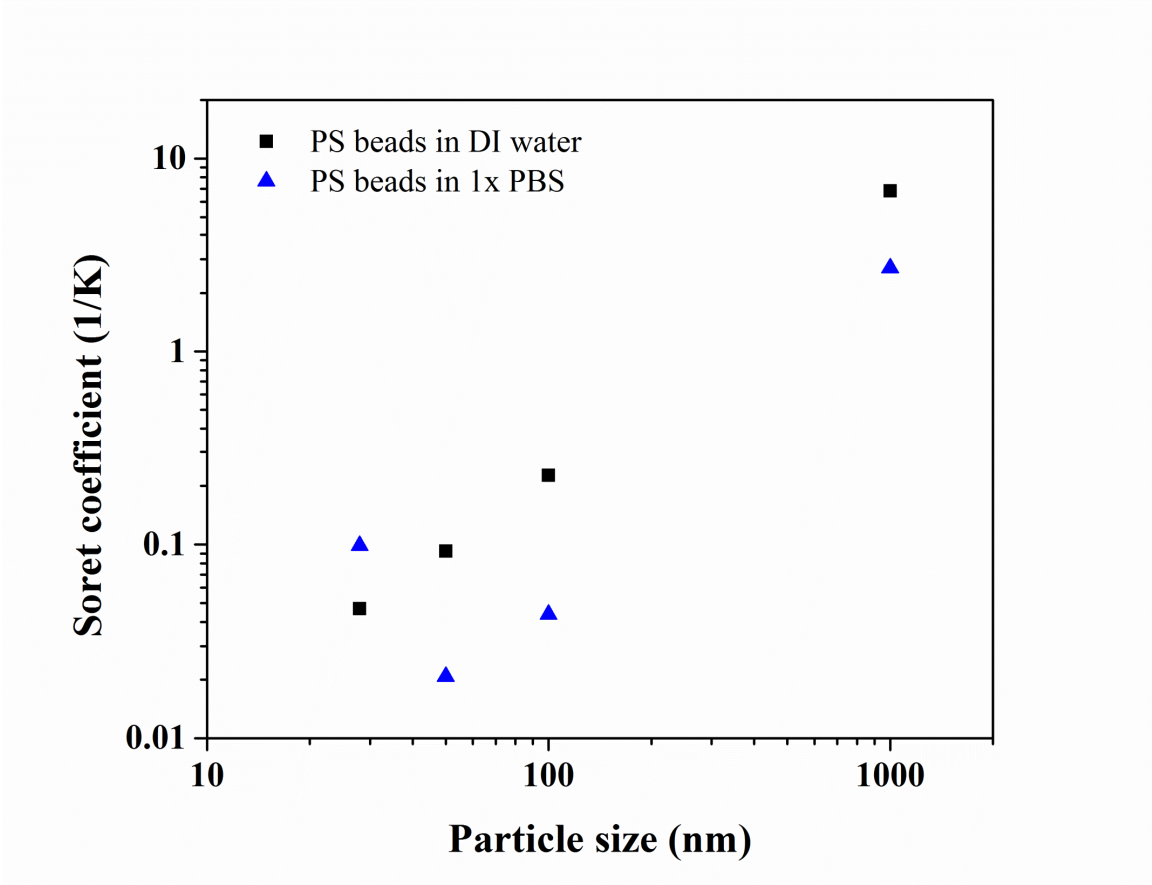

Figure 23 The Soret coefficient of different sized particles in DI water and PBS buffer.

In order to systematically study the Soret coefficient's relationship with the synthetic particle size, experiments of PS beads with diameters at 25 nm, 50 nm, 100 nm and 1

μm are performed. Fig. 23 shows that the Soret coefficient of particles in DI water increase monotonically with the increasing size, which matches the literature [73]. It is also predicted that the Debye length influences the Soret coefficient as the Debye length is the particle-solute interaction range. All particles' Soret coefficient in PBS confirmed this hypothesis. Except the abnormal 25 nm nanoparticles, the Soret coefficient decrease for about 3 times in PBS compared with in DI water. The abnormality is because when the particle size are comparable to the Debye length, the double layer model is not applicable.

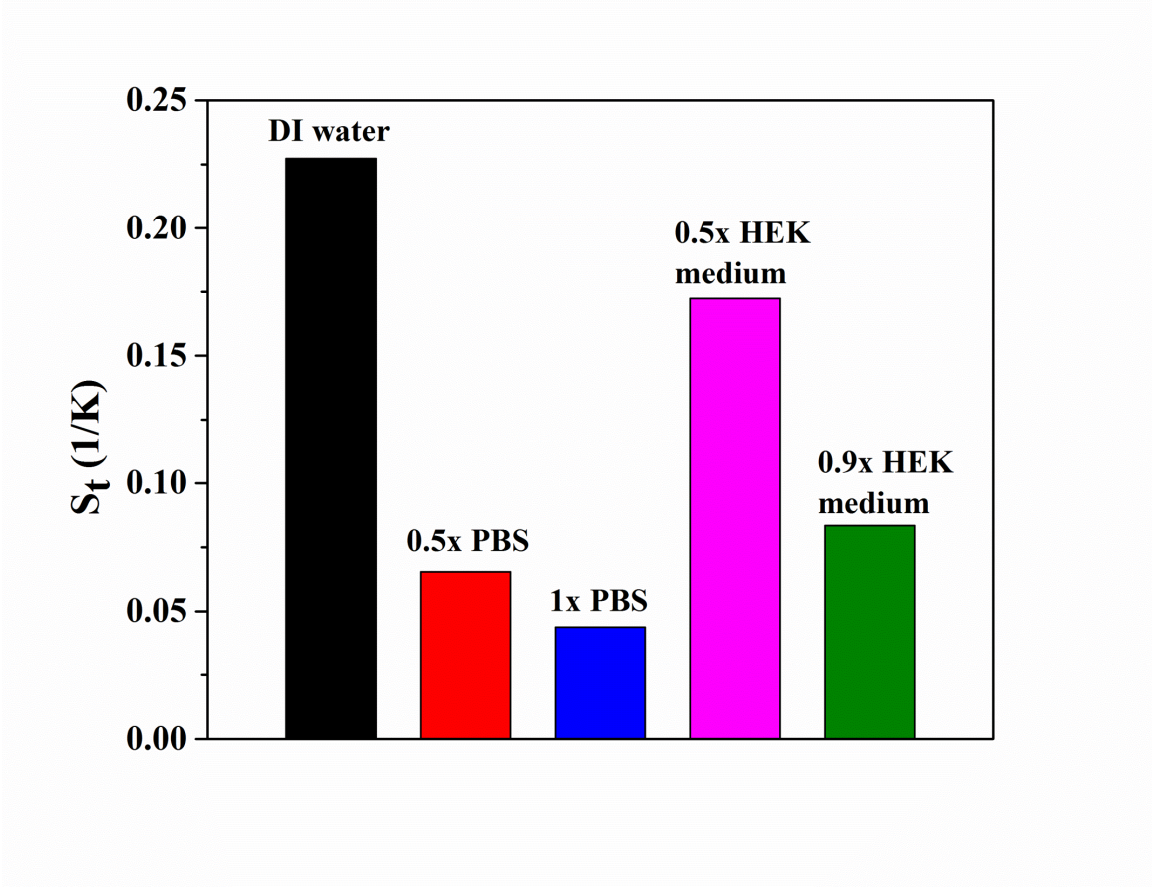

Figure 24 Soret coefficient of HIV virus in different buffer.

We also measured the Soret coefficient of 100 nm nanoparticles in different buffers, like DI water, 0.5x PBS, 1x PBS, 0.5x HEK medium, and 0.9x HEK medium (Fig. 24). HEK

medium is chosen as it is the buffer for HIV virus in our lab. For the first three columns in Fig. 24, the Soret coefficient decrease with the increase of salt concentration. However, the last two columns show that the biological species in HEK medium interacts with PS beads besides the ions and water molecules, inducing a higher Soret coefficient compared with PBS, but still a smaller coefficient compared with DI water, as the Debye length effect in the solute is dominating over other surface interacting forces.

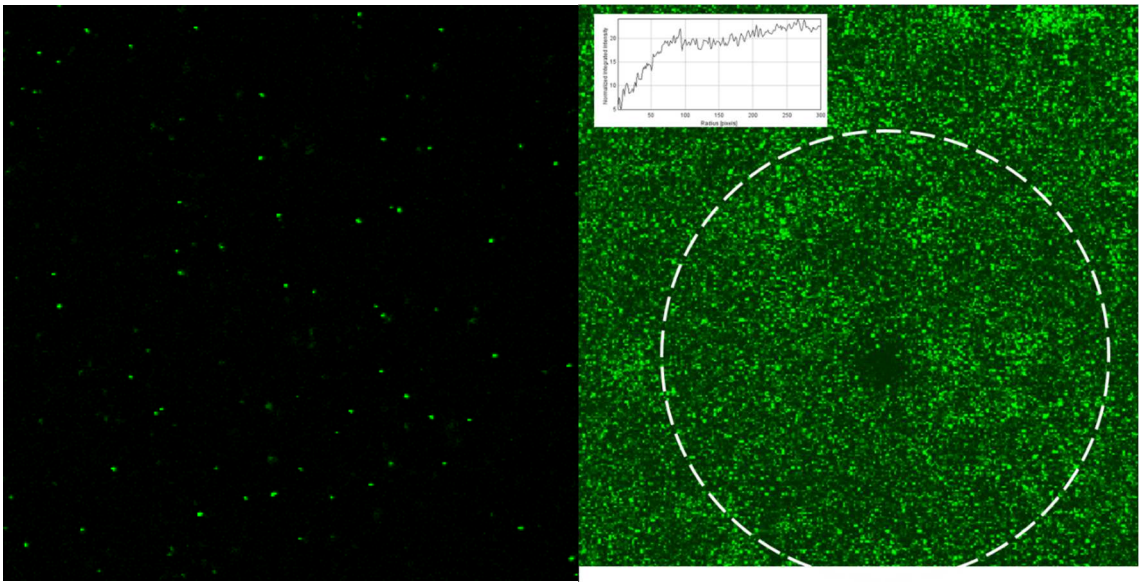

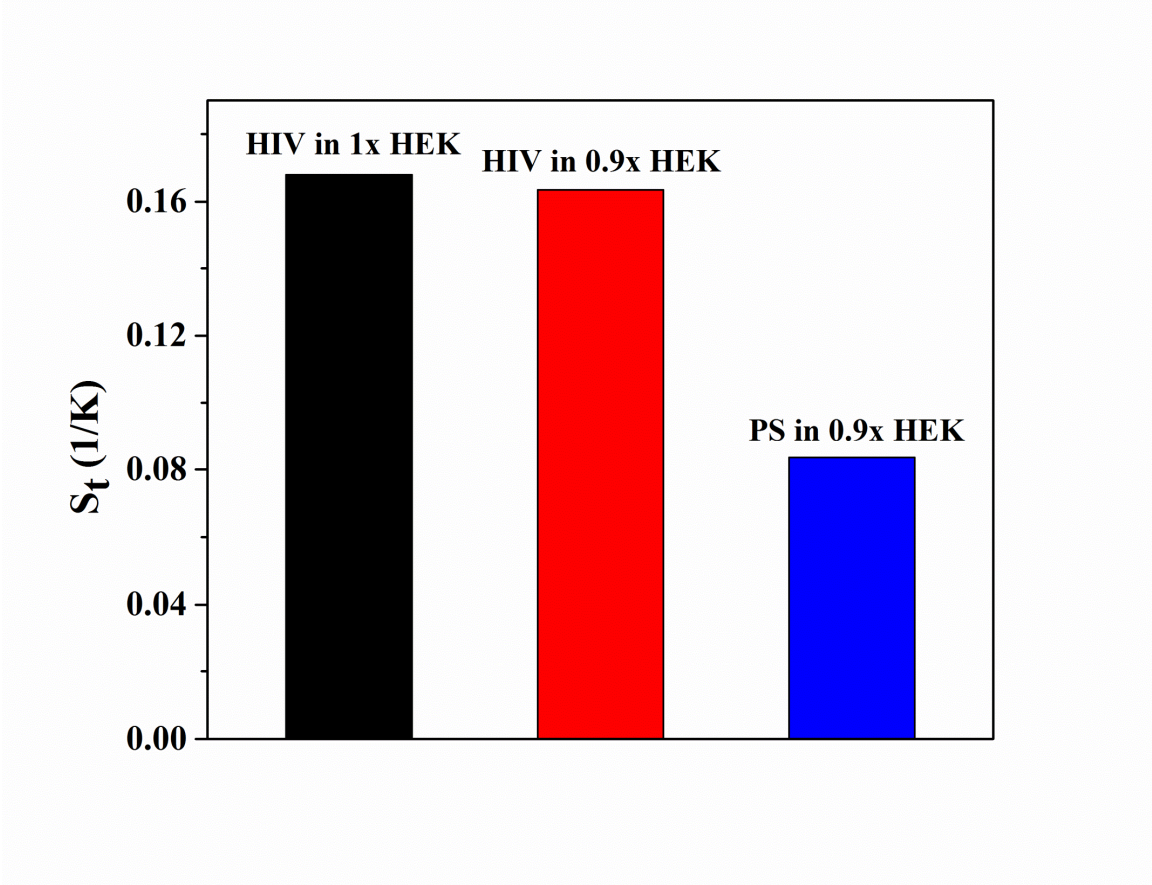

Figure 25 a) The HIV virus fluorescent image b) measurement of the Soret coefficient of HIV virus by stacking thousands of images together c) comparison between HIV virus and PS beads.

As our setup succeeded in measuring the Soret coefficient of synthetic nanoparticles with different size and in various buffer, thermophoresis of HIV virus is studied. Fig. 25a shows the fluorescent image of HIV virus. As the concentration is typically low and there are lots of space between the HIV viruses, the concentration profile could not be fitted with an exponential function; also as the Brownian motion is too fast, the tracking of each single virus is impractical using current setup. In order to solve this dilemma, thousands of fluorescent images of HIV virus under a temperature gradient is overlaid to form a continuous concentration contour (Fig. 25b). Then the profile was fitted with the depletion law to derive the Soret coefficient. As the size of HIV virus is about 120 nm, the measured Soret coefficient is 0.17 1/K. It is very close to the Soret coefficient of 0.18 1/K for 100 nm nanoparticles in DI water, despite the ions in the HEK medium. This is because of the larger size and more interactions from biological species in the HEK medium (Fig. 25c).

In conclusion, the Soret coefficients of different sized synthetic particles in various buffer condition were measured in an all optical setup. Also, the Soret coefficient of HIV virus was tested for the first time. The plasma protein in the biological buffer increase the Soret coefficient, while the electrolyte decreases it. Also thermophoresis has been demonstrated as a powerful tool to study their interaction affinity in aqueous solutions. With ongoing efforts to reveal the driving forces of thermophoresis, it may provide even more information about receptor-ligand binding and the associated thermodynamic processes.

3.1.3 Acknowledgements

We are grateful for the helpful discussions with Dr. Jinxin Fu. The HIV viral stock was kindly prepared by Caroline Multari. We are grateful for the helpful discussions with Prof.

Daniel Ouyang. Funding for the research was provided by National Institute of Health under Grant No. NIAID-1R21AI081638.

3.2 Discrete model for Soret coefficient measurement in a dilute suspension

3.2.1 Introduction

Conventionally, the Soret coefficient of nanosized species is obtained by fitting the concentration profile under a temperature gradient at the steady state to a continuous phase model. However, when the number density of the target is ultralow and the dispersed species cannot be treated as a continuous phase, the bulk concentration fluctuates spatially, preventing extraction of temperature-gradient induced concentration profile. The present work demonstrates a strategy to tackle this problem by superimposing snapshots of nanoparticle distribution. The resulting image is suitable for the extraction of the Soret coefficient through the conventional data fitting method. The strategy is first tested through a discrete phase model that illustrates the spatial fluctuation of the nanoparticle concentration in a dilute suspension in response to the temperature gradient. By superimposing snapshots of the stochastic distribution, a thermophoretic depletion profile with low standard error is constructed, indicative of the Soret coefficient. Next, confocal analysis of nanoparticle distribution in response to a temperature gradient is performed using polystyrene nanobeads down to 1e-5% (*v/v*). The experimental results also reveal that superimposing enhances the accuracy of extracted Soret coefficient. The critical particle number density in the superimposed image for predicting the Soret coefficient is hypothesized to depend on the spatial resolution of the image. This study also demonstrates that the discrete phase model is an effective tool to study particle migration under thermophoresis in the liquid phase.

However, when the concentration of the dispersed phase is low, the spatial distribution appears discrete and it is difficult to directly apply the depletion law or continuous phase model to obtain S_T. To overcome this challenge, we demonstrate here that by superimposing snapshots of the nanoparticle distributions, a thermophoretic depletion profile with low standard error can be obtained for the extraction of S_T. A discrete phase model is constructed first to illustrate the stochastic nature of nanoparticle distribution in a dilute suspension and the power of overlapping to significantly reduce the spatial fluctuation of concentration. The modeling results are confirmed using polystyrene nanoparticle suspensions at a concentration down to 1e-5% (*v/v*), i.e. on the order of 32 pM. Through the combined experimental and computational analysis, we also discuss the critical particle number density to obtain S_T accurately.

3.2.2 Results and conclusion

The discrete phase model employed the particle tracking theory with Eulerian-Lagrangian approach. The solvent (continuous phase) was treated using Eulerian description and the dispersed particles (discrete phase) were tracked using the Lagrangian description. Two-way coupling was employed in our modeling, where the continuous phase could affect the behavior of discrete phase, and vice versa. Hence, in this process a proper designed solver calculated the continuous and discrete phase equations in an alternate manner until a converged coupled solution was achieved. Particles were treated as volumeless points, but the size effect was incorporated in the Brownian, the drag, the lift and the buoyancy forces exerted on the particles. Given the low particle concentration and much larger detection volume compared to the particle size, particle-particle and particle-wall interactions are negligible. Thus, it is reasonable to ignore the particle volume for particle tracking.

By employing Eulerian approach, the steady creeping fluid flow was modeled by Navier-Stokes equation including the source term. The equations governing the conservation of mass and momentum of the liquid phase are [109,110]

$$\boldsymbol{\nabla} \cdot (\rho \boldsymbol{u}) = 0$$

$$\boldsymbol{\nabla} \cdot (\rho \boldsymbol{u}\boldsymbol{u}) = -\boldsymbol{\nabla} p + \boldsymbol{\nabla} \cdot (\bar{\bar{\tau}}) + \rho \boldsymbol{g} + \frac{1}{V_{ijk}} \sum_{p} \left(F_D \left(\boldsymbol{u_p} - \boldsymbol{u} \right) \right) \dot{m}_p \Delta t$$

$$Re_r = \frac{\rho d_p \left| \boldsymbol{u_p} - \boldsymbol{u} \right|}{\mu} and \quad F_D = \frac{18\mu}{\rho_P d_p^2} \frac{C_D Re_r}{24}$$

where ρ is the fluid density, μ is the viscosity of the fluid, $\boldsymbol{u}$ is the fluid phase velocity, p is the static pressure, $\bar{\bar{\tau}}$ is the stress tensor, $\rho \boldsymbol{g}$ is the gravitational body force, $\boldsymbol{u_p}$ is the particle velocity, ρ_P is the density of the particle, d_p is the particle diameter, C_D is the drag coefficient, $\dot{m}_p$ is the mass flow rate of the particles, Δt is the time step, $F_D \left(\boldsymbol{u_p} - \boldsymbol{u} \right)$ is the drag force per unit particle mass and Re_r is the relative Reynolds number. The last term in the second equation is the momentum source term that represents the influence of the particles on the flow field of fluids. It is calculated by averaging momentum of all the particles in the volume of fluid element (V_{ijk}).

Lagrangian approach was employed for the discrete phase model to track the movement of particles [71,148–150]:

$$\frac{d\boldsymbol{u_p}}{dt} = F_D \left(\boldsymbol{u} - \boldsymbol{u_p} \right) + \frac{\boldsymbol{g} \left(\rho_p - \rho \right)}{\rho_p} + \boldsymbol{F_b} + \boldsymbol{F_l} + \boldsymbol{F_{tp}}$$

$$\boldsymbol{F_b} = \boldsymbol{\zeta}\sqrt{\frac{\pi S_0}{\Delta t}}\ and\ S_0 = \frac{216\mu k_B T}{\pi^2 \rho^2 d_p^5 \left(\frac{\rho_P}{\rho}\right)^2 C_c}$$

$$\boldsymbol{F_l} = \frac{2K(\mu/\rho)^{1/2}\rho}{\rho_p d_p \left(\bar{\bar{d}} : \bar{\bar{d}}\right)^{1/4}} \bar{\bar{d}} \cdot \left(\boldsymbol{u} - \boldsymbol{u_p}\right)$$

$$\boldsymbol{F_{tp}} = 6\pi\mu d_p \boldsymbol{u} = -6\pi\mu d_p D_T \boldsymbol{\nabla} T$$

where $\boldsymbol{F_b}$ is the Brownian force per unit particle mass [111], $\boldsymbol{F_l}$ is the Saffman's lift force per unit particle mass due to shear [112], the thermophoretic force per unit particle mass in liquid $\boldsymbol{F_{tp}}$ is modeled using the empirical Stokes law [148], K=2.594, $\boldsymbol{\zeta}$ are zero-mean, unit-variance-independent Gaussian random number composed vector, T is the absolute temperature of the fluid, k_B is the Boltzmann constant, C_c is the Stokes-Cunningham slip correction, and $\bar{\bar{d}}$ is the deformation rate tensor. Temperature distribution in the fluid is determined by solving the energy equation displayed in equation 5. Iterative calculations to solve Navier-Stokes equations were carried out by the SIMPLE scheme for pressure-velocity coupling.

Table 6 Properties of IR laser, fluid, and nanoparticles in the simulation

Symbols	Values
Q_0	1 mW
R_c	0.56
A_c	3.67e7 m^{-1}
r_x	0.5 μm
r_y	0.5 μm
ρ	1,000 kg m^{-3}
ρ_p	1,050 kg m^{-3}
d_p	100 nm
μ	0.001 Pa s
γ	1e-6 m^2 s^{-1}
α	6.9e-5 K^{-1}
g	9.8 m s^{-2}
C_p	4.19 J g^{-1} K^{-1}
k	0.58 W m^{-1} K^{-1}
D_T	0.792 μm^2 s^{-1} K^{-1}
S_T	0.18 K^{-1}
D	4.4 μm^2 s^{-1}

The continuous phase model was implemented using COMSOL (Burlington, MA). The transport of species model was modified to include the thermophoretic flux term $D_T c \nabla T$ [73] and solved together with laminar flow and heat transfer models. For discrete phase model, ANSYS Fluent (Canonsburg, PA) was employed to simulate heat transfer, laminar flow, and particle tracking in 3D [151]. Nanoparticles with a diameter of 100 nm were randomly injected in the 3D microfluidic chamber. For both cases, the proper mesh

size was confirmed to attain a spatial convergence. All data were acquired at the quasi-steady state. All the parameters in the simulation is listed in Table 6.

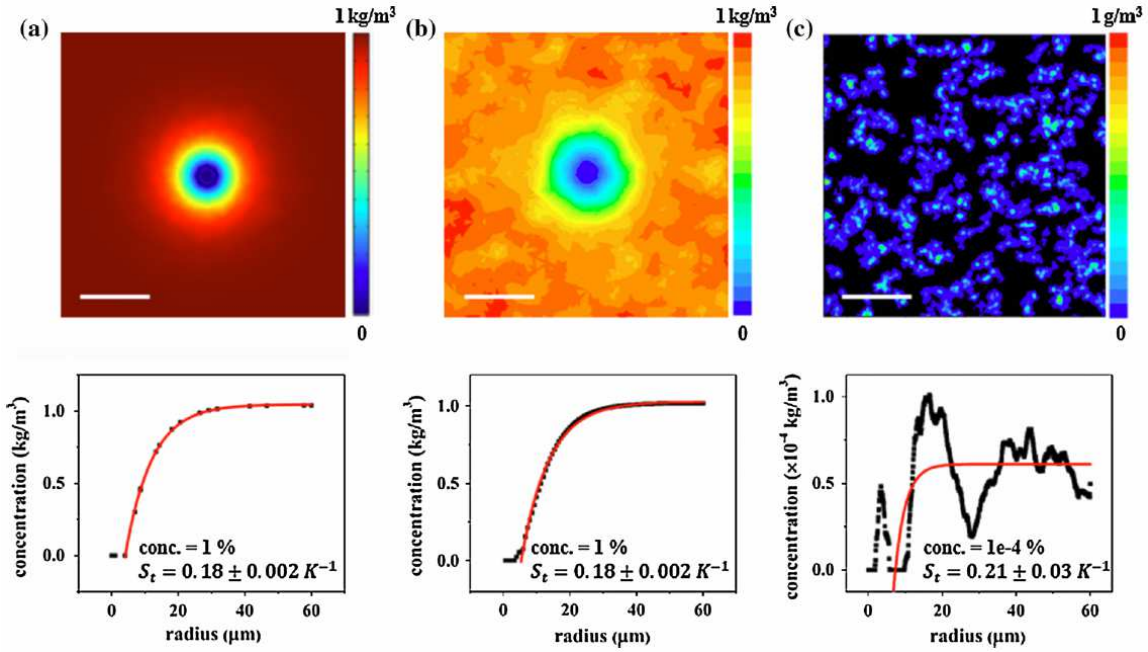

Figure 26 Concentration contour (top) and radially averaged concentration profile (bottom) for a) continuous phase modeling with concentration at 1% (*v/v*), b) discrete phase modeling with concentration at 1% (*v/v*), and c) discrete phase modeling with concentration at 1e-4% (*v/v*). The black dots in the bottom panel show the radially averaged concentration, and the red lines are fittings based on the depletion law in Eq. 1. Scale bars = 30 μm.

In response to a temperature gradient, thermophobic species move away from the high temperature region. The continuous phase model predicts that the steady-state concentration follows an exponential depletion law controlled by S_T. The image in Fig. 26a shows a simulated concentration contour at the steady state by the continuous phase model. The simulated volume is 360 μm × 360 μm × 6 μm and the center plane (z = 3 μm) with an area of 120 μm × 120 μm is analyzed here to avoid boundary artifacts. Since the height is only 6 μm, natural convection in the z-direction is negligible [76], so a 2D distribution profile in the x-y plane is expected. S_T of 0.18 1/K is used in the simulation, which was previously reported for 100 nm polystyrene particles in water [73]. The radially averaged concentration profile (Fig. 26a, bottom) is smooth, corresponding

to a continuous phase distribution. Fitting the non-zero region of the distribution to the exponential depletion law, a Soret coefficient of 0.18 ± 0.002 1/K is obtained, matching the set value for the simulation.

When the target is considered as a discrete species, its concentration is expected to fluctuate in space. To demonstrate this effect, a discrete phase model was set up using parameters relevant to 100 nm polystyrene particles. This model was firstly used to validate against the continuous phase model using a high particle concentration of 1% (*v/v*) (Fig. 26b), which yields ~1 million particles in the region of interest (ROI). The concentration fluctuation in the bulk is much smaller than the difference generated by the temperature gradient, thus the radially averaged concentration profile is smooth and the extracted Soret coefficient matches the set value.

When the particle concentration is reduced to 1e-4% (*v/v*) in the discrete phase model, the concentration fluctuation in the bulk is at a comparable level to the difference generated by the temperature gradient (Fig. 26c). Here, ~180 particles are present in the ROI, which is much less than the mesh number of ~15,000. The instantaneous concentration contour shows the location of individual particles, while a large volume in the bulk has no particle. Thus, the thermophoretic depletion in the center is much less obvious. Even after radial averaging, the bulk distribution is not smooth. Fitting the averaged concentration results in a Soret coefficient of 0.21 ± 0.03 1/K, which is 16% higher than expected.

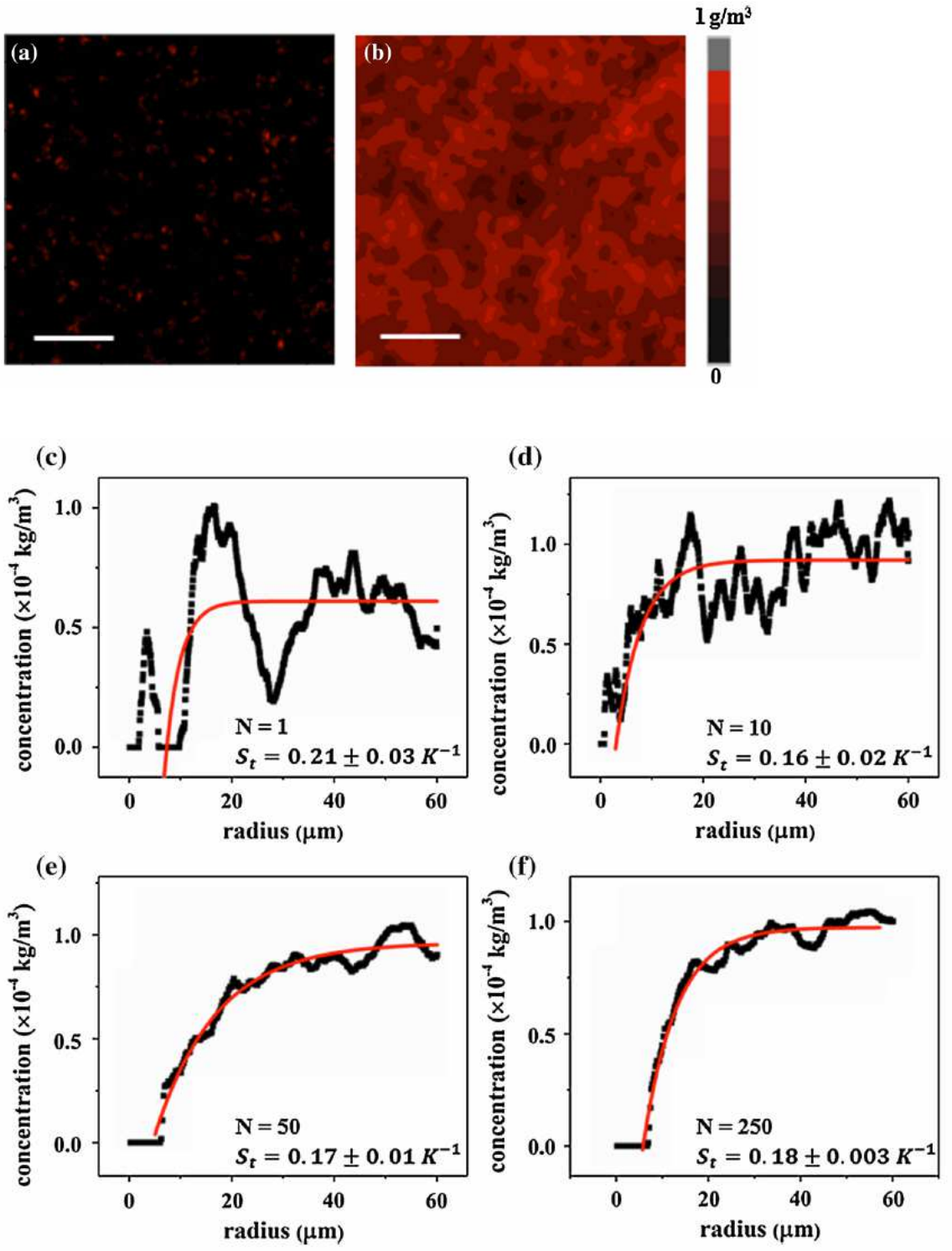

Figure 27 Simulated concentration contour for a) 1 snapshot and b) 250 overlays of nanoparticle distribution in response to a radially symmetric temperature gradient. Both images are 120 μm by 120 μm and the particle concentration is 1e-4% (*v/v*). Radially averaged quasi-steady concentration profiles of c) 1 snapshot, d) 10 overlays, e) 50 overlays, and f) 250 overlays from the discrete phase model. The black dots show the radially averaged concentration, and the red lines are fittings based on the depletion law in Eq. 1. Scale bars = 30 μm.

To increase the number density of targets in the ROI for a low concentration sample, snapshots of concentration contours from the discrete phase model were superimposed. The number density is the summation of particle number over several snapshots divided by the surface area. Mathematically, the number density is the multiplication of particle surface number density and number of snapshots. Images were acquired in the x-y plane at $z = 3$ μm with a time interval of 1 second after the particle distribution in the discrete phase model reached a quasi-steady state. Similar to the Kalman filter, the signal to noise ratio, which is the ratio between coefficient estimate and respective standard error, is expected to improve with this practice. The depletion in the center is much more obvious for 250 overlays compared to a single snapshot (Fig. 27a, b). Fig. 27c-f shows the radially averaged concentration profile for different numbers of overlays of 10, 50 and 250. The concentration profiles become smoother and the depletion center is more pronounced with the numbers of overlays. For the overlays of 250 images, the derived S_T is 0.18 ± 0.003 1/K, matching the set value of 0.18 1/K for the simulation.

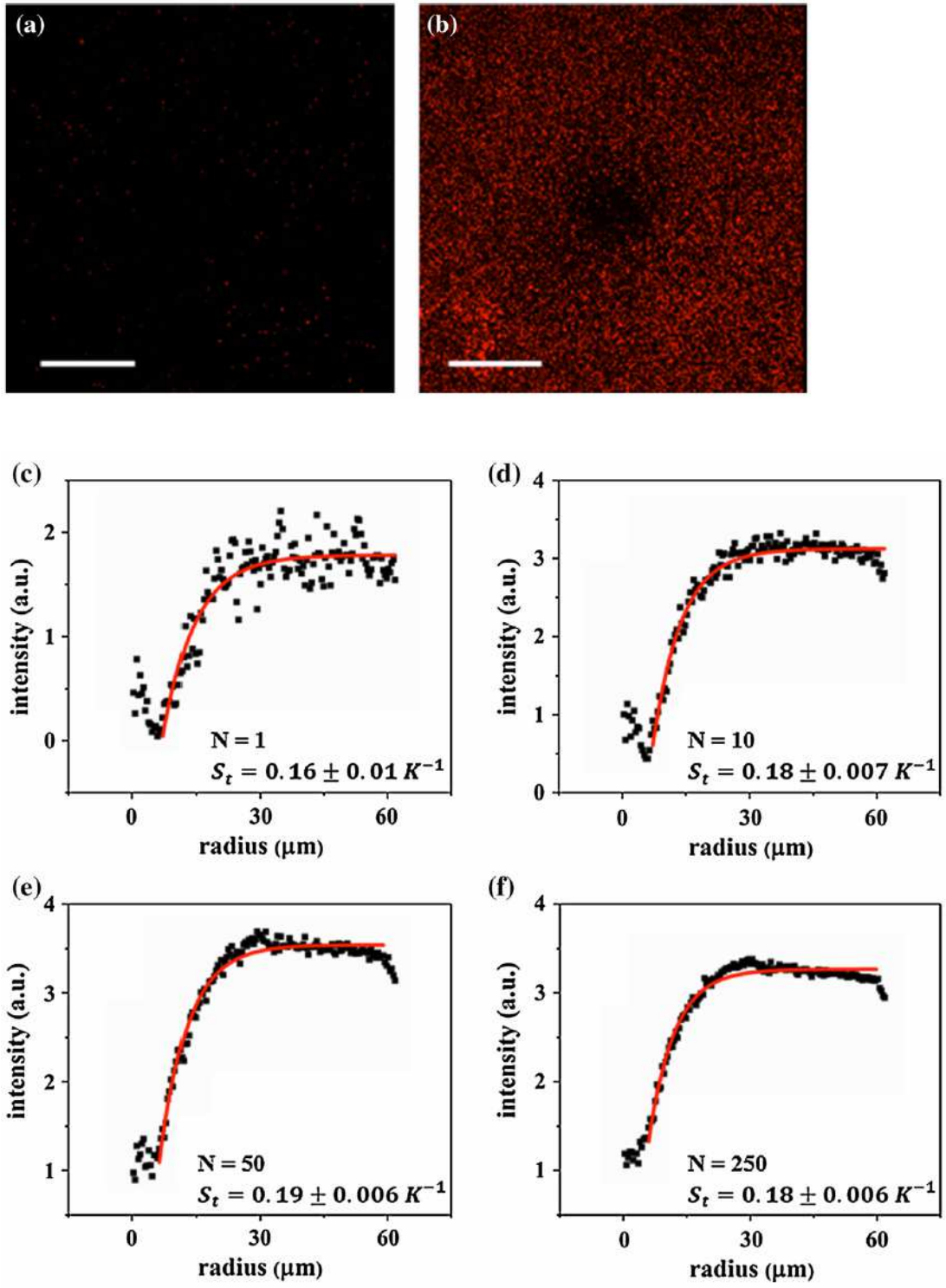

Figure 28 Experimentally measured distribution of 100nm polystyrene nanoparticle in response to a radially symmetric temperature gradient for a) single snapshot and b) 250 overlays. Both images are 120 μm by 120 μm. Radially averaged concentration profiles at quasi-steady state from c) single snapshot, d) 10 overlays, e) 50 overlays, and f) 250 overlays. The concentration of the polystyrene particle suspension is 1e-4% (*v/v*). The black dots show the radially averaged concentration, and the red lines are fittings based on the depletion law in Eq. 1. Scale bars = 30 μm.

Since the discrete phase model supports construction of a low standard error depletion profile by superimposing, experiments were carried out to validate the procedure. Polystyrene beads at a concentration of 1e-4% (*v/v*), i.e. 320 pM were used first, comparable to that in the simulation. A liquid film 6 μm thick was constrained between a chromium coated coverslip and a glass slide. Images were taken 3 μm above the bottom glass slide. Similar to the simulation, fluorescence images were acquired every second after the system reached quasi-steady state. Similar to Fig. 27a and 27b, Fig. 28a and 28b show the confocal fluorescence images for one snapshot versus 250 overlays. In the single snapshot, the particle distribution is stochastic and the depletion center is hard to visualize. After 250 overlays, the depletion in the center is pronounced. Fig. 28c-f shows the radially averaged concentration profiles for different numbers of overlays in the experiments. For single snapshot, the extracted S_T is 0.16 ± 0.03 1/K. The S_T becomes 0.18 ± 0.006 1/K with 250 overlays, which matches the previous reported value [73]. When a coefficient estimate is defined as the extracted S_T and standard error is from the smooth fitting, the signal to noise ratio is about 5 for the single snapshot and 30 for 250 overlays.

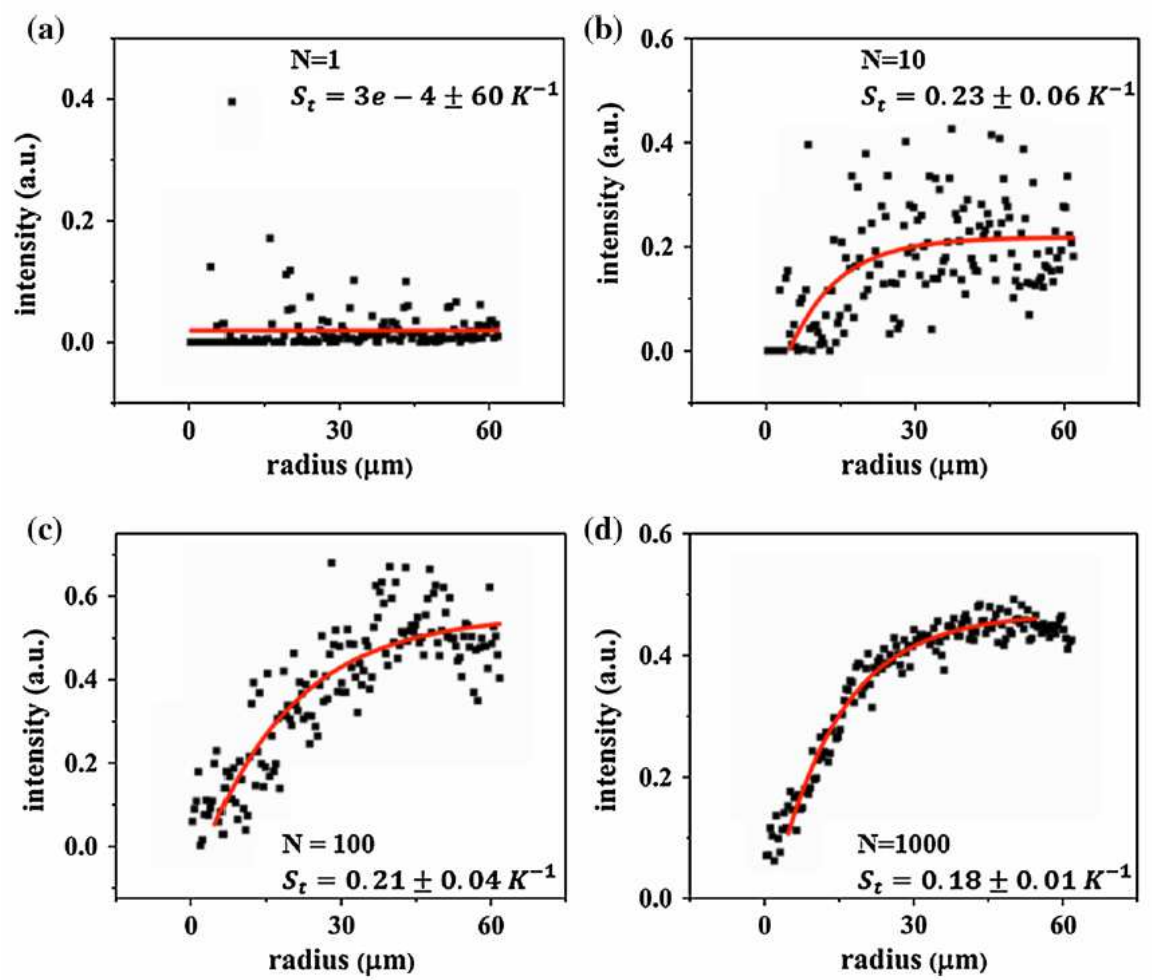

Figure 29 Radially averaged concentration profiles by experimental measurements at a quasi-steady state from a) single snapshot, b) 10 overlays, c) 100 overlays, and d) 1000 overlays. The concentration of the polystyrene particle suspension is 1e-5% (*v/v*). The black dots are radially averaged concentration, and the red lines are fittings based on the depletion law in Eq. 1.

When the particle concentration is further decreased to 1e-5% (*v/v*), i.e. 32 pM, more numbers of overlays are needed to accurately determine the Soret coefficient (Fig. 29). For a single snapshot, no thermophoretic depletion is observable even in the radially averaged concentration profile (Fig. 29a). When 10 images are stacked (Fig. 29b), the depletion is barely observable, and the extracted S_T is 0.23 ± 0.06 1/K. This number deviates from the known value of 0.18 1/K, and the high standard error roots from a sparse particle distribution. When 100 and 1000 images are overlaid (Fig. 29c, d), extracted S_T is 0.21 ± 0.04 1/K and 0.18 ± 0.01 1/K, respectively. The signal to noise

ratio reaches ~20 with 1000 overlays. Compared to the results from the suspension at 1e-4% (*v/v*), the suspension at 1e-5% (*v/v*) requires more overlays to yield a comparable signal to noise ratio.

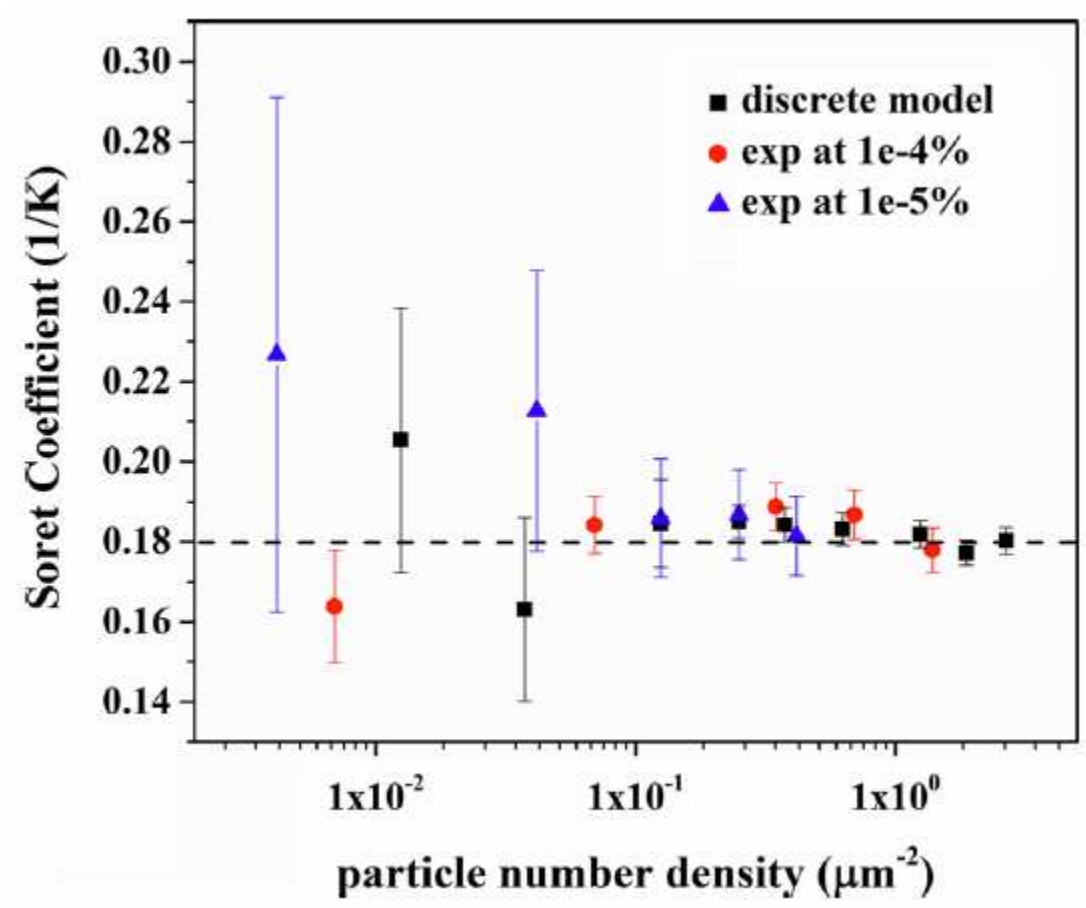

Figure 30 The relationship between the extracted Soret coefficients and particle number density from the discrete phase model and experiments with particle concentration of 1e-4% (*v/v*) and 1e-5% (*v/v*).

To compare all the data described above, we calculated particle number density in the ROI. Fig. 30 shows the extracted Soret coefficients as a function of the particle number density from all the simulation and experimental data above. The dash line represents the expected value. The experimental result from a single snapshot at a concentration of 1e-5% is not included as the signal to noise ratio is 5e-6. For all other cases, the signal to noise ratio is greater than 3.

When the particle number density is equal to or less than 0.06 μm^{-2}, the Soret coefficient extracted from the radial concentration profile deviates from the expected value by more than 20%. The large error bar indicates great fluctuation of the spatial concentration in these measurements. When the particle number density is 0.06 μm^{-2}, whether it is by increasing the suspension concentration (data not shown) or by image superimposing, the Soret coefficient converges to within 99% of the expected value with a standard error of ~0.002 1/K. More overlays generally reduce the standard error even more, since the scattered behavior is averaged and the standard deviation is inversely proportional to square root of sample number.

One possible explanation to the threshold of the particle number density to accurately predict S_T arises from the microscope resolution. When the particle number density is greater than 0.06 μm^{-2}, the average particle-particle distance is < 4 μm. This is on the same order as the spatial resolution of the microscope and nanoparticle size used in our work, thus the particle can be approximated as a continuous phase to apply the exponential depletion law. Long exposure of the sample may also result in the averaging effect, but continuous exposure may lead to sample bleaching and undesirable heating by the imaging light source.

To our knowledge, this work is the first that applies the discrete phase model to study nanoparticle thermophoresis in a liquid suspension. Discrete phase models have long been developed to understand contamination in the cleanroom and soot entrainment in the gas phase [152–156]. The thermophoretic force on aerosol particles in the gas phase is modeled using the equation proposed by L. Talbot *et al*. [157], which is directly proportional to the particle diameter, gas kinematic viscosity and inversely proportional to the particle mass. However, the relationship is not valid in the liquid phase and theoretical prediction of S_T in the liquid phase is not yet available. Instead, thermophoretic force is

implemented by the empirical Stokes law here. When coupled with the hydrodynamic and Brownian forces, the resulting discrete phase model provides an effective tool to study the distribution of nanoparticles at ultralow concentrations. As other non-conservative force fields and particle-particle interactions can be included, this discrete phase model is expected to find broad utility to study complex nanoparticle migration under thermophoresis in a liquid suspension.

The continuous phase model and discrete phase model were also studied in the thermodiffusion column system. In order to compare continuous model with discrete model, we first repeated the continuous model in [86], as shown in Fig. 31. For the thermal model, different temperatures are fixed at the side walls, and no flux conditions were assigned to other walls. For the fluid model, no slip wall condition is applied everywhere except for an outlet at the top right corner with a pressure at 0. For the species model, the initial concentration in the cell is zero, and the concentration at the top roof is fixed at one, which means a continuous feeding process. Same geometry dimension and thermal diffusion coefficient are chosen. In order to study the evolution profile of species better, concentration profiles in the transient state are also studied. Fig. 31 shows our continuous model could predict the species concentration evolution matched with literature results.

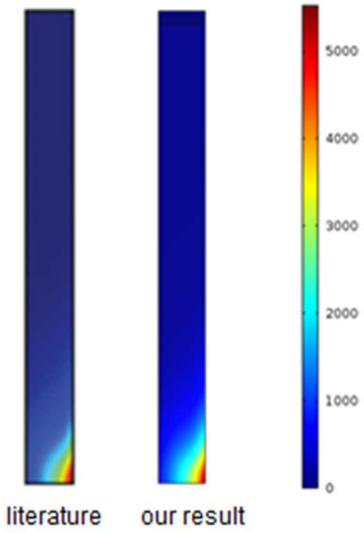

Figure 31 Comparison between [86] and our continuous model simulation shows the same steady state profile.

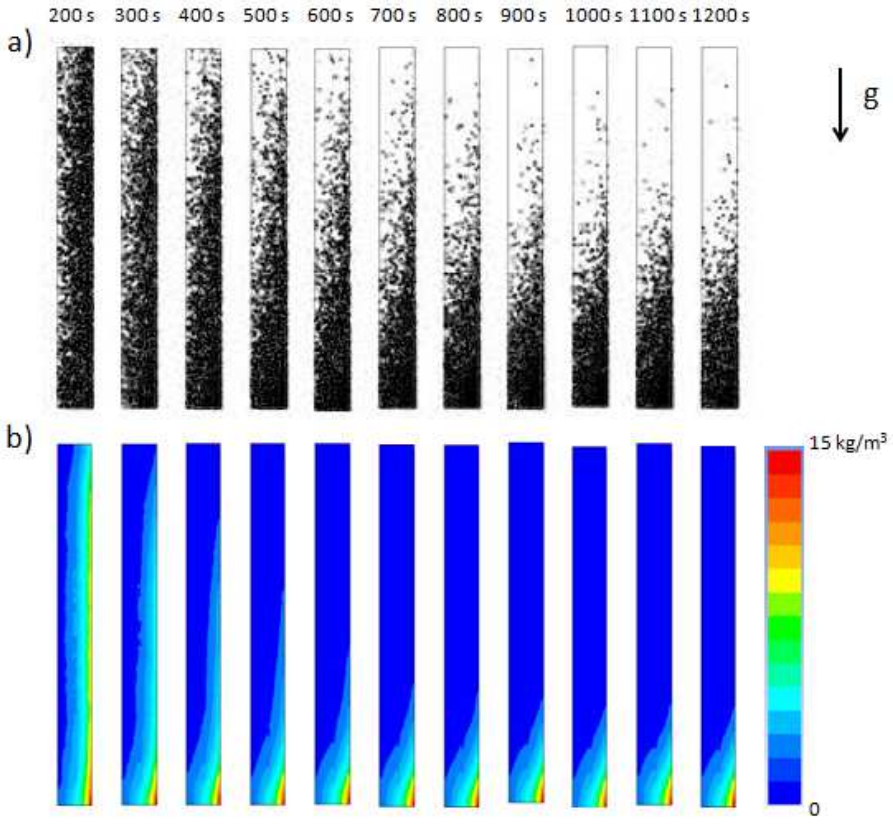

Figure 32 a) Particle tracking and b) particle concentration contour in discrete model at 200 s, 300 s, 400 s, 500 s … 1200s. Here the wall on the left is warm and the wall on the right is cool.

Particle distribution and particle concentration contour in a thermodiffusion column in the developing process is shown in Fig. 32. It is clearly shown that particles are concentrated in the bottom corner at the cooler wall. After about 1200 s, the steady state is reached.

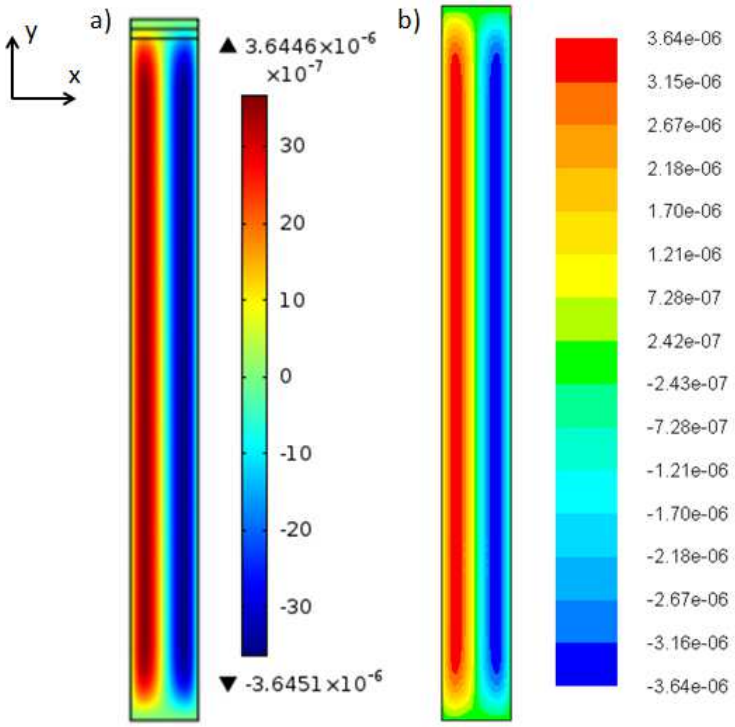

Figure 33 Contours of velocity in the y direction for a) continuous model and b) discrete model.

By comparing the flow pattern and concentration factor, the continuous model and discrete model show comparable results (Fig. 33). The steady state concentration factor also matches, but the time to reach the steady state is different. However, this time by the discrete model is consistent with the value predicted in [86]. Currently, the transient discrete model shows an oscillating concentration factor, even with a very small mesh size of 2 μm. This may be due to the intrinsic Brownian force as it introduces a Gaussian random number. To better understand the transient state, shorten time step will be taken to give more details in the developing phase.

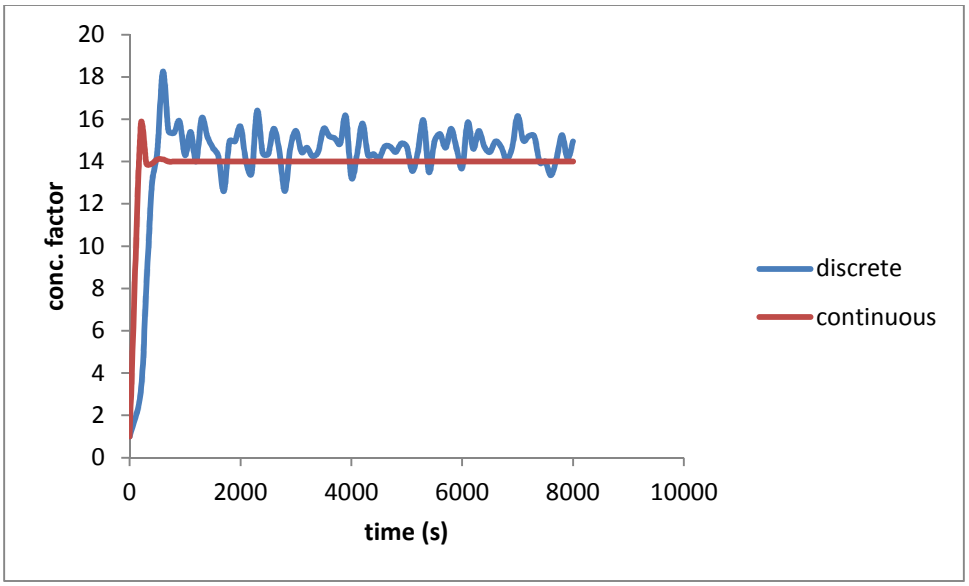

Figure 34 Concentration factor in developing stage for discrete model and continuous model.

We present an approach here to measure the Soret coefficient of a highly diluted species in a liquid suspension. By superimposing distribution images of the dispersed species, a smooth concentration profile matching the depletion law is constructed and the Soret coefficient is extracted accurately. This approach is validated using both discrete phase models and experimental measurements. The particle number density in the superimposed image needs to be comparable to the spatial resolution of the image. Also, the discrete phase model was applied to the classic thermodiffusion column system, and shows consistent result with continuous phase model. The discrete phase model developed here is shown to be useful for the study of nanoparticle migration and distribution in liquids in response to a temperature gradient.

3.2.3 Acknowledgements

We are grateful for the helpful discussions on confocal microscopy with Prof. H. Daniel Ou-Yang and Ming-Tzo Wei. Funding for the research is provided by the National Institute of Health under Grant No NIAID-1R21AI081638 and Pennsylvania Department of Health CURE Formula Funds.

3.3 Coupling thermophoresis with secondary flow in microfluidics for biological nanoparticle focusing and separation

3.3.1 Introduction

Separation and enrichment of biomolecules and bioparticles in the liquid phase are crucial for various biomedical applications, such as production of pharmaceutical compound, biosensing and decontamination [2,3,16]. Thermophoresis has been shown as an effective means to overcome diffusion and control the motion of biomolecules on the nanoscale [151]. While many other forces for manipulating colloidal particles scale with particle size and become insignificant relative to the Brownian force on the submicron scale, the force generated by thermophoresis is much less size sensitive. M. Braibanti *et al.* found that when the interfacial properties of colloidal particles are standardized, the Soret coefficient is independent of the size of the particles [79]. Although other literature [26] has reported different relationships between the Soret coefficient and particle size, it is general accepted that a non-uniform solute distribution can be established in a temperature gradient despite strong natural diffusion.

When the solute species migrates in response to the temperature gradient, a concentration gradient is set up simultaneously, which creates flux against thermodiffusion. At the steady state, a balance between thermodiffusion and ordinary diffusion leads to a predictable concentration gradient. Assuming the coefficients for natural diffusion and thermodiffusion are both constant and the temperature gradient is linear, the steady state concentration for one dimensional thermophoresis can be approximated by the exponential depletion law. It is trivial that the concentration enhancement is directly controlled by the temperature difference, which is limited to a narrow range for biocompatibility considerations. In order to boost the concentration factor in a reasonable temperature range, thermodiffusion columns have been devised that couple

thermophoresis with advection and extremely high concentration factors have been achieved in a biologically friendly setting [88]. A thermodiffusion column is a closed capillary tube with a large aspect ratio, and a temperature gradient is generated between the two side walls [24] (Fig. 35a). A thermophobic solute in the column migrates along the temperature gradient to the cold wall. At the same time, thermal expansion of water introduces a natural convection that sweeps solute at the high concentration side to one corner. As a result, the local concentration in the corner is boosted by several orders of magnitude compared to the bulk.

Concentration enhancement of various bioparticles and biomolecules in a thermodiffusion column has been reported in the literature [86,88,94] (Fig. 35a-b). DNA has been commonly used in these studies due to its biological relevance, versatility and temperature tolerance [147]. Finite element analysis predicts that DNA concentration in a thermodiffusion column can be enhanced by up to 8 orders of magnitude [86]. In the presence of nucleotides, polymerization and accumulation is mutually self-enhancing, resulting in a hyper-exponential escalation of polymer length [94] (Fig. 35c). Besides DNA, oleate has been shown to form vesicles of bilayer membranes after being concentrated and focused in a thermodiffusion column [88]. Geologically, thermal gradients were the most abundant dissipative systems on the early earth. The hydrothermal vents surrounded by highly porous mineral precipitates very much resemble natural thermodiffusion columns, thus formation of high molecular weight nucleic acid chains and vesicles provides a plausible explanation to the prebiotic evolution [86].

While it is challenging to observe molecular migration *in situ* in a thermodiffusion column with a gap of tens of microns, D. Braun *et al.* used a highly focused IR laser to generate coupled thermophoretic depletion and local advection in a simple microchamber (Fig. 35d). The pattern and magnitude of DNA accumulation are controlled by the chamber height.

This design allows real time and quantitative analysis of solute redistribution in a temperature gradient [84]. After this pioneering work, moving laser was used to introduce convection similar to those in thermodiffusion columns [87]. This convection together with the temperature gradient generated by the laser drives DNA replication in the concentration zone. A microscale analogue of a conveyor belt was also designed with a moving IR laser to dynamically relocate concentration zone of polystyrene beads and DNA [89]. These studies of focusing biomolecules in the soluble phase hold a potential to detect bioanalyte at an ultra-low concentration. The method based on microscopes and laser to map the molecular distribution in a temperature gradient *in situ* also offers a convenient means to determine the Soret coefficient.

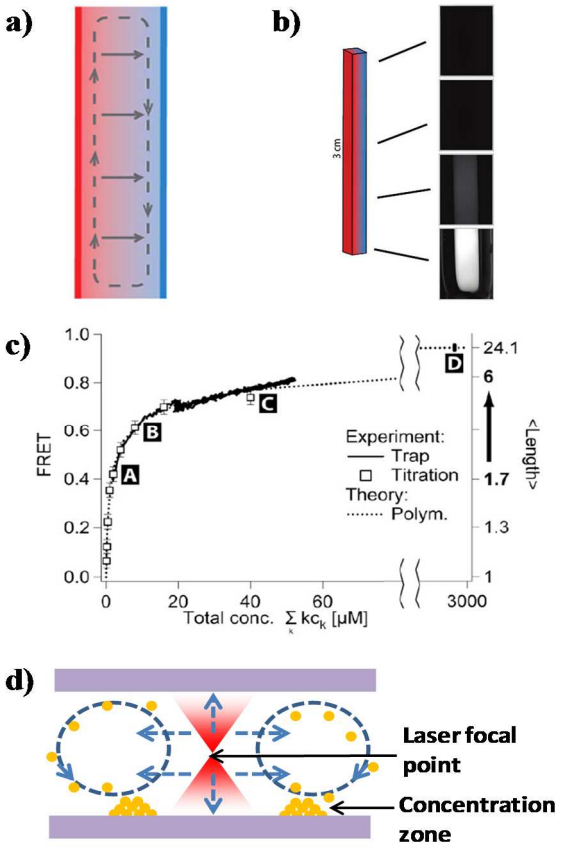

Figure 35 Concentrating and polymerizing biomolecules and bioparticles by thermophoresis (Figures from [22], [37] and [4]). a) Schematic diagram of a thermodiffusion column showing coupling of convection (dashed path) and thermophoresis (solid arrows). b) Fluorescence microscopy images of a linear capillary revealing a strong concentration gradient of 8-hydroxypyrene-1,3,6 -trisulfonic acid salt (HPTS) from top to bottom after 24 hour at ΔT = 30K [88]. c) Measurement of mean length of polymerized RNA as a function of monomer concentration in a thermodiffusion column [94].d) Enrichment of molecules on the floor of a microchamber driven by laser induced thermophoresis and natural convection (adapted from [84]). The dash lines represent the direction of convection and thermophoresis.

In the thermodiffusion column, the convective flow was purely originated from natural convection caused by thermal expansion of water and the velocity profile is not under control. However, recent development of microfluidic devices opens a door to introduce submicron flow pattern in a microchannel. Gravity induced swirl of nanoparticles in microfluidics is realized in our lab [151]. Different secondary flow patterns were explored by centrifugation force, gravitational force, etc [158]. In Fig. 36a, secondary flow is introduced by the Dean force in a curved channel, and it is intensively explored to focusing and separating microparticles and cells by coupling the Dean force, lift force and inertial

force. In Fig. 36b and c, secondary flow caused by density stratification and herringbone pattern on the channel wall were reported. However, how the secondary flow influence thermophoresis is not clear and not yet studied.

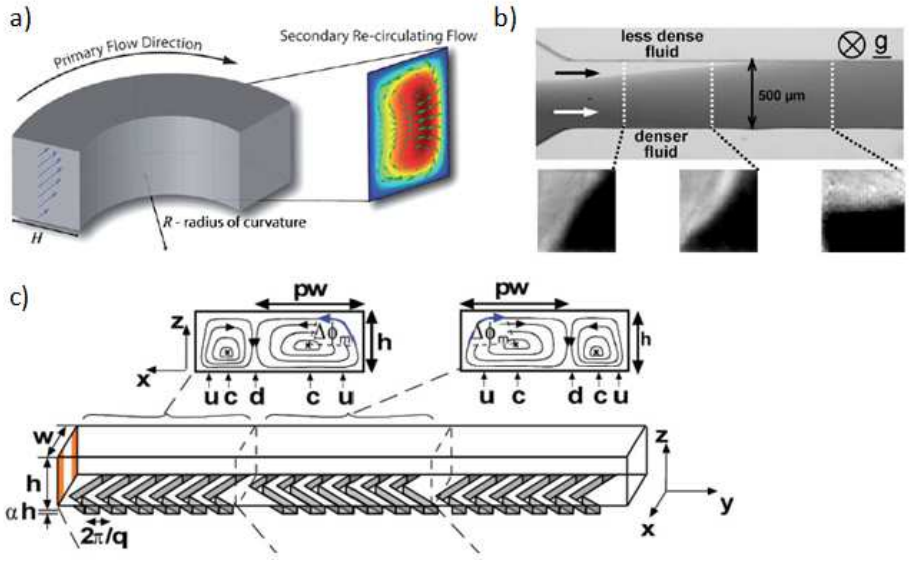

Figure 36 Current generation of secondary flows by Dean flow [4], gravity stratification [61], and Herringbone pattern [113].

3.3.2 Results and conclusion

In order to better understand the thermophoresis effect, experimental setup is prepared to compare predicted simulation results and experimental data. Steady state concentration profiles of HPTS, dCTP, 20-mer dA, and oleate were mapped in a thermodiffusion column in the literature, but no dynamic analysis have been reported in a column format [88]. To perform real time measurements, we used a rectangular capillary, with a cross-sectional dimension of 200 μm x 4 mm, as the thermodiffusion column. The glass capillary channels were selected for their smooth and optical friendly walls. The capillary was sealed by uncured PDMS on both ends. In order to introduce a temperature gradient in the channel, the capillary was clamped between a thermoelectric heater and ice water bath cooler. The assembled device is shown schematically in Fig. 37. The device was then imaged on inverted fluorescence microscope and confocal

laser scanning microscope. Due to the scattering effect, the capillary can be imaged within 150 μm from the bottom.

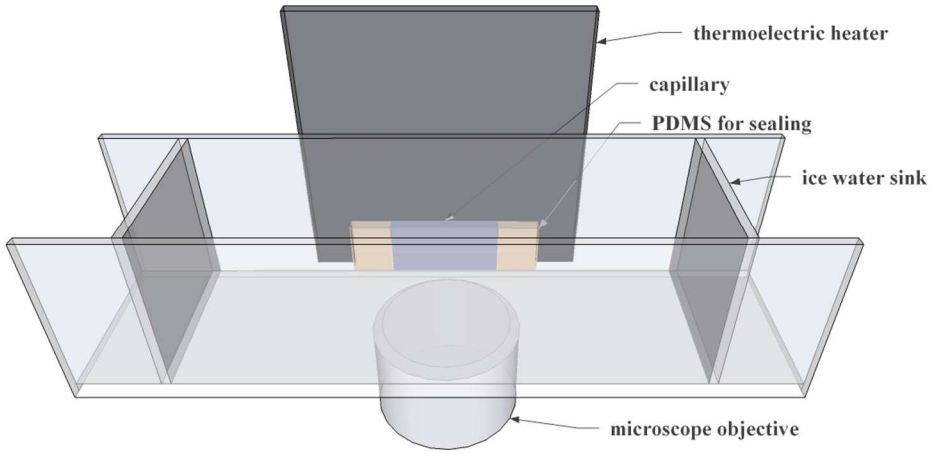

Figure 37 Schematic drawing of the assembled system for creating a temperature gradient in a channel.

In order to characterize the temperature within the channel, the relationship between fluorescent intensity of Rhodamine B and temperature in a capillary was also measured (Fig. 38). Different temperatures were cycled in the process of measurement, and no hysteresis effect was observed. In addition, no evidence of quenching of the rhodamine dye was observed after 60 min of constant exposure to the excitation light. Then the dye was put in a channel with a temperature gradient as a temperature indicator.

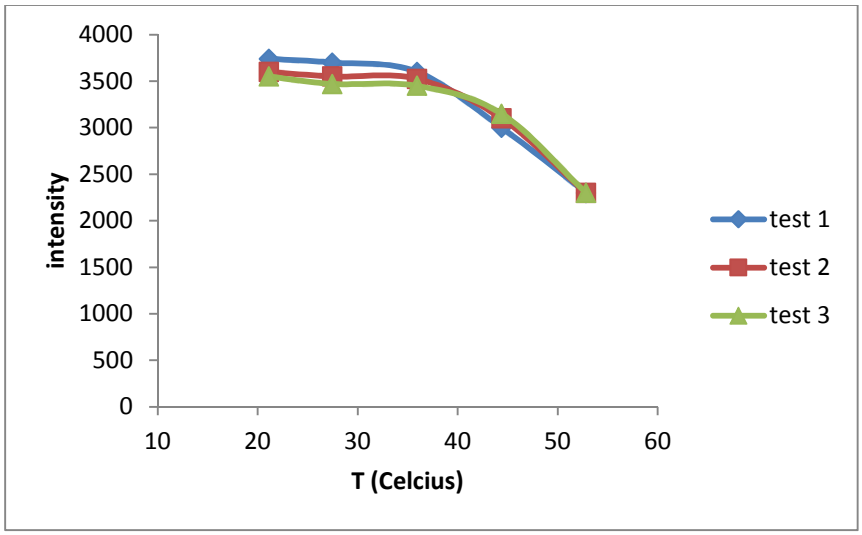

Figure 38 Relationship between temperature and fluorescent intensity.

In the assemble device with polystyrene beads, convective, unicellular flow caused by thermal expansion of water was confirmed by visualization of the swirling flow pattern of 1.5 μm polystyrene beads under a temperature gradient (Fig. 39).

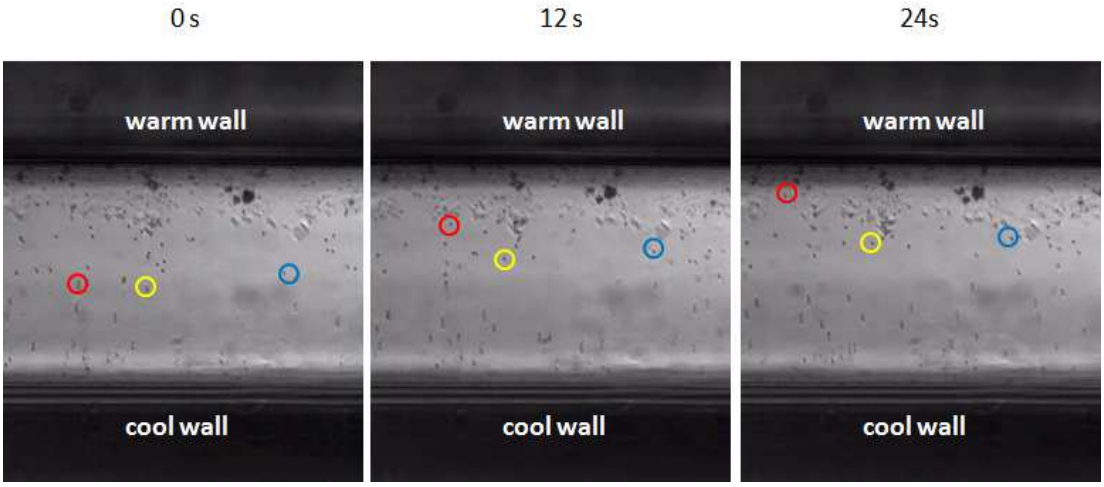

Figure 39 Migration of 1.5 μm polystyrene beads within the temperature gradient from natural convection (bottom view).

To appreciate concentration enhancement through secondary flow, prototype secondary flow was introduced by moving the warm wall of a thermodiffusion column. In Fig. 40, if the wall moving direction is the same as the natural convection, the concentration factor

is lower, and if the direction is opposite, the concentration factor is higher. The change of the concentration factor is even more dramatic when the warm wall moves at -10 μm/s. The simulation results strongly suggest that maximal focusing effect can be engineered through controlling the secondary flow.

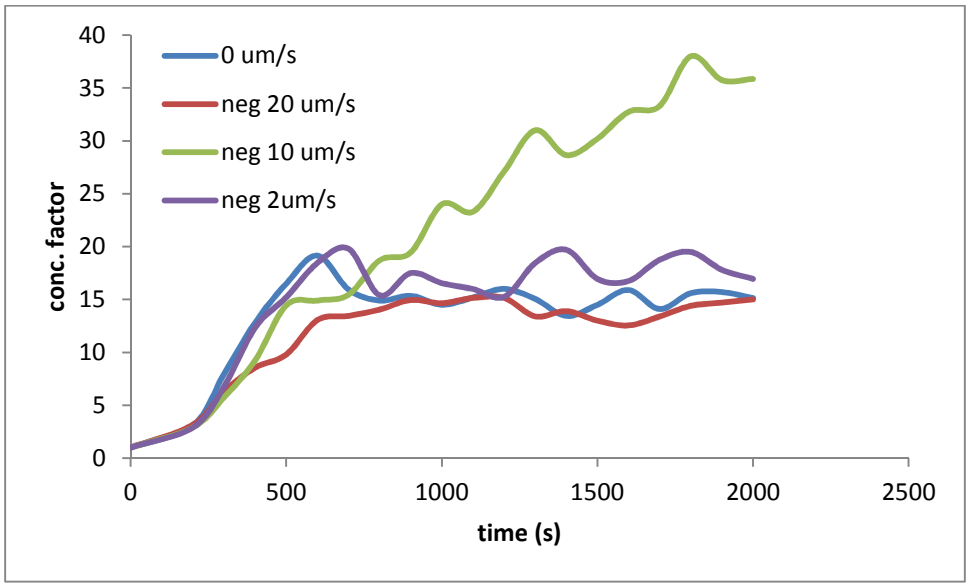

Figure 40 Discrete modeling of dynamic concentration factor under different velocities of moving walls.

In a thermodiffusion column, different sized particles will have distinct steady-state distribution with the highest concentration next to the wall. However, the dynamics differ depending on particle size (Fig. 41). For example, 200 nm PS particles have a 40 times higher concentration factor than 50 nm PS particles, but the developing time is 4 times longer (Fig. 42).

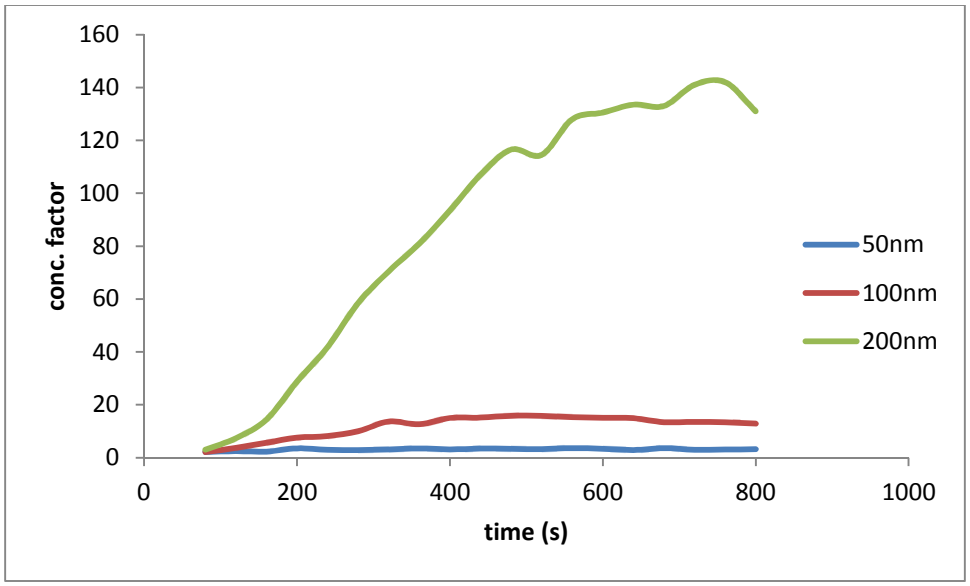

Figure 41 Discrete modeling of dynamic concentration factor for different sized particles in a thermodiffusion column.

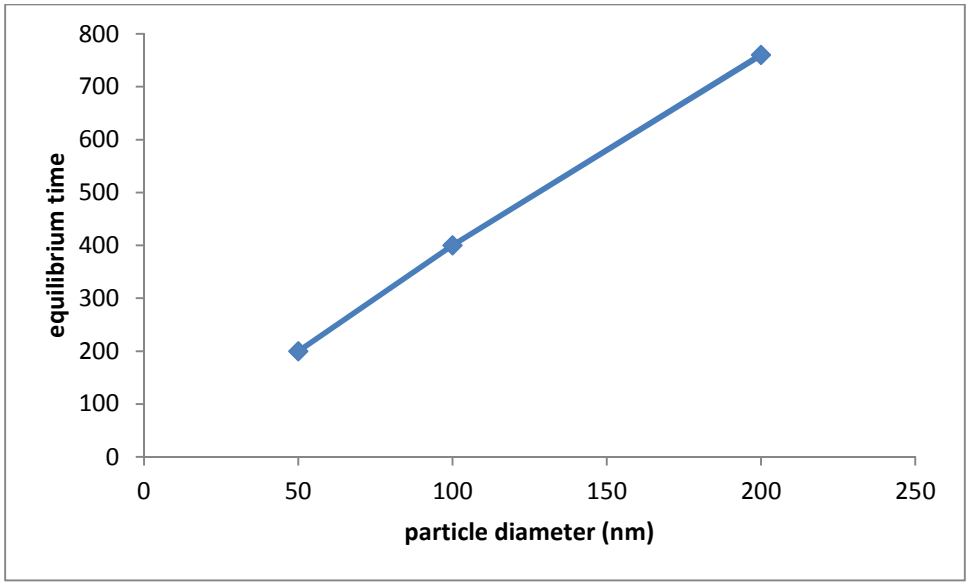

Figure 42 The relationship between the particle size and time to reach equilibrium state.

Enriching nanoparticles, both biological and synthetic ones in an aqueous solution, is commonly practiced for various applications. A general method to focus nanoparticles in a microfluidic channel in a label free and continuous flow fashion is not yet available, due to a dominant Brownian force. Recent research of thermophoresis indicates that thermophoretic force can overcome Brownian force to direct nanoparticle movement.

Coupling thermophoresis with natural convection on the microscale has been shown to induce significant enrichment of biomolecules in a closed capillary called a thermal diffusion column. However, the sample volume and throughput are not practical, due to difficulty to independently control thermophoretic and the convective transport, and the concentrated samples are hard to retrieve. We recently designed a microfluidic device that couples a helical recirculation and a temperature gradient to achieve effective nanoparticle focusing in a continuous flow. Swirling in the transverse plane is introduced by micropatterned parallel microgrooves and the swirling velocity is tunable. Here, COMSOL simulation is used to study how the microfluidic geometry and flow condition control nanoparticle side migration along an axial flow. The results demonstrate that the microgroove depth, width, spacing and tilting angle all influence the speed and steady state of nanoparticle focusing. Further dimensional analyses reveal that the ratio between the thermophoretic and convective fluxes governs the concentration factor, which reaches maximum when the ratio is approximate one. This simple relationship provides fundamental insights about nanoparticle transport in coupled convective and temperature fields. This study also offers a useful guideline to the design and optimization of nanoparticle concentrators based on coupled thermophoresis and engineered helical convection.

Enriching nanoparticles in an aqueous solution is a critical step in the preparation of many nanomaterials and analysis of nano-analytes [22,159,160]. While conventional methods, i.e. high-speed centrifugation and ultrafiltration, are effective and generally applicable, these batch processes require bulky instrument, extensive infrastructure and long processing time. Recent advances in lab-on-a-chip technologies have led to the development of microfluidic concentrators for microparticles, employing various physical mechanisms such as centrifugation [29,30], inertia-driven flow [2], dielectrophoresis [161],

optical trapping [162], acoustophoresis [163], etc. But these approaches are mostly ineffective for nanoparticle processing due to scaling of the involved forces with particle volume and strong Brownian motion of submicron and nanosized species. Microfluidic filtration devices [164] based on the size exclusion principle face similar challenges as their macroscopic counterparts, i.e. clogging and high back pressure. Capillary electrophoresis [165], including recent development utilizing the ion concentration polarization phenomenon, has achieved biomolecular enrichment by orders of magnitude [166]. However, the performance is influenced by electrochemical reactions and hydrolysis. Affinity capture [167] on solid capture bed or by magnetic particles have shown promising results for the separation of nanovesicles and viruses [22], but the requirement of labeling limits their application to species clearly presenting surface epitopes.

Recently, thermophoresis has been proposed as a strategy to manipulate the motion of solutes in aqueous solutions without the need of labeling. Thermophoresis is the migration of species under a temperature gradient and has long been studied as a means for molecular enrichment [25]. Initially, thermophoresis was applied to species in the gas phase, and shown to concentrate isotopes when it is coupled with natural convection in a thermal diffusion column [24]. Only in the past three decade has thermophoresis been investigated carefully in the aqueous phase, and found as an efficient technique for colloidal crystallization, droplet and bubble manipulation as well as molecular assembly. [86,94,121,168–170]. Based on a similar setup as the thermal diffusion column, researchers [84,86] predicted concentration enhancement of nanospecies in the liquid phase, and empirically observed enrichment of DNA, organic compounds and polymers [87,88,94].

The thermal diffusion column, however, lacks throughput for practical nanoparticle processing. A thermal diffusion column is a closed capillary tube with a large aspect

ratio, and a temperature gradient is generated across the capillary width. A thermophobic solute in the column migrates along the temperature gradient to the cold wall. At the same time, thermal expansion of the solvent introduces natural convection that sweeps solute along the cold wall, and recirculation of the solute is inhibited by the thermophoretic force. As a result, the solute accumulates at one corner and the local concentration can be boosted by orders of magnitude compared to the bulk. The steady-state concentration factor scales exponentially with the temperature difference and aspect ratio, and the time to reach steady state scales with the square of the column height [86]. A short and thin capillary is desirable for fast and strong enrichment, yet it limits the sample volume to be processed. It is also difficult to extract the concentrated species from the capillary.

Inspired by the concentration power of the thermal diffusion column, we have recently designed a microdevice that couples a temperature gradient with an engineered helical convection to achieve nanoparticle enrichment in a continuous flow. In the transverse plane, the combined swirling and thermophoretic transport mimic the transport in a thermal diffusion column, so nanoparticles are focused to one corner. The focusing effect develops along the axial flow until a steady state is reached. The concentrated species can be retrieved continuously from a strategically positioned outlet, opposed to batch processing in thermal diffusion columns. Another benefit of the design is to control thermophoresis and convection separately, which allow physical understanding and optimization of the enrichment process. Since thermal migration is intrinsic to all solvated species [26], no labeling is required and particles remain suspended in the focusing process. This avoids aggregation associated with pelleting in centrifugation and caking in ultrafiltration, both of which contributes to variable yields.

Vortices in a laminar flow in a microchannel can be generated by physical structures or side-by-side flow of density mismatched solutions [61,113,151,158,171]. Slanted grooves are chosen here due to its ability to generate stable transverse recirculation at low Reynolds number. While slanted or staggered herringbone grooves are usually used for passive mixing in microchannels [113,172,173], magnitude and pattern of the transverse velocity are controllable and predictable [171]. To understand how nanoparticle focusing is influenced by the groove and microchannel geometry as well as the flow conditions, when a temperature gradient is superposed on the microchannel, we performed numerical analysis using a finite element method and continuous phase model. A dimensionless analysis was also carried out to relate the concentration factor with the relative flux by transverse convection and thermophoresis, which provides physical insights about processes governing nanoparticle focusing.

Numerical analysis was performed by a continuous phase model. The governing equations to describe natural convection are Boussinesq approximation and the mass conservation equation:

$$\frac{\partial \boldsymbol{u}}{\partial t} + \boldsymbol{u} \cdot \nabla \boldsymbol{u} = -\frac{1}{\rho}\nabla p + \gamma \nabla^2 \boldsymbol{u} + \alpha \boldsymbol{g}(T - T_0)$$

$$\nabla \cdot (\rho \boldsymbol{u}) = 0$$

where ρ is fluid density, γ is kinematic viscosity, t is time, $\boldsymbol{u}$ is fluid velocity, p is pressure, α is the thermal expansion coefficient of the fluid, $\boldsymbol{g}$ is gravitational acceleration and T is temperature.

The conservation of energy is in the form

$$\rho C_p \frac{\partial T}{\partial t} + \rho C_p \boldsymbol{u} \cdot \nabla T = \nabla \cdot (k \nabla T)$$

where C_p is heat capacity of the fluid and k is thermal conductivity of the fluid.

Mass transport includes diffusion, advection and the thermophoretic flux:

$$\frac{\partial c}{\partial t} = \nabla \cdot (D_T c \nabla T + D \nabla c) - \nabla \cdot (\boldsymbol{u} c)$$

where c is the concentration of the species, D_T is the thermophoretic coefficient, and D is the diffusion coefficient.

The continuous phase model was implemented using COMSOL (Burlington, MA). The transport of species model was modified to include the thermophoretic flux term $D_T c \nabla T$ and solved together with laminar flow and heat transfer models [86]. The channel was designed to have grooves on the bottom wall [113,171], and a temperature gradient of 0.2 K/μm was established by setting temperatures on the top and bottom walls of the main channel at 296 and 306K, respectively. The temperature gradient is low enough that natural convection caused by density mismatch is negligible and engineered convection introduced by the grooves dominates, which was confirmed by inspecting recirculation velocity from natural and engineered convection respectively in the simulation. Parameters corresponding to 100 nm polystyrene particles in water was used: the diffusion coefficient was set at 4.4 $\mu m^2/s$, and the Soret coefficient set at 0.18 /K [73,118,174]. The viscosity of water was set at 0.001 Pa·s, the density at 1000 kg/m^3, the heat capacity at 4.2 J/g·K, and the thermal conductivity at 0.6 W/m·K. Gravitational acceleration is 9.8 m/s^2.

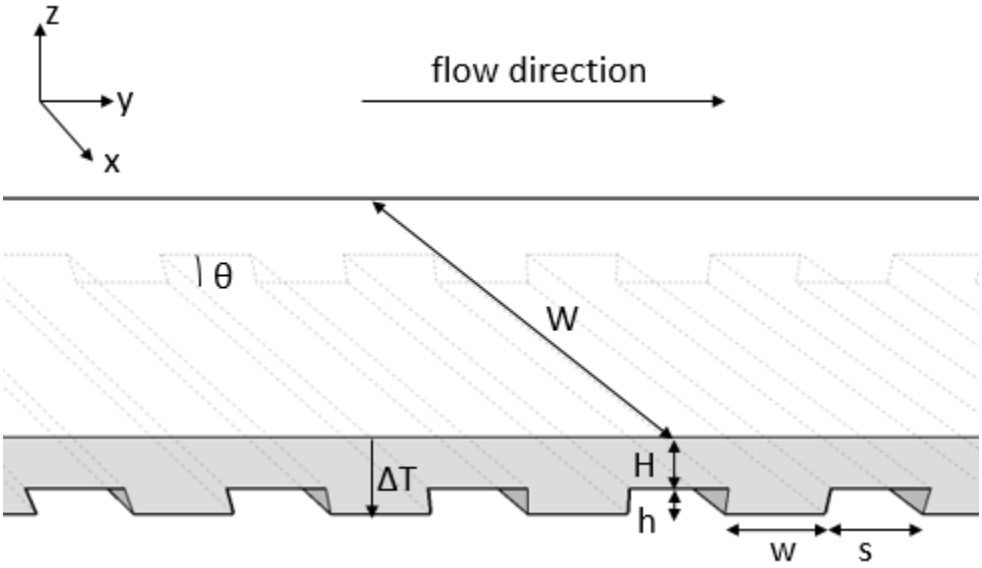

Figure 43 Schematic showing a section of the microchannel with slanted grooves at the bottom. Geometrical parameters studied in this study includes microgroove depth(h), width (w), spacing (s), tilting angle (θ), and main channel width (W). Flow rate has also been investigated.

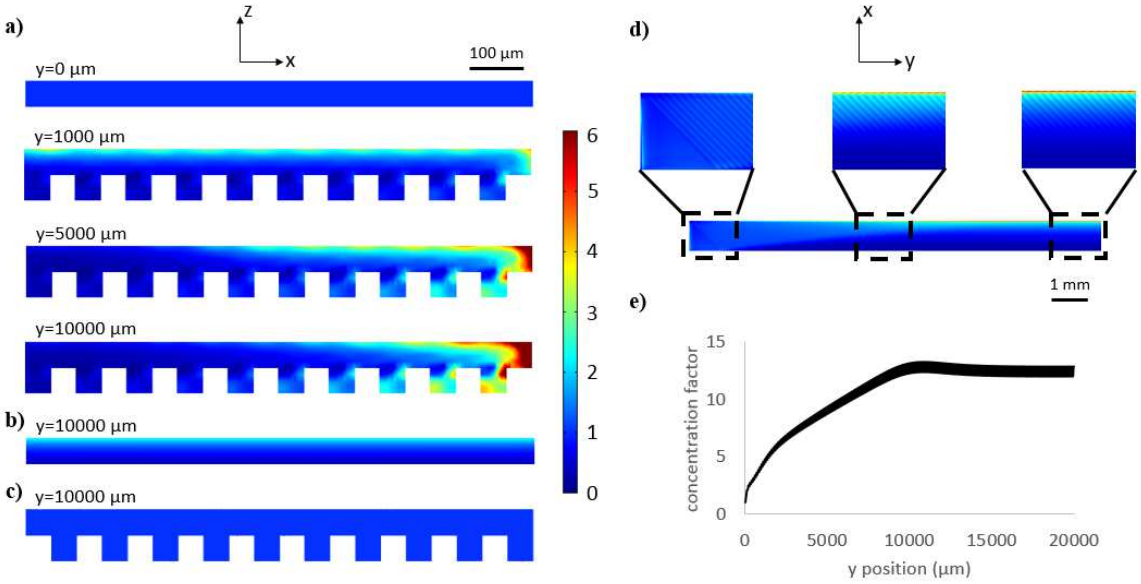

Figure 44 Concentration enhancement of nanoparticles observed a-c) at different cross sections along the y direction with ΔT = 0.2 K/µm and d) from the top of the x-y plane. Two control cross-sections are also shown in b, c) as labeled. (e) Development of concentration factor along the axial (y) direction.

The detailed structure of the slanted microgroove (SGM) design is shown schematically in Fig. 43. Geometrical parameters investigated in this study include: main channel width

(W), main channel height (H), groove width (w), groove height (h), groove spacing (s), groove angle (θ). The average axial velocity (v) in the main channel is also considered. Fig. 44 shows one example of nanoparticle redistribution in a microchannel with H=50 μm, W=1000 μm, w=50 μm, h=50 μm, s=50 μm, v=12 μm/s, θ=45° and ΔT of 10 K between the main channel floor and roof, distributed linearly in the z direction. As seen in the concentration profiles of different cross sections along the y direction (Fig. 44a) and the top view of the x-y plane (Fig. 44d), nanoparticles are initially uniformly distributed at the inlet, and gradually concentrated to one corner. The concentration at the top right corner develops along the axial flow and reaches maximum within 12 minutes (Fig. 44e). To verify that the enrichment is a combined result of transverse convection and thermophoresis, we further analyzed two control cases in the simulation: (1) the microchannel contained no grooves, but the flow rate and temperature gradient was the same as describe above (Fig. 44b) and (2) the same geometry and flow rate were used as described above, but the temperature was set uniform of 296 K (Fig. 44c). For case 1, thermophoresis only introduces a vertical migration of nanoparticles to the top wall, and the largest concentration factor is ~ 2 times compared to the initial uniform concentration. For case 2, the nanoparticle concentration remains uniform in every cross section and no focusing is observed. Additionally, nanoparticle distribution was analyzed in a flat section beyond a grooved section and species concentrated in the corner quickly diffuses to a uniform distribution, demonstrating the importance of the grooves.

The independent control of thermophoresis (through the main channel geometry) and transverse convection (through the microgroove geometry) allows fundamental study of how different transport processes interplay to promote nanoparticle accumulation. As the ratio of average transverse velocity to the average axial velocity is fixed for a given geometry [113,172], we varied the flow rate from 0.045 uL/hr to 0.15 uL/min, resulting in

average inflow velocity from 0.25 μm/s to 50 μm/s. As observed in Fig. 45, the concentration factor spans a wide range of 1 to 25 at steady state. A peak concentration is reached at ~1.5 – 3 μm/s, and the concentrated species is tightly bound. On the other hand, at higher axial velocities, the concentration zone has a tail in the z-direction, indicating the transverse velocity sweeping concentrated particles from the corner back into the channel. When the flow velocity is below the optimal, the nanoparticles are found to distribute broadly along the roof, due to weak convection that sweeps particles to the corner (Fig. 45c). Given the temperature gradient and Soret coefficient used here, the thermal diffusion velocity is ~0.16 μm/s, and characteristic time for thermophoretic transport in the z direction is ~10 min. Thus transverse sweeping is the slow process and dictates the overall time to reach steady state. For a thermodiffusion column with an inversed aspect ratio and the same temperature gradient, the average recirculation velocity is 1.6 μm/s, and a steady state concentration of 99 is reached after 6 h. The microfluidic channel presented here clearly provides freedom to control the transverse velocity and allow optimization of the accumulation effect for a given temperature gradient.

While the enrichment effect can be controlled by flow rate, the optimal flow rate and time to reach maximum concentration both limit the throughput. Since nanoparticle distribution suggests a significant role of the transverse velocity, which are controllable by the geometry of the slanted grooves, we next fixed the average inflow velocity to be 100 μm/s and varied the device geometrical parameters to study how they affect the concentration factor. The groove spacing, depth and oblique angle were varied one at a time, while the other parameters were held the same as shown in Table 7.

Table 7 Channel geometry and flow velocity in simulation

Properties	Range
Axial velocity	0.25 μm/s - 50 μm/s
Groove tilting angle	0° - 64°
Groove height	0 μm - 75 μm
Groove spacing	50 μm - 400 μm
Groove width	12.5 μm - 87.5 μm
Main channel width	500 μm - 2000 μm

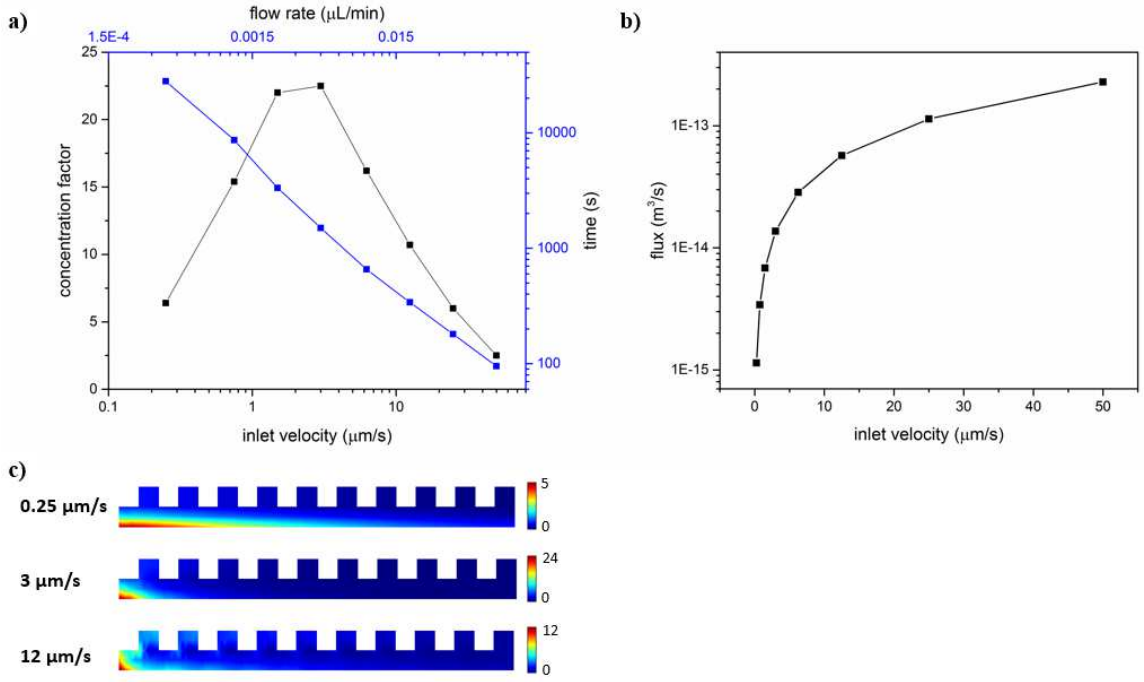

Figure 45 Relationship between concentration factor/time to reach steady state and average inflow velocity.

The first parameter studied was the groove angle. Fig. 46 shows that the magnitude of transverse velocity peaks at around 45° with the angle. The concentration factor and time to reach steady state, on the other hand, both monotonically increase with the decrease of the groove angle in the range of 14° to 64° degrees. Angles lower than 14°

could not be simulated due to excessive meshing. For example at an angle of 10°, the grooves are almost as long as the main channel and mesh number increases by 10 times compared to when angles are 45°. However, the steady state time and concentration factor is expected to drop to 40 s and 2 respectively when the groove angle is 0, driven by thermophoresis alone. A peak concentration may exist for groove angles between 0-14°. It should be noted that the low angle grooves are difficult to fabricate, thus are less practical to control the accumulation effect than some other parameters discussed below.

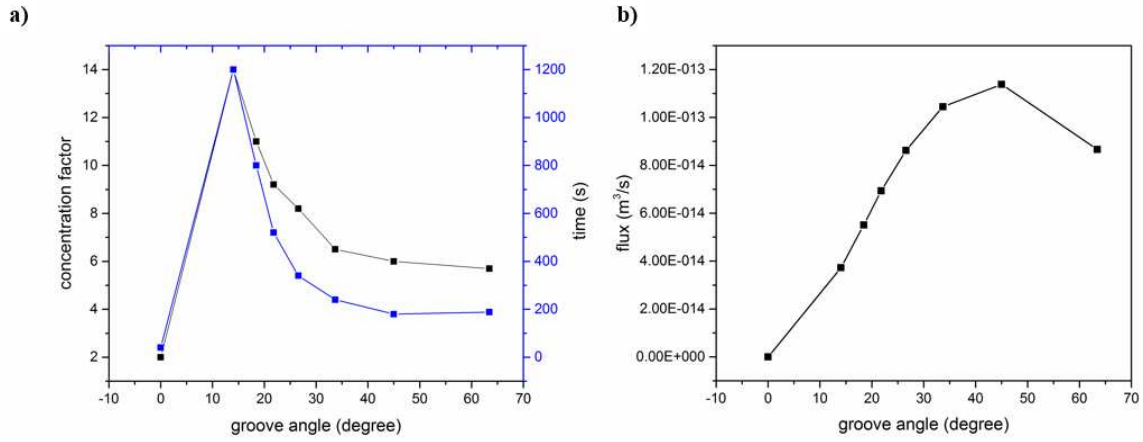

Figure 46 Relationship between the concentration factor/time to reach steady state and groove angle.

Next, groove height was studied independently with all other parameters being held constant. When the groove height is zero, the channel has a flat floor and zero vortex. The vortex strengthens with the groove height and plateaus when the height is more than 80 μm (Fig. 47). The concentration factor is boosted with dampened vortex. Fig. 47 shows that the concentration factor changes from 5 to 20 by decreasing the groove height from 75 μm to 5 μm. Simulations were unable to identify a peak in concentration factor within this range of groove heights, due to excessive meshing for even shallower grooves. Nonetheless, at a groove height of 0, the concentration factor is expected to

drop to about 2 from thermophoresis alone, thus a peak accumulation is expected with groove height between 0 and 5 μm. Compare to the groove angle discussed above, shallower grooves are easier to fabricate and thus is a more practical parameter to adjust to optimize the concentration factor.

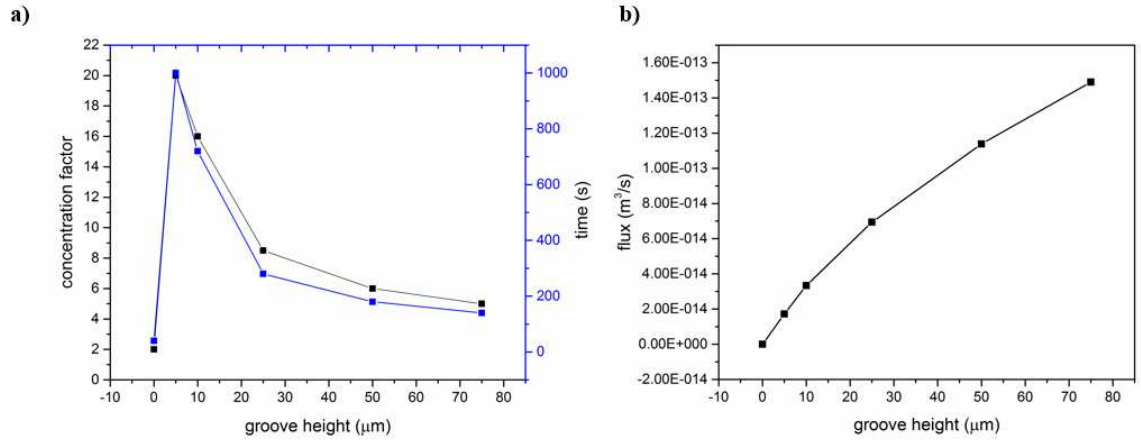

Figure 47 Relationship between concentration factor/time to reach steady state and groove height.

The third groove parameter investigated is the spacing between the grooves. In the default setup, the ratio between the spacing and groove width is one. As the spacing increases, magnitude of the swirling is reduced (Fig. 48), which lead to an increase of the steady state concentration factor. A maximum is reached when the spacing is 400 μm and steady-state concentration along flowing direction starts to oscillate when spacing is greater than 400 μm due to nanoparticles diffusing back to the channel between grooves. Under the extreme condition where the spacing to groove width ratio is infinite, no vortex exists and the concentration factor drops to about 2, driven by thermophoresis alone. In our range of parameters testing, the concentration factor varies from 6 to 13.5 with spacing changing from 50 μm to 400 μm, within 10 minutes.

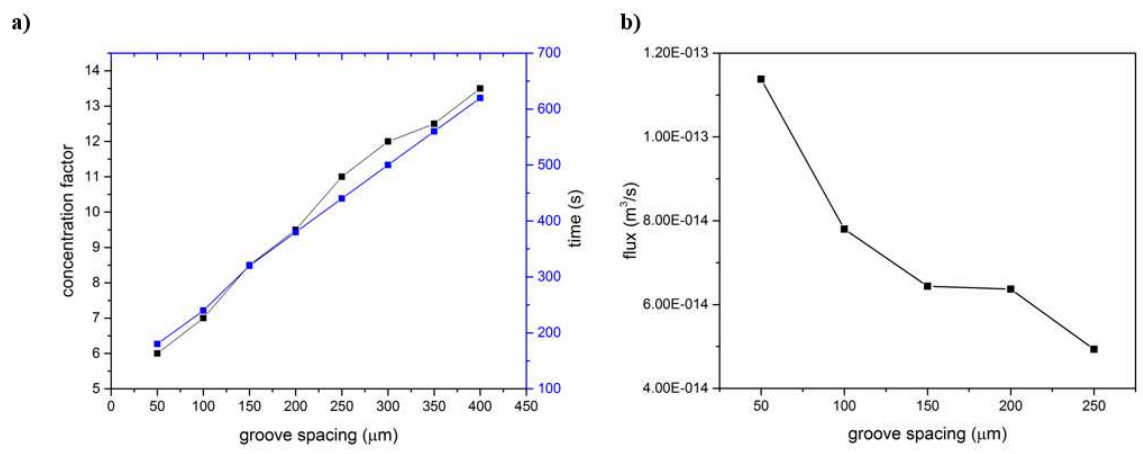

Figure 48 Relationship between concentration factor/time to reach steady state and the ratio between groove spacing and groove width.

The last groove geometry studied is the groove width. Here, the period between grooves are constant, not the spacing. If the width is 0 or infinite, thermophoresis alone will only introduce a concentration factor around 2. Between the two extremes, the swirling velocity has a plateau. Fig. 49 shows that there is an optimized groove width range from 40 μm to 90 μm. When the groove width is less than 40 μm, a dramatically diminished swirling will result in a low concentration factor, with a long time to reach steady state. Once the groove is higher than the threshold of 40 μm, the concentration factor is insensitive to the groove width until the channel becomes smooth channel when the groove width is the same as the period.

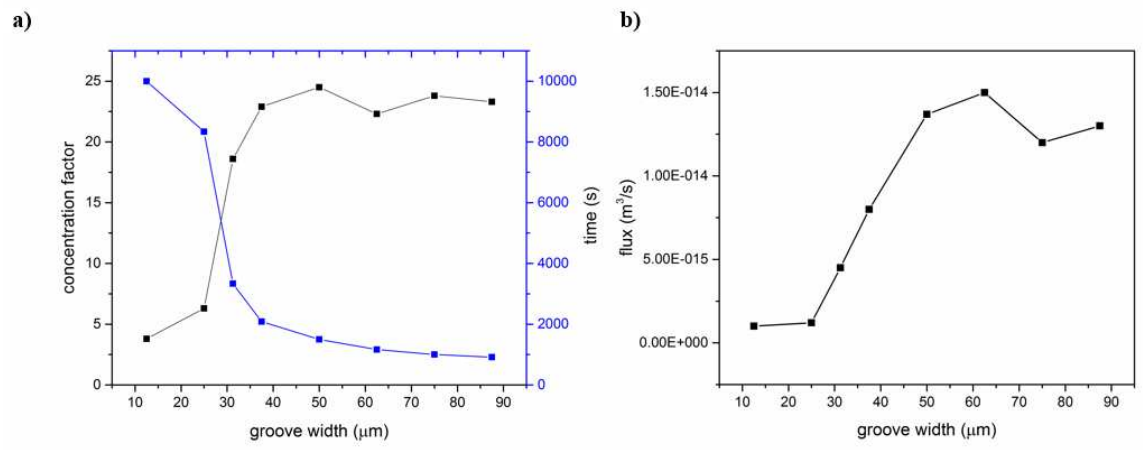

Figure 49 Relationship between concentration factor/time to reach steady state and the groove width.

In addition to the groove geometry, main channel width was also analyzed (Fig. 50). The main channel thickness was held constant to main a temperature gradient. The aspect ratio of the main channel changes from 10 to 30. The concentration factor and time to reach steady state are both proportional to the aspect ratio. This is understandable as the number of nanoparticles scale with the channel width. Furthermore, the multiplication of Soret coefficient and temperature gradient was investigated (Fig. 50). For different Soret coefficient, they show the same time to reach steady state, and much higher concentration factor for high multiplication.

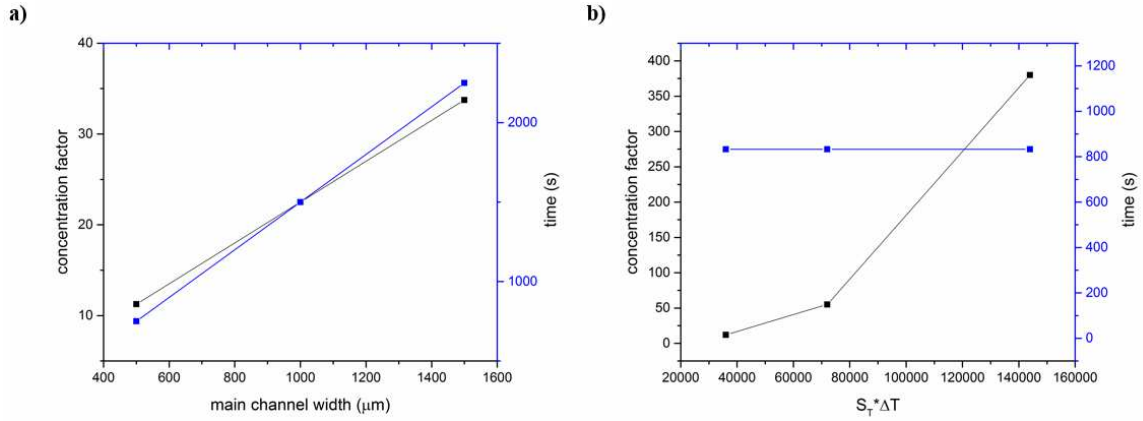

Figure 50 Relationship between concentration factor/time to reach steady state and the aspect ratio of the main channel.

The numerical analysis suggests the significance of the transverse velocity in controlling nanoparticle enrichment in our device. Since this concentrating effect is caused by coupling thermophoresis with a swirling vortex, all previous data is redrawn against a surface velocity integral along the groove cross section. Surprisingly, all previous geometrical and flow conditions fall into one master curve (Fig. 51). As we set the default velocity at 100 μm/s, most data are aggregated on the right half. However, decreasing the groove width could dramatically reduce the swirling flux, resulting in points on the left side of the bell curve. It is clearly shown that by engineering geometrical parameters, a high concentration factor can be realized even at a high flow rate through the manipulation of geometrical parameters, and the sweeping flux in the cross section along the grooves is capable of controlling the concentration factor.

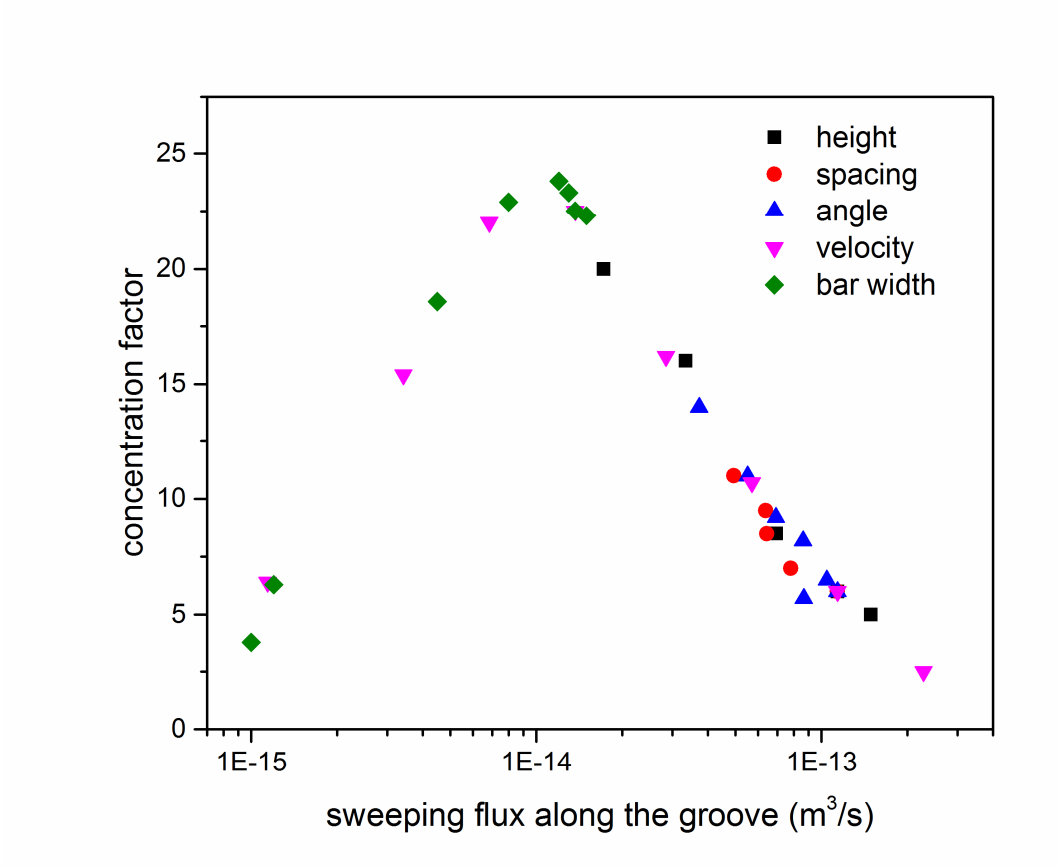

Figure 51 Relationship between concentration factor and sweeping velocity surface integral along the grooves.

The data is also plotted against the ratio between the swirling flux and the thermophoretic flux (Fig. 52). The peak's x value is very close to one. It is trivial to see that when the two transport processes are in the same order of magnitude and comparable, the system reaches its highest concentration factor. In previous studies of the thermodiffusion column, thermophoresis flux and the swirling flux could not be controlled independently, and the optimization was limited. In the microfluidic channel designed in this study, thermophoresis and swirl magnitude were manipulated individually to understand the physics of the phenomenon, and provides hints and guides in the design of similar devices to achieve the theoretical maximum concentration factor.

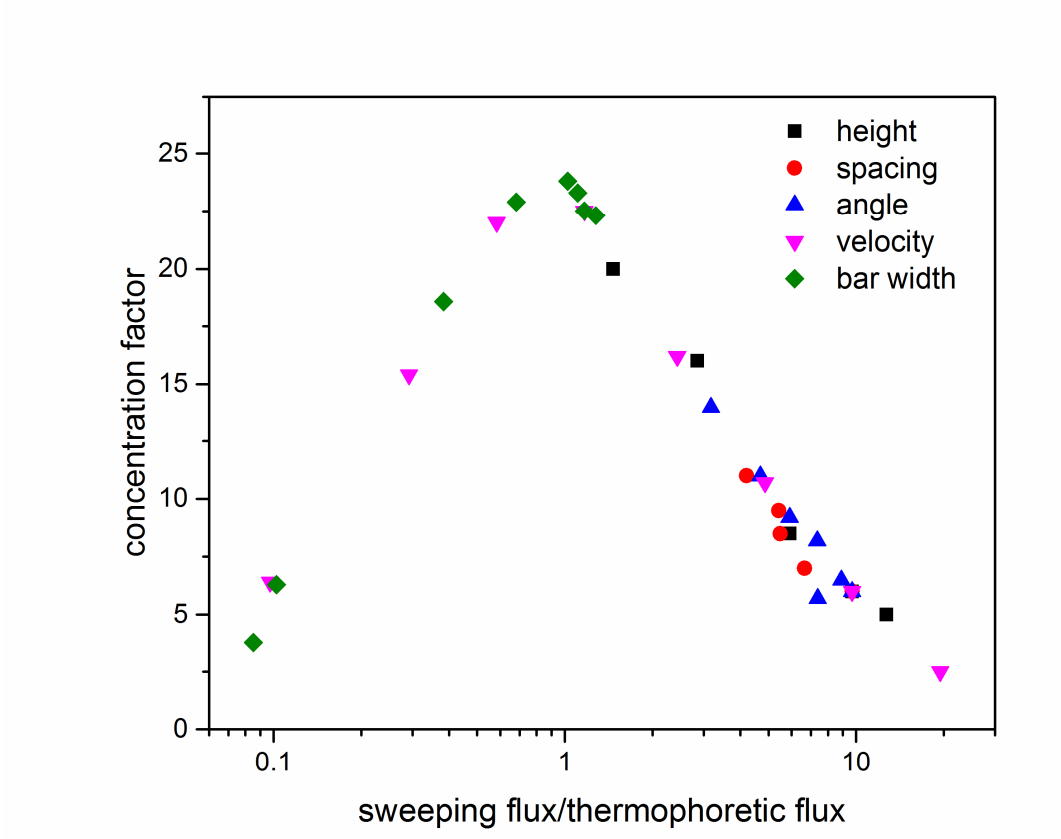

Figure 52 Relationship between concentration factor and ratio between sweeping flux and thermophoretic flux.

The general thermophoretic behavior of nanoparticles and molecules in solutions make our approach appealing and widely applicable. D_T and S_T of various solid particles and synthetic vesicles have been measured as a function of particle and solution properties [26,79,81,175,176]. Most studies report a rather narrow range of D_T from 10^{-9} to 10^{-8} cm^2 s^{-1} K^{-1} for micelles, polymers and polystyrene spheres in water up to a diameter of 250 nm, compared to the diffusivity *D* spanning more than two orders of magnitude [27,177]. This weak dependence of D_T on size drastically differs from mobility induced by dielectrophoresis, magnetophoresis, centrifugation and optical trapping, where the mobility scales with the second or third power of the particle radius, and becomes insignificant on the nanoscale. Compared with thermal diffusion column, by controlling

thermophoresis and swirling independently, the concentration factor could be boosted even higher. An optical conveyor for molecules by coupling thermophoresis and convection was realized [89], but it can only process sample in a fixed volume, and the speed is compromised as the laser needs to scan all the sample area. Attempts have also been made to couple thermophoresis with laminar flow for thermal field flow fractionation (TFFF), which is commercially utilized for composition analysis of polymers and colloids [168,178–186]. Relying on the parabolic profile to sort particles in different streams, TFFF requires a plug sample to prevent different species from overlapping axially, thus is usually used for analytical purposes. It is impractical to collect sample afterwards and the concentration factor is orders of magnitude lower. More recently, people are trying to focus nanoparticles in a thermodiffusion column continuously [187]. As flow rate needs to be very low, this method has low throughput. Also, the natural convection could not be controlled independently. Our device shows order of magnitude higher throughput, better concentration factor, and thus is more advantageous.

In this simulation, the concentrating effect of nanoparticles in a microfluidic channel by coupling thermophoresis and artificial swirling is studied by simulation. The physics behind this phenomena is revealed to be the competition and coupling between these two fluxes, and the dimensionless analysis also provides a guidance for designing the microfluidic channel to achieve the theoretical maximum. Next, experiments were guided by simulation to focus nanoparticles.

Lab-on-a-chip technology is impacting a broad range of disciplines such as chemistry, biology and medicine. Despite a continuously growing tool set for micro total analysis, a general microfluidic solution for continuous, label-free enrichment of polymeric nanoparticles and vesicles are not yet available, due to strong Brownian motion of nanospecies in a solution. Recent research of thermophoresis in aqueous solutions

indicates that thermophoretic force can overcome Brownian force to direct nanoparticle movement in a biocompatible environment. Coupling thermophoresis with natural convection on the microscale has been shown to induce significant enrichment of biomolecules in a closed capillary called a thermal diffusion column, yet the column has many practical limitations for separation applications. Here, we present a microfluidic device that couples an engineered helical flow and a mild, one-dimensional temperature gradient to achieve effective nanoparticle focusing in a continuous flow. Focusing of 100nm polystyrene particles are observed through confocal microscopy and the steady-state accumulation factor is dependent on the microgroove geometry and flow rates. Through numerical analysis of different transport processes within the channel, it is found that matched thermophoretic and convective fluxes lead to maximum concentration factor for a given temperature gradient. As thermophoresis is ubiquitous in fluids, the approach applies universally to suspended soft nanoparticles without the need of labeling and allows continuous retrieval of concentrated species in a simple flow through process. The microfluidic solution to nanoparticle focusing opens a new avenue to their analysis in resource limited settings.

Nanoparticle enrichment is a key pretreatment step in many applications. Microparticles focusing is achieved recently by utilizing its inertial properties. However, fast Brownian motion presents a main obstacle to efficient nanoparticle focusing. Different external field has been applied to focus nanoparticles, like fluid flow field, electromagnetic field, concentration gradient field, and temperature gradient field. Most recently, the temperature field driven nanoparticles focusing has attracted a lot of attention, as the temperature gradient caused thermophoresis does not scale with particle size significantly, hence provides a strong force on nanoparticles unlike other forces. Also, it's universal in nature and biocompatible. Nevertheless, temperature gradient could not

be infinitely high, and thermophoresis alone can only focus nanoparticles a couple times with a reasonable temperature gradient. Engineers have tackled this problem 80 years ago by using a thermal diffusion column. Most of recent work for nanoparticles focusing are based on this, in which the same temperature gradient introduce both thermophoresis and natural convection. This has an intrinsic problem that thermophoresis and convection could not be controlled independently, resulting in a compromised focusing effect. Also, it is a batch process and concentrated sample is hard to retrieve. In this paper, our study of nanoparticles focusing by coupling thermophoresis and convection shows a higher concentration effect in a label free and continuous flow fashion. Furthermore, the physics revealed in our previous simulation is confirmed by experiment here.

PDMS microfluidic devices were fabricated using the standard soft lithography technique. First, two layer SU-8 photoresist was patterned on a silicon wafer by photolithography to form a negative mold. Next, a 10:1 mixture of poly(dimethylsiloxane) (PDMS) prepolymer and curing agent was spin-coated onto the wafer and baked at 60 °C until cured. After cutting and removing the PDMS channel from the SU-8 mold, the thin layer of PDMS channel was sandwiched and bonded permanently through oxygen plasma between two cover glass slides. One of the cover glass was laser-cut with holes serving as inlet and outlet. PDMS blocks were bonded to the holes on cover glass for tubing handling.

After microfluidic channel fabrication, a temperature gradient was established by attaching the channel with a brass tube with cold water running inside. A thin film of silver-filled thermal conducting epoxy was used to enhance the thermal conductivity between the channel and brass tube. The other side of the sandwiched device was exposed to room temperature at around 28 °C with humidity controlled around 30%. The

temperature gradient was measured and confirmed by using a temperature sensitive dye BCECF (2', 7'-Bis-(2-Carboxyethyl)-5-(and-6)-Carboxyfluorescein) at 1 mM in DI water and by heat transfer simulation.

To demonstrate the principle of nanoparticles focusing by coupling thermophoresis and swirling, suspension containing 100 nm polystyrene nanoparticles at 1% or 0.03% (v/v) was introduced into the channel using a syringe pump. Scanning laser fluorescent confocal microscope was used for particle concentration measurement, and NanoDrop was utilized to measure the nanoparticles concentration.

To understand the transport processes that control nanoparticle accumulation, numerical analysis was performed by continuous phase model. The governing equations to describe natural convection are Boussinesq approximation and the mass conservation equation:

$$\frac{\partial \boldsymbol{u}}{\partial t} + \boldsymbol{u} \cdot \nabla \boldsymbol{u} = -\frac{1}{\rho}\nabla p + \gamma \nabla^2 \boldsymbol{u} + \alpha \boldsymbol{g}(T - T_0)$$

$$\nabla \cdot (\rho \boldsymbol{u}) = 0$$

where ρ is the fluid density, γ is the kinematic viscosity, t is the time, $\boldsymbol{u}$ is the fluid velocity, p is the pressure, α is the thermal expansion coefficient of the fluid, $\boldsymbol{g}$ is the gravitational acceleration and T is the temperature.

The conservation of energy is in the form

$$\rho C_p \frac{\partial T}{\partial t} + \rho C_p \boldsymbol{u} \cdot \nabla T = \nabla \cdot (k \nabla T)$$

where C_p is the heat capacity of the fluid and k is the thermal conductivity of the fluid.

The mass transport equation includes the mass diffusion, advection and the effect of the thermophoresis:

$$\frac{\partial c}{\partial t} = \nabla \cdot (D_T c \nabla T + D \nabla c) - \nabla \cdot (\boldsymbol{u} c)$$

where c is the concentration of the species.

The continuous phase model was implemented using COMSOL (Burlington, MA). The transport of species model was modified to include the thermophoretic flux term $D_T c \nabla T$ and solved together with laminar flow and heat transfer models. The channel is designed to have grooves on the bottom wall, and a temperature gradient is established as the temperature on top and bottom wall differs.

The proposed design is inspired by molecular enrichment in a thermal diffusion column [24,25], where a one dimensional temperature gradient across a thin gap is coupled with a natural convection roll in the gap (Fig. 53a). Solute molecules or suspended nanoparticles are transported through three processes: thermophoretic flux that drives species to either the cold (thermophobic) or warm wall (thermophilic), flux from natural convection that sweeps species to a low shear corner, and diffusive flux that transports species out of the corner. At the steady state, concentration in the accumulation zone decays exponentially to the bulk (Fig. 53a), and the concentration factor increases exponentially with the product of Soret coefficient, temperature difference across the gap and aspect ratio of the gap [86].

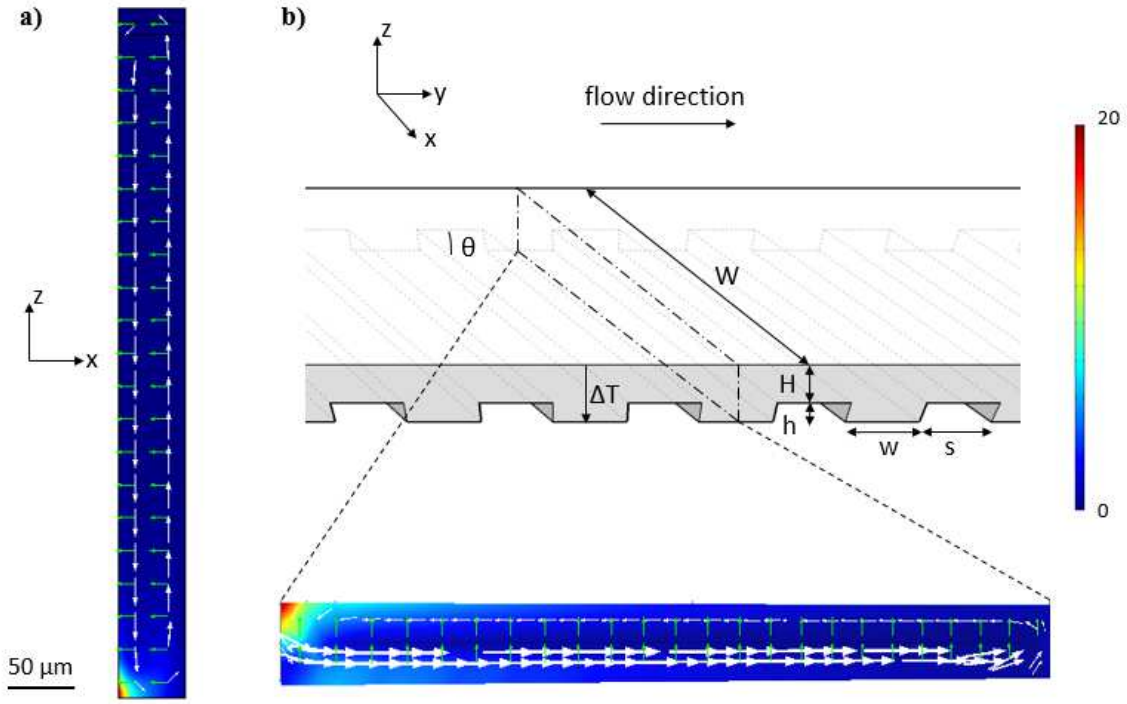

Figure 53 Nanoparticles focusing by coupling thermophoresis and secondary flow in a) a thermal diffusion column and b) in a microfluidic channel. In both figures, white arrows show the secondary flow velocity and green ones show thermophoretic velocity. The concentration contours demonstrate the focusing effect in 2D and 3D.

While a thermal diffusion column faces the challenge of batch processing and difficulty to retrieve the samples, we propose to couple an engineered 3D helical transport with a one dimensional temperature gradient in a microfluidic channel such that combined swirling and thermophoretic transport are created in the transverse plane (Fig. 53b). Numerical analysis shows that nanoparticles focus to one corner continuously. The focusing effect develops along the axial flow until a steady state is reached. The concentrated species can be retrieved continuously from a strategically positioned outlet, opposed to batch processing in thermal diffusion column. Since thermo-migration is intrinsic to all solvated species, no labeling is required and particles remain suspended in the focusing process. This avoids aggregation associated with pelleting in centrifugation and caking in ultracentrifugation, both of which contribute to variable yields. Furthermore, the throughput

is controllable by optimizing the device geometry, operation conditions and channel parallelization.

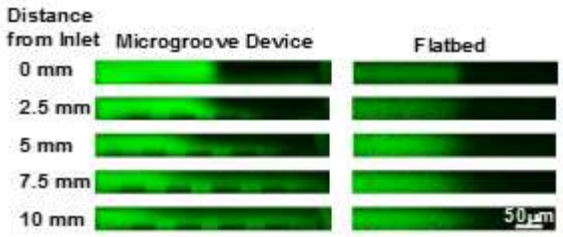

Figure 54 Grooves induced mixing

Three dimensional helical transport is introduced by micropatterned slanted grooves, structures often used for chaotic mixing [113,171–173], and the transverse velocity is controlled by the groove geometry (data not shown). While most literature uses a groove aspect ratio of 1, numerical analysis supports gentle secondary flow introduced by shallow grooves. To demonstrate experimentally that shallow grooves on the floor introduce transverse convection as a subcomponent of the axial flow, a solution of fluorescein and water are injected into the microchannel side by side at a mean axial velocity of 1 mm/s. The main channel width (W) is 500 µm, height (H) is 50 µm, groove width (w) is 50 µm, height (h) is 10 µm, spacing (s) is 50 µm and tilting angle (θ) is 45°. Compared to a channel with smooth floors and operated under the same axial velocity, fluorescein in the groove device shows significant lateral migration from confocal images (Fig. 54). The mean transverse velocity is measured to be ~30µm/s, matching the prediction from simulation for the selected structure.

A temperature gradient is superposed on the helical flow by sandwiching the PDMS thin channel between two coverslips and attaching a cooling pipe to the roof (Fig. 55). A 50/50 mixture of ethylene glycol and water at a controlled temperature of 0 °C to -12 °C is circulated in the cooling pipe. Bottom of the assembly is warmed up by air, where room temperature and humidity are controlled at 28 °C and 30% respectively. Fig. 56a-b

show one example of vertical temperature measurement by both finite element analysis and experimental measurements (Fig. 56). A temperature sensitive dye BCECF is used in the latter case, whose fluorescence intensity increases by 1.6% with each degree of temperature decrease [73,147,174]. Both analyses indicate an average temperature of ~ 277 K in the channel and a mild temperature difference of 1K between the ceiling and floor. Temperature difference is adjustable through coolant of different temperatures.

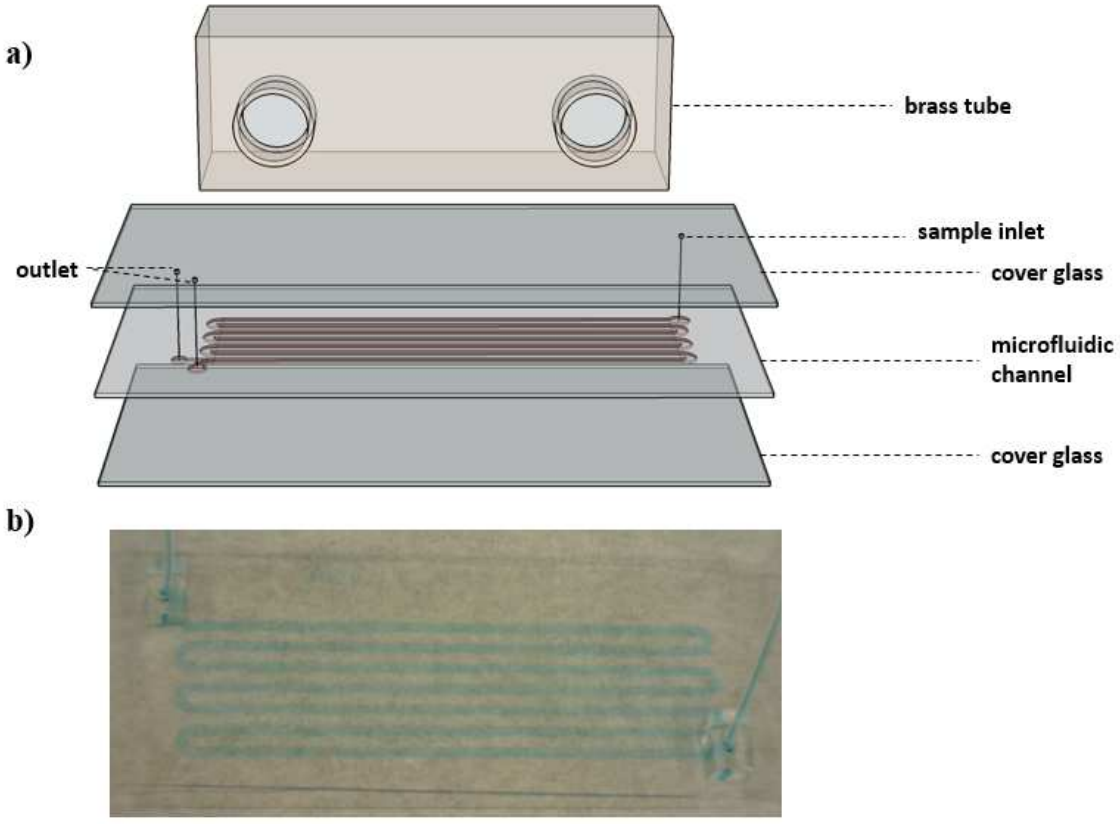

Figure 55 (a) Schematic of the device assembly and (b) photograph of an assembled device.

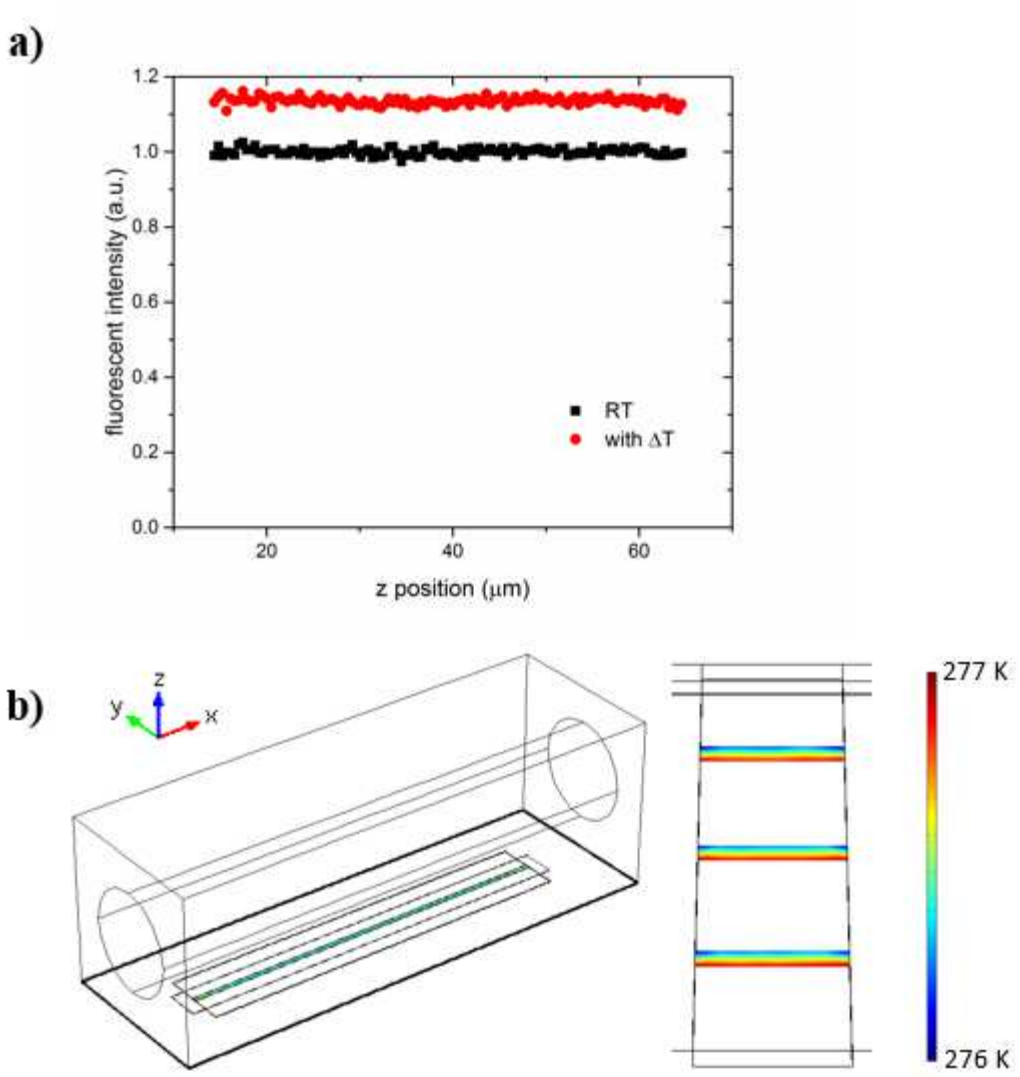

Figure 56 a) Fluorescent intensity in the vertical direction measured by BCECF. b) Temperature gradient in the channel observed by COMSOL simulation. The cooling pipe and room temperature is -12 °C and 28 °C respectively.

Under minute temperature gradients of 0.02K/μm and without any flow, preferential accumulation of nanoparticles is observed near the floor, and the accumulation becomes more evident when the coolant temperature is reduced from 273 K to 261 K (Fig. 57a-b). Maximum enrichment of 2 is observed when the coolant temperature is 261 K, corresponding to a temperature gradient of 1 K. A uniform distribution is observed when the coolant is left to warm to room temperature. Exponential decay of the concentration in the z-direction matches theoretical prediction with a one dimensional temperature

gradient present. Using temperature profiles shown in Fig. 56, the thermophoretic coefficient of 100 nm polystyrene particles is found to be increase with decreasing temperature, consistent with values from the literature [27,79]. As a reference, Soret coefficient of the same particles drop to 0.18 K^{-1} at room temperature from our prior measurements. The dramatic increase of Soret coefficients with a decrease of temperature near the water freezing point has been attributed to the change of water hydration entropy. Dampened diffusivity at lower temperature also promote nanoparticle accumulation. Furthermore, lower temperature near 0 °C protects native conformation and function of biological molecules and particles. All these factors support selection of a working temperature near 0°C.

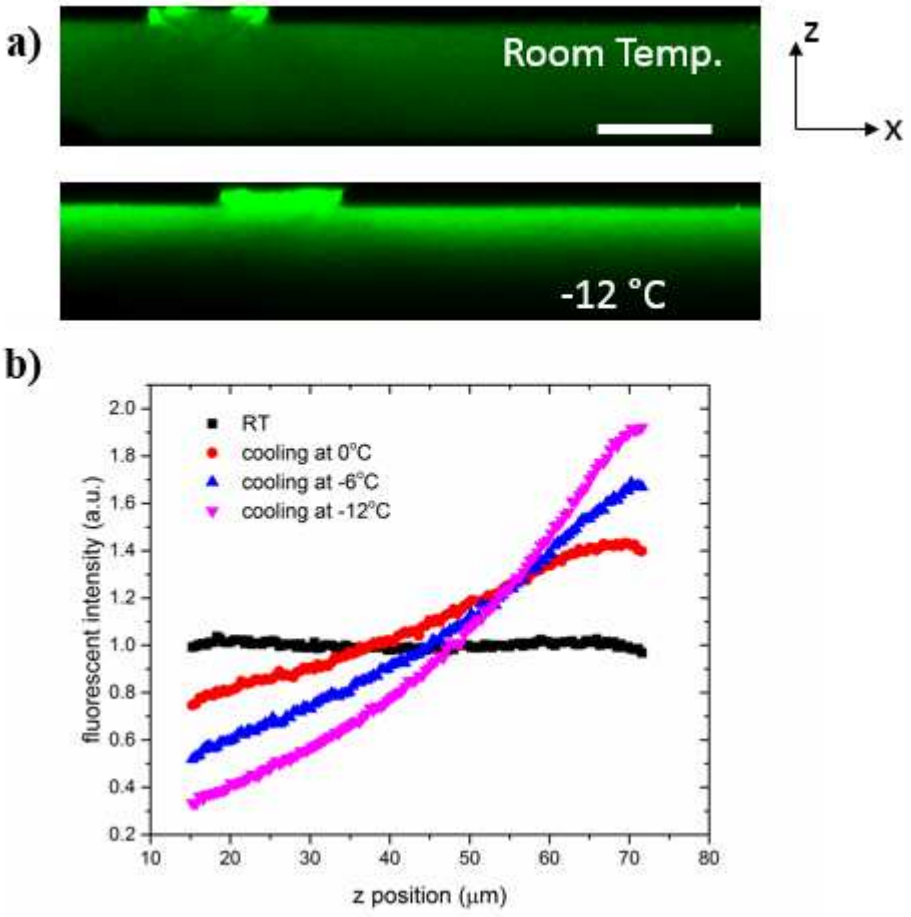

Figure 57 1D thermophoresis in the channel. a) confocal fluorescent image of the nanoparticles b) intensity profile in z direction with or without temperature gradient

Nanoparticle focusing in the lateral direction is achieved by coupling thermophoresis with an engineered helical flow. Swirling in the transverse plane sweeps the concentrated species on the floor to a corner and the concentration factor develops along an axial flow (Fig. 58a). Steady-state nanoparticle distribution in the x-z planes are shown in Fig. 58b, acquired by fluorescence confocal microscopy. Due to a channel aspect ratio of 1:20, only images from the two sides are shown here. The averaged vertical fluorescent intensity profile was analysis (Fig. 58c). At room temperature, the fluorescent intensity is uniform and low (Fig. 58c). With fluid flow and temperature gradient, nanoparticles are focused to the left part of the cross section of the channel. The focusing effect is

dependent on the axial flow. As shown in Fig. 58c, an axial flow of 10 μm/s yields the highest concentration factor of ~10, calculated by comparing the intensity with a calibration curve.

To interpret the dependence of concentration factors on the axial flow rate, transport processes in the microchannel are inspected more carefully through numerical analysis. Swirling and thermophoretic fluxes are calculated for each of the flow conditions: the swirling flux is calculated by averaging the positive secondary flow flux in a period, and the thermophoretic flux is the product of thermophoretic velocity and cross sectional area. When the concentration factor is plotted against the ratio of the two fluxes, maximum concentration is observed for a ratio of 1. Alternatively, the flux ratios are controlled by device geometry, which is still under investigation.

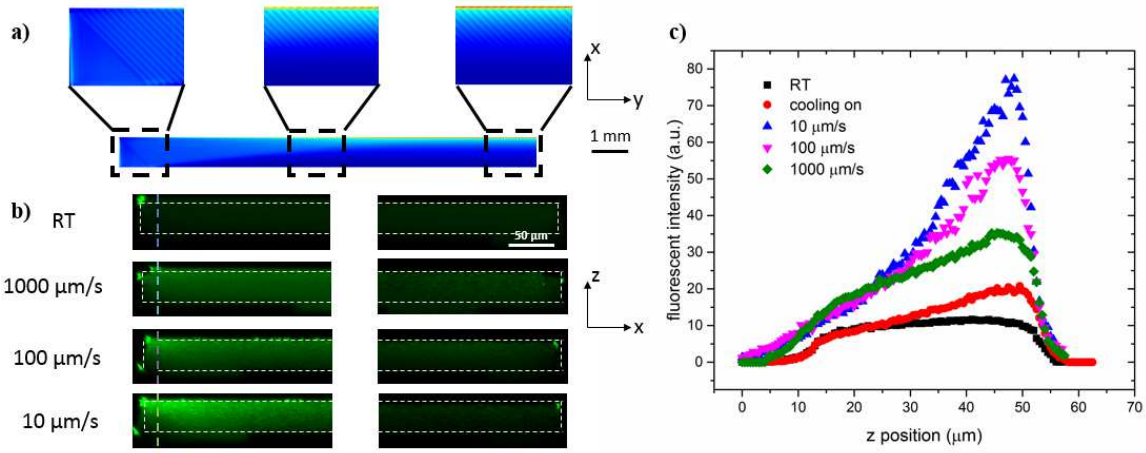

Figure 58 3D thermophoresis in the channel a) simulation showing focusing effect b) confocal fluorescent image of the nanoparticles c) intensity profile in z direction with or without temperature gradient

In this study, a novel method to focus nanoparticles is introduced by coupling thermophoresis and artificial lateral flow in microfluidics. It provides a way to pretreat nanoparticles more advanced than centrifuge.

3.3.3 Acknowledgements

Funding for the research was provided by National Institute of Health under Grant No. NIAID-1R21AI081638 and the U.S. Department of Defense, Defense Threat Reduction Agency under Contract HDTRA1-12-1-0007.

4 Conclusions and future directions

This research aims to provide a more accurate way to predict the migration of nanoparticles by gravity or thermophoresis. The thermal diffusion coefficient of biological particles like HIV virus was measured under different conditions, and the thermodynamic interaction near the viral particle surface could be better understood. By coupling thermophoresis with controlled secondary flow in microfluidics, we provided a practical way to focusing and separating nanoparticles continuously.

5 References

1. Whitesides GM. The origins and the future of microfluidics. *Nature*. 2006;442(7101):368-373. doi:10.1038/nature05058.

2. Di Carlo D, Irimia D, Tompkins RG, Toner M. Continuous inertial focusing, ordering, and separation of particles in microchannels. *Proc Natl Acad Sci*. 2007;104(48):18892-18897. doi:10.1073/pnas.0704958104.

3. Di Carlo D, Edd J, Humphry K, Stone H, Toner M. Particle Segregation and Dynamics in Confined Flows. *Phys Rev Lett*. 2009;102(9). doi:10.1103/PhysRevLett.102.094503.

4. Di Carlo D. Inertial microfluidics. *Lab Chip*. 2009;9(21):3038. doi:10.1039/b912547g.

5. Park J-S, Song S-H, Jung H-I. Continuous focusing of microparticles using inertial lift force and vorticity via multi-orifice microfluidic channels. *Lab Chip*. 2009;9(7):939. doi:10.1039/b813952k.

6. Amini H, Sollier E, Weaver WM, Di Carlo D. Intrinsic particle-induced lateral transport in microchannels. *Proc Natl Acad Sci U S A*. 2012;109(29):11593-11598. doi:10.1073/pnas.1207550109.

7. Yoon DH, Ha JB, Bahk YK, Arakawa T, Shoji S, Go JS. Size-selective separation of micro beads by utilizing secondary flow in a curved rectangular microchannel. *Lab Chip*. 2009;9(1):87-90. doi:10.1039/b809123d.

8. Stan CA, Ellerbee AK, Guglielmini L, Stone HA, Whitesides GM. The magnitude of lift forces acting on drops and bubbles in liquids flowing inside microchannels. *Lab Chip*. 2013;13(3):365-376. doi:10.1039/c2lc41035d.

9. Hur SC, Tse HT, Di Carlo D. Sheathless inertial cell ordering for extreme throughput flow cytometry. *Lab Chip*. 2010;10(3):274-280. doi:10.1039/b919495a.

10. Hur SC, Henderson-MacLennan NK, McCabe ER, Di Carlo D. Deformability-based cell classification and enrichment using inertial microfluidics. *Lab Chip*. 2011;11(5):912-920. doi:10.1039/c0lc00595a.

11. Sun M, Khan ZS, Vanapalli SA. Blood plasma separation in a long two-phase plug flowing through disposable tubing. *Lab Chip*. 2012. doi:10.1039/c2lc40544j.

12. Wu L, Guan G, Hou HW, Bhagat AA, Han J. Separation of leukocytes from blood using spiral channel with trapezoid cross-section. *Anal Chem*. 2012;84(21):9324-9331. doi:10.1021/ac302085y.

13. Wu Z, Willing B, Bjerketorp J, Jansson JK, Hjort K. Soft inertial microfluidics for high throughput separation of bacteria from human blood cells. *Lab Chip*. 2009;9(9):1193. doi:10.1039/b817611f.

14. Bhagat AA, Hou HW, Li LD, Lim CT, Han J. Pinched flow coupled shear-modulated inertial microfluidics for high-throughput rare blood cell separation. *Lab Chip*. 2011;11(11):1870-1878. doi:10.1039/c0lc00633e.

15. Hermanson KD, Lumsdon SO, Williams JP, Kaler EW, Velev OD. Dielectrophoretic assembly of electrically functional microwires from nanoparticle suspensions. *Science (80-)*. 2001;294(5544):1082-1086. doi:10.1126/science.1063821.

16. Zhao C, Cheng XH. Microfluidic separation of viruses from blood cells based on intrinsic transport processes. *Biomicrofluidics*. 2011;5(3). doi:10.1063/1.3609262.

17. Irimajiri A, Hanai T, Inouye A. DIELECTRIC THEORY OF MULTI-STRATIFIED SHELL-MODEL WITH ITS APPLICATION TO A LYMPHOMA CELL. *J Theor Biol*. 1979;78(2):251-269. doi:10.1016/0022-5193(79)90268-6.

18. Gagnon ZR. Cellular dielectrophoresis: applications to the characterization, manipulation, separation and patterning of cells. *Electrophoresis*. 2011;32(18):2466-2487. doi:10.1002/elps.201100060.

19. McCauley MJ, Williams MC. Mechanisms of DNA binding determined in optical tweezers experiments. *Biopolymers*. 2007;85(2):154-168. doi:10.1002/bip.20622.

20. Huang LR. Continuous Particle Separation Through Deterministic Lateral Displacement. *Science (80-)*. 2004;304(5673):987-990. doi:10.1126/science.1094567.

21. Lim J, Lanni C, Evarts ER, Lanni F, Tilton RD, Majetich SA. Magnetophoresis of Nanoparticles. *ACS Nano*. 2011;5(1):217-226. doi:10.1021/nn102383s.

22. Chen GD, Alberts CJ, Rodriguez W, Toner M. Concentration and Purification of Human Immunodeficiency Virus Type 1 Virions by Microfluidic Separation of Superparamagnetic Nanoparticles. *Anal Chem*. 2010;82(2):723-728. doi:10.1021/ac9024522.

23. Abecassis B, Cottin-Bizonne C, Ybert C, Ajdari A, Bocquet L. Boosting migration of large particles by solute contrasts. *Nat Mater*. 2008;7(10):785-789. doi:10.1038/nmat2254.

24. Debye P. Zur Theorie des Clusiusschen Trennungsverfahrens. *Ann Phys*. 1939;428(3-4). doi:10.1002/andp.19394280310.

25. Furry W, Jones R, Onsager L. On the Theory of Isotope Separation by Thermal Diffusion. *Phys Rev*. 1939;55(11):1083-1095. doi:10.1103/PhysRev.55.1083.

26. Piazza R, Parola A. Thermophoresis in colloidal suspensions. *J Phys Condens Matter*. 2008;20(15):153102. doi:10.1088/0953-8984/20/15/153102.

27. Putnam SA, Cahill DG, Wong GCL. Temperature dependence of thermodiffusion in aqueous suspensions of charged nanoparticles. *Langmuir*. 2007;23(18):9221-9228. doi:10.1021/la700489e.

28. Wong AP, Gupta M, Shevkoplyas SS, Whitesides GM. Egg beater as centrifuge: isolating human blood plasma from whole blood in resource-poor settings. *Lab Chip*. 2008;8(12):2032-2037. doi:10.1039/b809830c.

29. Cho Y-K, Lee J-G, Park J-M, Lee B-S, Lee Y, Ko C. One-step pathogen specific DNA extraction from whole blood on a centrifugal microfluidic device. *Lab Chip*. 2007;7(5):565-573. doi:10.1039/b616115d.

30. Zhang J, Guo Q, Liu M, Yang J. A lab-on-CD prototype for high-speed blood separation. *J Micromechanics Microengineering*. 2008;18(12):125025. doi:10.1088/0960-1317/18/12/125025.

31. Lee BS, Lee J-N, Park J-M, et al. A fully automated immunoassay from whole blood on a disc. *Lab Chip*. 2009;9(11):1548-1555. doi:10.1039/b820321k.

32. Crowley TA, Pizziconi V. Isolation of plasma from whole blood using planar microfilters for lab-on-a-chip applications. *Lab Chip*. 2005;5(9):922-929. doi:10.1039/b502930a.

33. VanDelinder V, Groisman A. Separation of plasma from whole human blood in a continuous cross-flow in a molded microfluidic device. *Anal Chem*. 2006;78(11):3765-3771. doi:10.1021/ac060042r.

34. Jäggi RD, Sandoz R, Effenhauser CS. Microfluidic depletion of red blood cells from whole blood in high-aspect-ratio microchannels. *Microfluid Nanofluidics*. 2006;3(1):47-53. doi:10.1007/s10404-006-0104-9.

35. Tachi T, Kaji N, Tokeshi M, Baba Y. Simultaneous separation, metering, and dilution of plasma from human whole blood in a microfluidic system. *Anal Chem*. 2009;81(8):3194-3198. doi:10.1021/ac802434z.

36. Chen X, Cui D, Chen J. Design, fabrication and characterization of nano-filters in silicon microfluidic channels based on MEMS technology. *Electrophoresis*. 2009;30(18):3168-3173. doi:10.1002/elps.200900068.

37. Thorslund S, Klett O, Nikolajeff F, Markides K, Bergquist J. A hybrid poly(dimethylsiloxane) microsystem for on-chip whole blood filtration optimized for steroid screening. *Biomed Microdevices*. 2006;8(1):73-79. doi:10.1007/s10544-006-6385-7.

38. Kersaudy-Kerhoas M, Kavanagh DM, Dhariwal RS, Campbell CJ, Desmulliez MP. Validation of a blood plasma separation system by biomarker detection. *Lab Chip*. 2010;10(12):1587-1595. doi:10.1039/b926834k.

39. Yang S, Undar A, Zahn JD. A microfluidic device for continuous, real time blood plasma separation. *Lab Chip*. 2006;6(7):871-880. doi:10.1039/b516401j.

40. Rodriguez-Villarreal AI, Arundell M, Carmona M, Samitier J. High flow rate microfluidic device for blood plasma separation using a range of temperatures. *Lab Chip*. 2010;10(2):211-219. doi:10.1039/b904531g.

41. Sollier E, Rostaing H, Pouteau P, Fouillet Y, Achard J-L. Passive microfluidic devices for plasma extraction from whole human blood. *Sensors Actuators B Chem*. 2009;141(2):617-624. doi:10.1016/j.snb.2009.05.023.

42. Davis JA, Inglis DW, Morton KJ, et al. Deterministic hydrodynamics: taking blood apart. *Proc Natl Acad Sci U S A*. 2006;103(40):14779-14784. doi:10.1073/pnas.0605967103.

43. Russom A, Gupta AK, Nagrath S, Di Carlo D, Edd JF, Toner M. Differential inertial focusing of particles in curved low-aspect-ratio microchannels. *New J Phys*. 2009;11:75025. doi:10.1088/1367-2630/11/7/075025.

44. Hsu C-H, Di Carlo D, Chen C, Irimia D, Toner M. Microvortex for focusing, guiding and sorting of particles. *Lab Chip*. 2008;8(12):2128. doi:10.1039/b813434k.

45. Chen H-H, Gao D. Particle enrichment employing grooved microfluidic channels. *Appl Phys Lett*. 2008;92(17):173502. doi:10.1063/1.2917794.

46. Arifin DR, Yeo LY, Friend JR. Microfluidic blood plasma separation via bulk electrohydrodynamic flows. *Biomicrofluidics*. 2007;1(1):14103. doi:10.1063/1.2409629.

47. Qu BY, Wu ZY, Fang F, Bai ZM, Yang DZ, Xu SK. A glass microfluidic chip for continuous blood cell sorting by a magnetic gradient without labeling. *Anal Bioanal Chem*. 2008;392(7-8):1317-1324. doi:10.1007/s00216-008-2382-4.

48. Nakashima Y, Hata S, Yasuda T. Blood plasma separation and extraction from a minute amount of blood using dielectrophoretic and capillary forces. *Sensors Actuators B Chem*. 2010;145(1):561-569. doi:10.1016/j.snb.2009.11.070.

49. Lien KY, Lin JL, Liu CY, Lei HY, Lee GB. Purification and enrichment of virus samples utilizing magnetic beads on a microfluidic system. *Lab Chip*. 2007;7(7):868-875. doi:10.1039/b700516d.

50. Chen GD, Alberts CJ, Rodriguez W, Toner M. Concentration and purification of human immunodeficiency virus type 1 virions by microfluidic separation of superparamagnetic nanoparticles. *Anal Chem*. 2010;82(2):723-728. doi:10.1021/ac9024522.

51. Huh D, Mills KL, Zhu X, Burns MA, Thouless MD, Takayama S. Tuneable elastomeric nanochannels for nanofluidic manipulation. *Nat Mater*. 2007;6(6):424-428. doi:10.1038/nmat1907.

52. Yamada M, Nakashima M, Seki M. Pinched flow fractionation: continuous size separation of particles utilizing a laminar flow profile in a pinched microchannel. *Anal Chem*. 2004;76(18):5465-5471. doi:10.1021/ac049863r.

53. Lin Y, Skaff H, Emrick T, Dinsmore AD, Russell TP. Nanoparticle assembly and transport at liquid-liquid interfaces. *Science*. 2003;299(5604):226-229. doi:10.1126/science.1078616.

54. Bresme F, Oettel M. Nanoparticles at fluid interfaces. *J Phys Condens Matter*. 2007;19(41):413101. doi:10.1088/0953-8984/19/41/413101.

55. Zhao J-J, Duan Y-Y, Wang X-D, Wang B-X. Effects of solid–gas coupling and pore and particle microstructures on the effective gaseous thermal conductivity in aerogels. *J Nanoparticle Res*. 2012;14(8):1024. doi:10.1007/s11051-012-1024-0.

56. Kamholz AE, Schilling EA, Yager P. Optical measurement of transverse molecular diffusion in a microchannel. *Biophys J*. 2001;80(4):1967-1972. doi:10.1016/S0006-3495(01)76166-8.

57. Kamholz AE, Yager P. Theoretical analysis of molecular diffusion in pressure-driven laminar flow in microfluidic channels. *Biophys J*. 2001;80(1):155-160. doi:10.1016/S0006-3495(01)76003-1.

58. Ismagilov RF, Stroock AD, Kenis PJA, Whitesides G, Stone HA. Experimental and theoretical scaling laws for transverse diffusive broadening in two-phase laminar flows in microchannels. *Appl Phys Lett*. 2000;76(17):2376. doi:10.1063/1.126351.

59. Hatch A, Kamholz AE, Hawkins KR, et al. A rapid diffusion immunoassay in a T-sensor. *Nat Biotechnol*. 2001;19(5):461-465. doi:10.1038/88135.

60. Stiles PJ, Fletcher DF. Effects of gravity on the steady state of a reaction in a liquid-state microreactor—deviations from Poiseuille flow. *Phys Chem Chem Phys*. 2003;5(6):1219-1224. doi:10.1039/b211686c.

61. Yoon SK, Mitchell M, Choban ER, Kenis PJ. Gravity-induced reorientation of the interface between two liquids of different densities flowing laminarly through a microchannel. *Lab Chip*. 2005;5(11):1259-1263. doi:10.1039/b508680a.

62. Yamaguchi Y, Honda T, Briones MP, et al. Influence of gravity on a laminar flow in a microbioanalysis system. *Meas Sci Technol*. 2006;17(12):3162-3166. doi:10.1088/0957-0233/17/12/s07.

63. Yamaguchi Y, Honda T, Briones MP, et al. Influence of Gravity on Two-Layer Laminar Flow in a Microchannel. *Chem Eng Technol*. 2007;30(3):379-382. doi:10.1002/ceat.200600326.

64. Xuan J, Leung MKH, Leung DYC, Ni M. Density-induced asymmetric pair of Dean vortices and its effects on mass transfer in a curved microchannel with two-layer laminar stream. *Chem Eng J*. 2011;171(1):216-223. doi:10.1016/j.cej.2011.01.011.

65. Yamaguchi Y, Takagi F, Watari T, et al. Interface configuration of the two layered laminar flow in a curved microchannel. *Chem Eng J*. 2004;101(1-3):367-372. doi:10.1016/j.cej.2003.10.018.

66. Ruckenstein E. Can phoretic motions be treated as interfacial-tension gradient driven phenomena. *J Colloid Interface Sci*. 1981;83(1):77-81. doi:10.1016/0021-9797(81)90011-4.

67. Morozov KI. Thermal diffusion in disperse systems. *J Exp Theor Phys*. 1999;88(5):944-946. doi:10.1134/1.558875.

68. Andreev AF. Thermophoresis in liquids. *Zhurnal Eksp I Teor Fiz*. 1988;94(1):210-216. <Go to ISI>://WOS:A1988M002500019.

69. Gaeta FS. Radiation pressure theory of thermal diffusion in liquids. *Phys Rev*. 1969;182(1):289 - &. doi:10.1103/PhysRev.182.289.

70. Semenov S, Schimpf M. Thermophoresis of dissolved molecules and polymers: Consideration of the temperature-induced macroscopic pressure gradient. *Phys Rev E*. 2004;69(1). doi:10.1103/PhysRevE.69.011201.

71. Anderson JL. Colloid transport by interfacial forces. *Annu Rev Fluid Mech*. 1989;21:61-99. doi:10.1146/annurev.fluid.21.1.61.

72. Bringuier E, Bourdon A. Colloid transport in nonuniform temperature. *Phys Rev E*. 2003;67(1). doi:10.1103/PhysRevE.67.011404.

73. Duhr S, Braun D. Why molecules move along a temperature gradient. *Proc Natl Acad Sci U S A*. 2006;103(52):19678-19682. doi:10.1073/pnas.0603873103.

74. Srinivasan S, Saghir MZ. Experimental approaches to study thermodiffusion - A review. *Int J Therm Sci*. 2011;50(7):1125-1137. doi:10.1016/j.ijthermalsci.2011.02.022.

75. Piazza R. Thermal forces : colloids in temperature gradients. *J Phys Condens Matter*. 2004;16(38):S4195-S4211. doi:10.1088/0953-8984/16/38/032.

76. Duhr S, Arduini S, Braun D. Thermophoresis of DNA determined by microfluidic fluorescence. *Eur Phys J E Soft Matter*. 2004;15(3):277-286. doi:10.1140/epje/i2004-10073-5.

77. Jiang H-R, Wada H, Yoshinaga N, Sano M. Manipulation of Colloids by a Nonequilibrium Depletion Force in a Temperature Gradient. *Phys Rev Lett*. 2009;102(20). doi:10.1103/PhysRevLett.102.208301.

78. Vigolo D, Rusconi R, Stone HA, Piazza R. Thermophoresis: microfluidics characterization and separation. *Soft Matter*. 2010;6(15):3489. doi:10.1039/c002057e.

79. Braibanti M, Vigolo D, Piazza R. Does Thermophoretic Mobility Depend on Particle Size? *Phys Rev Lett*. 2008;100(10). doi:10.1103/PhysRevLett.100.108303.

80. Piazza R, Guarino A. Soret Effect in Interacting Micellar Solutions. *Phys Rev Lett*. 2002;88(20). doi:10.1103/PhysRevLett.88.208302.

81. Iacopini S, Rusconi R, Piazza R. The “macromolecular tourist”: universal temperature dependence of thermal diffusion in aqueous colloidal suspensions. *Eur Phys J E Soft Matter*. 2006;19(1):59-67. doi:10.1140/epje/e2006-00012-9.

82. Maeda Y, Buguin A, Libchaber A. Thermal Separation: Interplay between the Soret Effect and Entropic Force Gradient. *Phys Rev Lett*. 2011;107(3). doi:10.1103/PhysRevLett.107.038301.

83. Würger A. Transport in Charged Colloids Driven by Thermoelectricity. *Phys Rev Lett*. 2008;101(10). doi:10.1103/PhysRevLett.101.108302.

84. Braun D, Libchaber A. Trapping of DNA by Thermophoretic Depletion and Convection. *Phys Rev Lett*. 2002;89(18). doi:10.1103/PhysRevLett.89.188103.

85. Reineck P, Wienken CJ, Braun D. Thermophoresis of single stranded DNA. *Electrophoresis*. 2010;31(2):279-286. doi:10.1002/elps.200900505.

86. Baaske P, Weinert FM, Duhr S, Lemke KH, Russell MJ, Braun D. Extreme accumulation of nucleotides in simulated hydrothermal pore systems. *Proc Natl Acad Sci U S A*. 2007;104(22):9346-9351. doi:10.1073/pnas.0609592104.

87. Mast CB, Braun D. Thermal Trap for DNA Replication. *Phys Rev Lett*. 2010;104(18). doi:10.1103/PhysRevLett.104.188102.

88. Budin I, Bruckner RJ, Szostak JW. Formation of Protocell-like Vesicles in a Thermal Diffusion Column. *J Am Chem Soc*. 2009;131(28):9628-9629. doi:10.1021/ja9029818.

89. Weinert FM, Braun D. An Optical Conveyor for Molecules. *Nano Lett*. 2009;9(12):4264-4267. doi:10.1021/nl902503c.

90. Astumian RD. Coupled transport at the nanoscale: the unreasonable effectiveness of equilibrium theory. *Proc Natl Acad Sci U S A*. 2007;104(1):3-4. doi:10.1073/pnas.0609754104.

91. Wienken CJ, Baaske P, Rothbauer U, Braun D, Duhr S. Protein-binding assays in biological liquids using microscale thermophoresis. *Nat Commun*. 2010;1:100. doi:10.1038/ncomms1093.

92. Jiang H-R, Yoshinaga N, Sano M. Active Motion of a Janus Particle by Self-Thermophoresis in a Defocused Laser Beam. *Phys Rev Lett*. 2010;105(26). doi:10.1103/PhysRevLett.105.268302.

93. Duhr S, Braun D. Optothermal Molecule Trapping by Opposing Fluid Flow with Thermophoretic Drift. *Phys Rev Lett*. 2006;97(3). doi:10.1103/PhysRevLett.97.038103.

94. Mast CB, Schink S, Gerland U, Braun D. Escalation of polymerization in a thermal gradient. *Proc Natl Acad Sci U S A*. 2013;110(20):8030-8035. doi:10.1073/pnas.1303222110.

95. Mao HB, Yang TL, Cremer PS. A microfluidic device with a linear temperature gradient for parallel and combinatorial measurements. *J Am Chem Soc*. 2002;124(16):4432-4435. doi:10.1021/ja017625x.

96. Chen P-C, Fan W, Hoo T-K, Chan LCZ, Wang Z. Simulation guided-design of a microfluidic thermal reactor for polymerase chain reaction. *Chem Eng Res Des*. 2012;90(5):591-599. doi:10.1016/j.cherd.2011.09.008.

97. Watzig H. THE MEASUREMENT OF TEMPERATURE INSIDE CAPILLARIES FOR ELECTROPHORESIS USING THERMOCHROMIC SOLUTIONS. *Chromatographia*. 1992;33(9-10):445-448. doi:10.1007/bf02262325.

98. Chaudhari AM, Woudenberg TM, Albin M, Goodson KE. Transient liquid crystal thermometry of microfabricated PCR vessel arrays. *J Microelectromechanical Syst*. 1998;7(4):345-355. doi:10.1109/84.735341.

99. Lacey ME, Webb AG, Sweedler J V. Monitoring temperature changes in capillary electrophoresis with nanoliter-volume NMR thermometry. *Anal Chem*. 2000;72(20):4991-4998. doi:10.1021/ac000649m.

100. Liu KLK, Davis KL, Morris MD. RAMAN-SPECTROSCOPIC MEASUREMENT OF SPATIAL AND TEMPORAL TEMPERATURE-GRADIENTS IN OPERATING ELECTROPHORESIS CAPILLARIES. *Anal Chem*. 1994;66(21):3744-3750. doi:10.1021/ac00093a033.

101. Ross D, Gaitan M, Locascio LE. Temperature measurement in microfluidic systems using a temperature-dependent fluorescent dye. *Anal Chem*. 2001;73(17):4117-4123. doi:10.1021/ac010370l.

102. Miyauchi K, Kim Y, Latinovic O, Morozov V, Melikyan GB. HIV enters cells via endocytosis and dynamin-dependent fusion with endosomes. *Cell*. 2009;137(3):433-444. doi:10.1016/j.cell.2009.02.046.

103. Human Immunodeficiency Virus (HIV). *Transfus Med Hemotherapy*. 2005;32(3-4):196-208. doi:10.1159/000087620.

104. Cabrales P, Tsai AG, Winslow RM, Intaglietta M. Extreme hemodilution with PEG-hemoglobin vs. PEG-albumin. *Am J Physiol Heart Circ Physiol*. 2005;289(6):H2392-H2400. doi:10.1152/ajpheart.00225.2005.

105. Zhang X, Davis RH. The rate of collisions due to Brownian or gravitational motion of small drops. *J Fluid Mech*. 2006;230(-1):479. doi:10.1017/S0022112091000861.

106. Chien S. Shear dependence of effective cell volume as a determinant of blood viscosity. *Science*. 1970;168(3934):977-979. http://www.ncbi.nlm.nih.gov/pubmed/5441028. Accessed March 3, 2015.

107. Kang YJ, Yoon SY, Lee K-H, Yang S. A highly accurate and consistent microfluidic viscometer for continuous blood viscosity measurement. *Artif Organs*. 2010;34(11):944-949. doi:10.1111/j.1525-1594.2010.01078.x.

108. Masoumi N, Sohrabi N, Behzadmehr A. A new model for calculating the effective viscosity of nanofluids. *J Phys D Appl Phys*. 2009;42(5):055501. doi:10.1088/0022-3727/42/5/055501.

109. Drew DA. MATHEMATICAL-MODELING OF 2-PHASE FLOW. *Annu Rev Fluid Mech*. 1983;15:261-291. doi:10.1146/annurev.fl.15.010183.001401.

110. Zhang DZ, Prosperetti A. Momentum and energy equations for disperse two-phase flows and their closure for dilute suspensions. *Int J Multiph Flow*. 1997;23(3):425-453. doi:10.1016/S0301-9322(96)00080-8.

111. Li A, Ahmadi G. Dispersion and Deposition of Spherical Particles from Point Sources in a Turbulent Channel Flow. *Aerosol Sci Technol*. 1992;16(4):209-226. doi:10.1080/02786829208959550.

112. Saffman PG. The lift on a small sphere in a slow shear flow. *J Fluid Mech*. 1965;22:385. doi:10.1017/S0022112065000824.

113. Stroock AD. Chaotic Mixer for Microchannels. *Science (80-)*. 2002;295(5555):647-651. doi:10.1126/science.1066238.

114. Grzelczak M, Vermant J, Furst EM, Liz-Marzán LM. Directed self-assembly of nanoparticles. *ACS Nano*. 2010;4(7):3591-3605. doi:10.1021/nn100869j.

115. Van den Bogaart G, Thutupalli S, Risselada JH, et al. Synaptotagmin-1 may be a distance regulator acting upstream of SNARE nucleation. *Nat Struct Mol Biol*. 2011;18(7):805-812. doi:10.1038/nsmb.2061.

116. Putnam SA, Cahill DG. Transport of nanoscale latex spheres in a temperature gradient. *Langmuir*. 2005;21(12):5317-5323.

117. Blanco P, Kriegs H, Lettinga MP, Holmqvist P, Wiegand S. Thermal diffusion of a stiff rod-like mutant Y21M fd-virus. *Biomacromolecules*. 2011;12(5):1602-1609. doi:10.1021/bm2000023.

118. Zhao C, Oztekin A, Cheng X. Measuring the thermal diffusion coefficients of artificial and biological particles in a microfluidic chip. *Bull Am Phys Soc*. 2013;Volume 58,. http://meetings.aps.org/link/BAPS.2013.DFD.D6.2. Accessed July 9, 2014.

119. Zheng F. Thermophoresis of spherical and non-spherical particles: a review of theories and experiments. *Adv Colloid Interface Sci*. 2002;97(1-3):255-278. doi:10.1016/S0001-8686(01)00067-7.

120. Seidel S a I, Dijkman PM, Lea W a, et al. Microscale thermophoresis quantifies biomolecular interactions under previously challenging conditions. *Methods*. 2013;59(3):301-315. doi:10.1016/j.ymeth.2012.12.005.

121. Jerabek-Willemsen M, Wienken CJ, Braun D, Baaske P, Duhr S. Molecular interaction studies using microscale thermophoresis. *Assay Drug Dev Technol*. 2011;9(4):342-353. doi:10.1089/adt.2011.0380.

122. Garner MM, Revzin A. A gel electrophoresis method for quantifying the binding of proteins to specific DNA regions: application to components of the Escherichia coli lactose operon regulatory system. *Nucleic Acids Res*. 1981;9(13):3047-3060. doi:10.1093/nar/9.13.3047.

123. Hellman LM, Fried MG. Electrophoretic mobility shift assay (EMSA) for detecting protein-nucleic acid interactions. *Nat Protoc*. 2007;2(8):1849-1861. doi:10.1038/nprot.2007.249.

124. Engvall E, Perlmann P. Enzyme-linked immunosorbent assay (ELISA). Quantitative assay of immunoglobulin G. *Immunochemistry*. 1971;8(9):871-874. http://www.ncbi.nlm.nih.gov/pubmed/5135623. Accessed July 7, 2014.

125. Ladbury JE, Chowdhry BZ. Sensing the heat: the application of isothermal titration calorimetry to thermodynamic studies of biomolecular interactions. *Chem Biol*. 1996;3(10):791-801. doi:10.1016/S1074-5521(96)90063-0.

126. Leavitt S, Freire E. Direct measurement of protein binding energetics by isothermal titration calorimetry. *Curr Opin Struct Biol*. 2001;11(5):560-566. doi:10.1016/S0959-440X(00)00248-7.

127. Wiseman T, Williston S, Brandts JF, Lin L-N. Rapid measurement of binding constants and heats of binding using a new titration calorimeter. *Anal Biochem*. 1989;179(1):131-137. doi:10.1016/0003-2697(89)90213-3.

128. Fujime S, Ishiwata S. Dynamic study of F-actin by quasielastic scattering of laser light. *J Mol Biol*. 1971;62(1):251-265. doi:10.1016/0022-2836(71)90144-6.

129. Hanlon AD, Larkin MI, Reddick RM. Free-solution, label-free protein-protein interactions characterized by dynamic light scattering. *Biophys J*. 2010;98(2):297-304. doi:10.1016/j.bpj.2009.09.061.

130. Dandliker WB, Feigen GA. Quantification of the antigen-antibody reaction by the polarization of fluorescence. *Biochem Biophys Res Commun*. 1961;5(4):299-304. doi:10.1016/0006-291X(61)90167-X.

131. Lea WA, Simeonov A. Fluorescence polarization assays in small molecule screening. *Expert Opin Drug Discov*. 2011;6(1):17-32. doi:10.1517/17460441.2011.537322.

132. Baksh MM, Kussrow AK, Mileni M, Finn MG, Bornhop DJ. Label-free quantification of membrane-ligand interactions using backscattering interferometry. *Nat Biotechnol*. 2011;29(4):357-360. doi:10.1038/nbt.1790.

133. Nguyen B, Tanious FA, Wilson WD. Biosensor-surface plasmon resonance: quantitative analysis of small molecule-nucleic acid interactions. *Methods*. 2007;42(2):150-161. doi:10.1016/j.ymeth.2006.09.009.

134. Schuck P. Use of surface plasmon resonance to probe the equilibrium and dynamic aspects of interactions between biological macromolecules. *Annu Rev Biophys Biomol Struct*. 1997;26:541-566. doi:10.1146/annurev.biophys.26.1.541.

135. Gao Y, Xin Z, Zeng B, Gan Q, Cheng X, Bartoli FJ. Plasmonic interferometric sensor arrays for high-performance label-free biomolecular detection. *Lab Chip*. 2013;13(24):4755-4764. doi:10.1039/c3lc50863c.

136. Seidel SAI, Markwardt NA, Lanzmich SA, Braun D. Thermophoresis in Nanoliter Droplets to Quantify Aptamer Binding. *Angew Chem Int Ed Engl*. 2014. doi:10.1002/anie.201402514.

137. Bhogaraju S, Cajanek L, Fort C, et al. Molecular basis of tubulin transport within the cilium by IFT74 and IFT81. *Science*. 2013;341(6149):1009-1012. doi:10.1126/science.1240985.

138. Xiong X, Coombs PJ, Martin SR, et al. Receptor binding by a ferret-transmissible H5 avian influenza virus. *Nature*. 2013;497(7449):392-396. doi:10.1038/nature12144.

139. Gertz M, Fischer F, Nguyen GTT, et al. Ex-527 inhibits Sirtuins by exploiting their unique NAD+-dependent deacetylation mechanism. *Proc Natl Acad Sci U S A*. 2013;110(30):E2772-E2781. http://www.pubmedcentral.nih.gov/articlerender.fcgi?artid=3725051&tool=pmcentrez&rendertype=abstract.

140. Shang X, Marchioni F, Evelyn CR, et al. Small-molecule inhibitors targeting G-protein-coupled Rho guanine nucleotide exchange factors. *Proc Natl Acad Sci U S A*. 2013;110(8):3155-3160. doi:10.1073/pnas.1212324110.

141. Cherrier T, Le Douce V, Eilebrecht S, et al. CTIP2 is a negative regulator of P-TEFb. *Proc Natl Acad Sci U S A*. 2013;110(31):12655-12660. doi:10.1073/pnas.1220136110.

142. Baaske P, Wienken CJ, Reineck P, Duhr S, Braun D. Optical thermophoresis for quantifying the buffer dependence of aptamer binding. *Angew Chemie*. 2010;49(12):2238-2241. doi:10.1002/anie.200903998.

143. Seidel SA, Wienken CJ, Geissler S, et al. Label-free microscale thermophoresis discriminates sites and affinity of protein-ligand binding. *Angew Chemie*. 2012;51(42):10656-10659. doi:10.1002/anie.201204268.

144. Lippok S, Seidel SA, Duhr S, et al. Direct detection of antibody concentration and affinity in human serum using microscale thermophoresis. *Anal Chem*. 2012;84(8):3523-3530. doi:10.1021/ac202923j.

145. Wolff M, Braun D, Nash MA. Detection of Thermoresponsive Polymer Phase Transition in Dilute Low-Volume Format by Microscale Thermophoretic Depletion. *Anal Chem*. 2014. doi:10.1021/ac5008283.

146. Alexander CG, Jürgens MC, Shepherd D a, Freund SM V, Ashcroft AE, Ferguson N. Thermodynamic origins of protein folding, allostery, and capsid formation in the human hepatitis B virus core protein. *Proc Natl Acad Sci U S A*. 2013;110(30):E2782-E2791. doi:10.1073/pnas.1308846110.

147. Maeda YT, Tlusty T, Libchaber A. Effects of long DNA folding and small RNA stem-loop in thermophoresis. *Proc Natl Acad Sci U S A*. 2012;109(44):17972-17977. doi:10.1073/pnas.1215764109.

148. Bielenberg JR, Brenner H. A hydrodynamic/Brownian motion model of thermal diffusion in liquids. *Phys A Stat Mech its Appl*. 2005;356(2-4):279-293. doi:10.1016/j.physa.2005.03.033.

149. Guha A. Transport and Deposition of Particles in Turbulent and Laminar Flow. *Annu Rev Fluid Mech*. 2008;40(1):311-341. doi:10.1146/annurev.fluid.40.111406.102220.

150. Li W, James Davis E. Measurement of the thermophoretic force by electrodynamic levitation: Microspheres in air. *J Aerosol Sci*. 1995;26(7):1063-1083. doi:10.1016/0021-8502(95)00047-G.

151. Zhao C, Oztekin A, Cheng X. Gravity-induced swirl of nanoparticles in microfluidics. *J Nanoparticle Res*. 2013;15(5). doi:10.1007/s11051-013-1611-8.

152. Lee H, Yook S-J. Deposition velocity of particles in charge equilibrium onto a flat plate in parallel airflow under the influence of simultaneous electrophoresis and thermophoresis. *J Aerosol Sci*. 2014;67:166-176. doi:10.1016/j.jaerosci.2013.10.006.

153. Longest PW, Xi J. Effectiveness of Direct Lagrangian Tracking Models for Simulating Nanoparticle Deposition in the Upper Airways. *Aerosol Sci Technol*. 2007;41(4):380-397. doi:10.1080/02786820701203223.

154. Majlesara M, Salmanzadeh M, Ahmadi G. A model for particles deposition in turbulent inclined channels. *J Aerosol Sci*. 2013;64:37-47. doi:10.1016/j.jaerosci.2013.06.001.

155. Tan SM, Ng HK, Gan S. CFD modelling of soot entrainment via thermophoretic deposition and crevice flow in a diesel engine. *J Aerosol Sci*. 2013;66:83-95. doi:10.1016/j.jaerosci.2013.08.007.

156. Woo S-H, Lee S-C, Yook S-J. Statistical Lagrangian particle tracking approach to investigate the effect of thermophoresis on particle deposition onto a face-up flat surface in a parallel airflow. *J Aerosol Sci*. 2012;44:1-10. doi:10.1016/j.jaerosci.2011.10.003.

157. Talbot L, Cheng RK, Schefer RW, Willis DR. Thermophoresis of particles in a heated boundary-layer. *J Fluid Mech*. 1980;101(DEC):737-758. doi:10.1017/s0022112080001905.

158. Bhagat AAS, Kuntaegowdanahalli SS, Papautsky I. Continuous particle separation in spiral microchannels using dean flows and differential migration. *Lab Chip*. 2008;8(11):1906. doi:10.1039/b807107a.

159. Mirkin CA, Letsinger RL, Mucic RC, Storhoff JJ. A DNA-based method for rationally assembling nanoparticles into macroscopic materials. *Nature*. 1996;382(6592):607-609. doi:10.1038/382607a0.

160. Medintz IL, Uyeda HT, Goldman ER, Mattoussi H. Quantum dot bioconjugates for imaging, labelling and sensing. *Nat Mater*. 2005;4(6):435-446. doi:10.1038/nmat1390.

161. Kadaksham ATJ, Singh P, Aubry N. Dielectrophoresis of nanoparticles. *Electrophoresis*. 2004;25(21-22):3625-3632. doi:10.1002/elps.200406092.

162. Neuman KC, Block SM. Optical trapping. *Rev Sci Instrum*. 2004;75(9):2787-2809. doi:10.1063/1.1785844.

163. Lin S-CS, Mao X, Huang TJ. Surface acoustic wave (SAW) acoustophoresis: now and beyond. *Lab Chip*. 2012;12(16):2766-2770. doi:10.1039/c2lc90076a.

164. Striemer CC, Gaborski TR, McGrath JL, Fauchet PM. Charge- and size-based separation of macromolecules using ultrathin silicon membranes. *Nature*. 2007;445(7129):749-753. doi:10.1038/nature05532.

165. Harrison DJ, Fluri K, Seiler K, Fan Z, Effenhauser CS, Manz A. Micromachining a miniaturized capillary electrophoresis-based chemical analysis system on a chip. *Science*. 1993;261(5123):895-897. doi:10.1126/science.261.5123.895.

166. Kwak R, Kim SJ, Han J. Continuous-Flow Biomolecule and Cell Concentrator by Ion Concentration Polarization. *Anal Chem*. 2011;83(19):7348-7355. doi:10.1021/ac2012619.

167. Dainiak MB, Kumar A, Galaev IY, Mattiasson B. Detachment of affinity-captured bioparticles by elastic deformation of a macroporous hydrogel. *Proc Natl Acad Sci U S A*. 2006;103(4):849-854. doi:10.1073/pnas.0508432103.

168. Edwards TL, Gale BK, Frazier AB. A microfabricated thermal field-flow fractionation system. *Anal Chem*. 2002;74:1211-1216. doi:10.1021/ac010653d.

169. Duhr S, Braun D. Two-dimensional colloidal crystals formed by thermophoresis and convection. *Appl Phys Lett*. 2005;86(13):131921. doi:10.1063/1.1888036.

170. Weinert FM, Mast CB, Braun D. Optical fluid and biomolecule transport with thermal fields. *Phys Chem Chem Phys*. 2011;13(21):9918-9928. doi:10.1039/c0cp02359k.

171. Lynn NS, Dandy DS. Geometrical optimization of helical flow in grooved micromixers. *Lab Chip*. 2007;7(5):580-587. doi:10.1039/b700811b.

172. Stroock AD, McGraw GJ. Investigation of the staggered herringbone mixer with a simple analytical model. *Philos Trans A Math Phys Eng Sci*. 2004;362(1818):971-986. doi:10.1098/rsta.2003.1357.

173. Stroock AD, Dertinger SK, Whitesides GM, Ajdari A. Patterning flows using grooved surfaces. *Anal Chem*. 2002;74(20):5306-5312.

174. Zhao C, Fu J, Oztekin A, Cheng X. Measuring the Soret coefficient of nanoparticles in a dilute suspension. *J Nanopart Res*. 2014;16(10):2625. doi:10.1007/s11051-014-2625-6.

175. Vigolo D, Buzzaccaro S, Piazza R. Thermophoresis and thermoelectricity in surfactant solutions. *Langmuir*. 2010;26(11):7792-7801. doi:10.1021/la904588s.

176. Würger A. Temperature dependence of the soret motion in colloids. *Langmuir*. 2009;25(12):6696-6701. doi:10.1021/la9001913.

177. Würger A. Thermal non-equilibrium transport in colloids. *Reports Prog Phys*. 2010;73(12):126601. doi:10.1088/0034-4885/73/12/126601.

178. Janča J. Micro-Thermal Field-Flow Fractionation in the Analysis of Polymers and Particles: A Review. *Int J Polym Anal Charact*. 2006;11(1):57-70. doi:10.1080/10236660500486416.

179. Janča J. Polarization, steric, and focusing micro-thermal field-flow fractionation principles, theory, instrumentation, and applications in polymers and particles analysis. *Anal Chim Acta*. 2005;540(1):187-196. doi:10.1016/j.aca.2004.09.018.

180. Messaud FA, Sanderson RD, Runyon JR, Otte T, Pasch H, Williams SKR. An overview on field-flow fractionation techniques and their applications in the separation and characterization of polymers. *Prog Polym Sci*. 2009;34(4):351-368. doi:10.1016/j.progpolymsci.2008.11.001.

181. Thompson GH, Myers MN, Giddings JC. An Observation of a Field-Flow Fractionation Effect with Polystyrene Samples. *Sep Sci*. 1967;2(6):797-800. doi:10.1080/01496396708049739.

182. Thompson GH, Myers MN, Giddings JC. Thermal field-flow fractionation of polystyrene samples. *Anal Chem*. 1969;41(10):1219-1222. doi:10.1021/ac60279a001.

183. Janca J, Kaspárková V, Halabalová V, Simek L, Růzicka J, Barosová E. Micro-thermal field-flow fractionation of bacteria. *J Chromatogr B Analyt Technol Biomed Life Sci*. 2007;852(1-2):512-518. doi:10.1016/j.jchromb.2007.02.018.

184. Janca J. Micro□channel Thermal Field□Flow Fractionation: High□Speed Analysis of Colloidal Particles. *J Liq Chromatogr Relat Technol*. 2003;26(6):849-869. doi:10.1081/JLC-120018888.

185. Giddings JC, Martin M, Myers MN. High-speed polymer separations by thermal field-flow fractionation. *J Chromatogr A*. 1978;158:419-435. doi:10.1016/S0021-9673(00)89985-9.

186. Flagan RC. Continuous-flow differential mobility analysis of nanoparticles and biomolecules. *Annu Rev Chem Biomol Eng*. 2014;5:255-279. doi:10.1146/annurev-chembioeng-061312-103316.

187. Kreysing M, Keil L, Lanzmich S, Braun D. Heat flux across an open pore enables the continuous replication and selection of oligonucleotides towards increasing length. *Nat Chem*. 2015;7(3):203-208. doi:10.1038/nchem.2155.

Appendix

Publications arising from this work

Journal Papers

C. Zhao, J. Fu, A. Oztekin and X. Cheng 'Measuring the Soret coefficient of nanoparticles in a dilute suspension' Journal of Nanoparticle Research, 16 (2014) 2625

C. Zhao and X. Cheng 'Thermophoresis of biomolecules and bioparticles in aqueous solutions: a mini review' International Journal of Terraspace Science and Engineering, 6 (2014) 63

C. Zhao, A. Oztekin and X. Cheng 'Gravity-induced swirl of nanoparticles in microfluidics' Journal of Nanoparticle Research 15 (2013) 1611

C. Zhao and X. Cheng 'Microfluidic separation of viruses from blood cells based on intrinsic transport processes' Biomicrofluidics 5 (2011) 032004

C. Zhao, S. Tang and Y. Du 'Effect of non-pore-widening on plasmon resonances of silver nanowire arrays in anodized aluminum oxide' Chemical Physics Letters 491 (2010) 183

Conference presentations and extended abstracts

C. Zhao, A. Oztekin and X. Cheng 'Measuring the thermal diffusion coefficients of artificial and biological particles in a microfluidic chip' 66th Annual Meeting of the APS Division of Fluid Dynamics, Pittsburgh, PA, November 2013 (Oral presentation)

C. Zhao and X. Cheng 'Gravity induced archimedean spiral in density mismatched multistream flow' Biomedical Engineering Society Annual Fall Meeting, Atlanta, GA, October 2012 (Poster presentation)

C. Zhao and X. Cheng 'Microfluidic separation of viruses from blood cells based on intrinsic transport processes' Biomedical Engineering Society Annual Fall Meeting, Hartford, CT, October 2011 (Oral presentation)

Vita

Chao Zhao was born in Yangzhou, Jiangsu, China on February 4th, 1986, the son of Jialong Zhao and Shanshan Zhou. After completing his study in Jiangsu Jiangdu Middle School in 2003, he attended Nanjing University in Nanjing, China, for undergraduate study. He graduated from Nanjing University in May 2007, with the degree of Bachelor of Science in Physics. In January of 2010, he received the degree of Master of Science from Nanjing University, under the supervision of Dr. Shaolong Tang. He then started his PhD studies in the Department of Materials Science and Engineering and Bioengineering program at Lehigh University in August of 2010. Under the supervision of Dr. Xuanhong Cheng, he has been working on the microfluidic technology since 2010, which comprises this thesis.